NREL/TP-410-4960 • UC Category: 270 • DE92010592

New Concepts for High Efficiency Energy Conversion: The Avalanche Heterostructure and Superlattice Solar Cells

A Subcontract Report
1 June 1987 - 31 January 1990

NREL/TP--410-4960

DE92 010592

C. J. Summers, A. Rohatgi, A. Torabi,
H. M. Harris
Georgia Tech Research Institute
Atlanta, Georgia

NREL technical monitor: T. S. Basso

National Renewable Energy Laboratory
1617 Cole Boulevard
Golden, Colorado 80401-3393
A Division of Midwest Research Institute
Operated for the U.S. Department of Energy
under Contract No. DE-AC02-83CH10093

Prepared under Subcontract No. XL-7-06074-1

January 1993

MASTER

This publication was reproduced from the best available camera-ready copy
submitted by the subcontractor and received no editorial review at NREL.

NOTICE

This report was prepared as an account of work sponsored by an agency of the United States government. Neither the United States government nor any agency thereof, nor any of their employees, makes any warranty, express or implied, or assumes any legal liability or responsibility for the accuracy, completeness, or usefulness of any information, apparatus, product, or process disclosed, or represents that its use would not infringe privately owned rights. Reference herein to any specific commercial product, process, or service by trade name, trademark, manufacturer, or otherwise does not necessarily constitute or imply its endorsement, recommendation, or favoring by the United States government or any agency thereof. The views and opinions of authors expressed herein do not necessarily state or reflect those of the United States government or any agency thereof.

Printed in the United States of America
Available from:
National Technical Information Service
U.S. Department of Commerce
5285 Port Royal Road
Springfield, VA 22161

Price: Microfiche A01
Printed Copy A06

Codes are used for pricing all publications. The code is determined by the number of pages in the publication. Information pertaining to the pricing codes can be found in the current issue of the following publications which are generally available in most libraries: *Energy Research Abstracts (ERA)*; *Government Reports Announcements* and Index (*GRA* and I); *Scientific and Technical Abstract Reports (STAR)*; and publication NTIS-PR-360 available from NTIS at the above address.

TABLE OF CONTENTS

1. INTRODUCTION

Solar cell efficiency is determined by material quality and the ability to fabricate device structures whose spectral response is well matched to the solar spectrum.[1,2] Essentially, the optical response of the semiconductor provides a fundamental limit to cell performance while the cell geometry and doping profiles impact the efficiency through the design details of the structure.

These limitations have resulted in investigations of multi-bandgap cells which make more efficient use of the solar spectrum by extending the spectral response of the cell. For a two-bandgap cell with energy gaps of ~1.64 eV and 0.96 eV, the ideal efficiency is 38% and 50% for 1 and 1000 suns concentration, respectively. Calculations also predict that the efficiency increases with the number of bandgaps and reaches a limit of 72% for 36 bandgaps.[3] However, because of this complexity, and the fact that the increase in efficiency for each additional cell is small, multi-bandgap cells are not economic. Also, it should be noted that even the two-bandgap cascade solar cell is a relatively complex structure, requiring several changes in alloy composition and doping levels in order to fabricate both solar cells and the connecting tunnel junctions.

In this program we have investigated the theory and technology of a novel heterojunction or superlattice, single junction solar cell, which injects electrons across the heterointerface to produce highly efficient impact ionization of carriers in the low bandgap side of the junction, thereby conserving their total energy. Also, the superlattice structure has the advantage of relaxing the need for perfect lattice matching at the p-n interface and will inhibit the cross diffusion of dopant atoms that typically occurs in heavy doping. This structure avoids the use of tunnel junctions which make it very difficult to achieve the predicted efficiencies in cascade cells. Thus it should be possible to obtain energy efficiencies that are competitive with those predicted for cascade solar cells with reduced complexity and cost. Finally, we note that this cell structure could be incorporated into other solar cell structures designed for wider spectral coverage.

2. TECHNICAL PROGRESS

2.1 Calculation of Heterojunction Avalanche Solar Cell Efficiency

In 1980, Pearsall suggested the use of an abrupt p^+-n-n^+ heterojunction as a means to extend the spectral response of a single junction solar cell and to obtain higher energy conversion efficiencies.[4] In the proposed scheme, shown in Figure 1, the energy gap of the p-side junction is more than twice the bandgap energy of the n-side. Thus the photo-generated electrons on the p^+-side are injected by the internal electric field over the heterointerface into the low bandgap layer. Because they experience the full difference in energy gaps, impact ionization occurs and a photo-current gain of two is realized. Thus the energy of the electrons in the wide bandgap region is conserved by adding it to the current generated by the low bandgap side of the junction. The efficiency of the electron injection process is determined by the quality and abruptness of the heterojunction which must be shorter than the phonon scattering mean free path, ~100Å. To achieve this transition requires that both the compositional gradient, and the depletion lengths induced by doping, are considerably less than 100Å. Abrupt changes in both alloy composition and doping concentration can be obtained over distances much less than this (<20Å) by molecular beam epitaxy growth provided sufficient control is obtained over the technique. Also, Pearsall has shown that the depletion lengths in most semiconductor materials of interest are <30Å, for doping concentrations of $2\text{-}3\times10^{18}\text{cm}^{-3}$. Thus it appears that the concept is technically feasible, and requires detailed modeling studies in order to estimate the theoretical increase in efficiency that is possible with this cell design and also to develop the best cell geometry for approaching the theoretical limits.

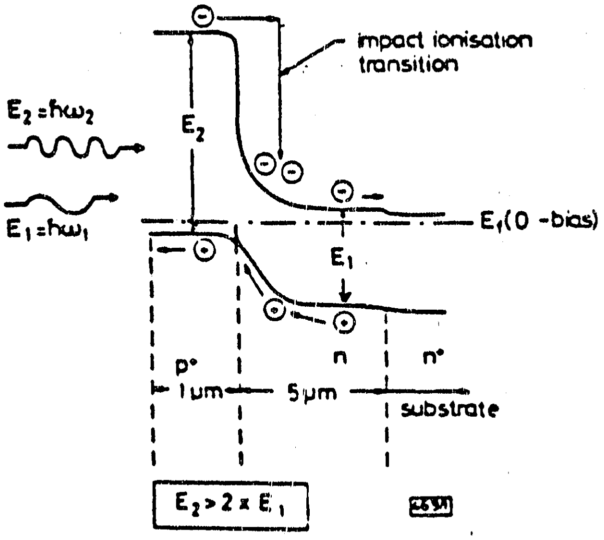

Figure 1. Energy level diagram for heterojunction solar cell.

2.1.1 Model Calculation for Homojunction

To estimate the potential benefits of the scheme proposed by Pearsall we apply the scheme used by Henry[3] to calculate the limiting efficiencies of ideal single, and multiple, energy gap terrestrial solar cells. This approach calculates the efficiency by only considering the two intrinsic loss mechanisms which limit the efficiency of an ideal solar cell. The first intrinsic loss mechanism is the inability of a single energy gap cell to properly match the broad solar spectrum. Photons with energies $h\nu$, less than the bandgap energy, are not absorbed and solar photons with $h\nu > E_G$ generate electron-hole pairs which very rapidly lose most of their energy in excess of E_G to optical phonon scattering. The second major loss is due to radiative recombination by the cell. The rate of radiative emission increases exponentially with the applied bias energy eV, where V is the voltage developed across the load.

The many extrinsic limitations that are not considered in this calculation include losses due to reflection, contacts, series resistance, absorption in window layers, incomplete photon collection, nonradiative recombination and cell heating.

To avoid excessive complications the calculation is only performed for an extraterrestrial air mass 0 spectrum which is approximated by a 5800 K blackbody spectrum (Figre 2). Thus the solar flux $N_{ph}(E)$ (in photons $cm^{-2}s^{-1}$) is calculated as a function of bandgap energy, E_G, using the formula

$$n_{ph}(E_G) = \int_{E_G}^{\infty} \frac{2\pi\nu c^2}{e^{h\nu/kT}-1} \cdot d\nu \qquad (1)$$

Here it is assumed that the semiconductor is opaque for photons with energies greater than E_G, and transparent for photons with energies less than E_G. Consequently the number of photons absorbed by a semiconductor with bandgap E_G is given by integrating Equation 1 for all energies above E_G; i.e.

$$n_{ph}(E_G) = \int_{E_G}^{\infty} \frac{dn_{ph}}{dE} \cdot dE \qquad (2)$$

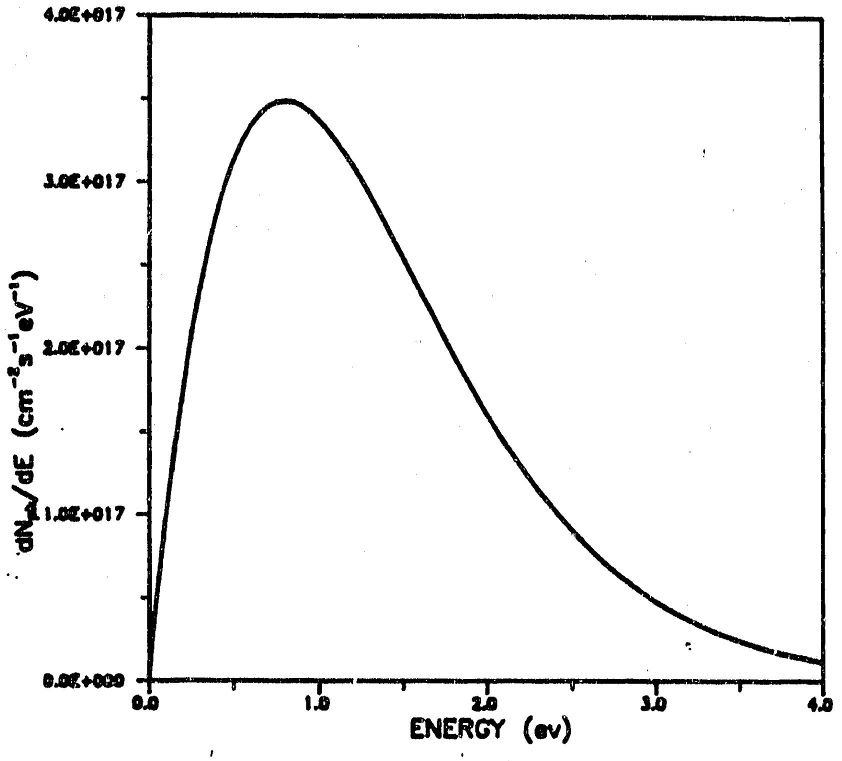

Figure 2. The 5800K blackbody radiation spectrum used for these calculations.

The area under the $n_{ph}(E_G)$ vs. E_G curve is therefore equal to the total solar cell power generated per unit area, i.e.

$$P = \int_0^\infty E_G \left(\frac{dn_{ph}}{dE_G} \right) \cdot dE_G \tag{3}$$

To be able to calculate the efficiency of a solar cell it is first necessary to determine the maximum work that can be done by each absorbed photon. The total current density, J, delivered to the load of the cell is the sum of the current densities produced by the solar (J_{ph}) and ambient thermal radiation (J_{th}), minus the current density (J_{rad}) lost by radiative recombination from the top and bottom surfaces of the cell. Thus

$$J = J_{ph} + J_{th} - J_{rad} \tag{4}$$

where;

$$J_{ph} = qn_{ph} \; , \tag{5}$$

$$J_{th} = A_{th} \exp(-E_G/kT_B) \tag{6}$$

and,

$$J_{rad} = A_{rad} \exp((qV - E_G)/kT_B) \tag{7}$$

In these equations

$$A_{rad} = \frac{q(n^2+1)\,E_G^2 kT}{4\pi^2 \hbar^3 c^2} = 5693 E_G^2 A cm^{-2}$$

T is the suns temperature, T_B is the ambient temperature, n is the semiconductor refractive index, E_G is the bandgap energy in electron volts, q is the electron charge, k is Boltzman's constant, $\hbar$ is Plank's modified constant and c is the velocity of light. Substituting in Equation 4, therefore, gives the total current as:

$$J = qn_{ph} + A_{th}\exp(-E_G/kT) - A_{rad}\exp((qV - E_G)/kT) \tag{8}$$

The open circuit cell voltage, V_{oc}, is then found by setting J = 0.

$$V_{oc} = kT \cdot \ln\left(1 + \frac{qn_{ph}(E_G)}{e^{E_G/kT} - 1}\right) \tag{9}$$

Next the maximum power point, (J_m, V_m), is found by setting d(JV)/dV = 0. This calculation gives

$$eV_m = eV_{oc} - kT\ln\left(1 + \frac{qV_m}{kT_B}\right) \tag{10}$$

and

$$J_m = \frac{qn_{ph}}{1 + kT/eV_m} \tag{11}$$

From these calculations the work done per absorbed photon, W, is obtained from the equation

$$W = \frac{J_m V_m}{\eta_{ph}} \tag{12}$$

The cell efficiency, η, is then given by the expression

$$\eta = \frac{100 N_{ph} W}{P} \tag{13}$$

where $N_{ph} = n_{ph}(0)$ from Equation 2, and is the total number of photons captured from the sun by the solar cell.

2.1.2 Numerical Procedure and Results

The numerical calculation used to obtain the cell efficiency as a function of bandgap energy and also sun concentration then proceeds as follows. Equation 2 is used to obtain the number of photons emitted as a function of bandgap energy (Figure 2). From Equation 2 the number of photons absorbed by a semiconductor with bandgap energy, E_G, is then calculated from E_G values between 0 and 4 eV. This curve is labelled the 100% line in Figure 3. The integration of Figure 3 is next performed to obtain the total solar power per unit area. Finally, for each bandgap energy, solutions are found for V_{oc}, V_m, J_m, and W. The dependence of W on E_G is also shown in Figure 3. As discussed by Henry Figure 3 can be broken down into four areas. The area labelled $h\nu<E_G$ is identified with photons that are not absorbed and which, therefore, can make no contribution to the power generated by the cell. The area labeled $h\nu>E_G$ is identified with the work lost from photons with energies above E_G which is dissipated as heat in the cell. The area labeled $W<E_G$ is attributed to work lost because of radiative recombination from the cell. Finally the last (unshaded) region equals the power per unit area delivered by the solar cell to the load.

The ratio of this area to the total area under the 100% line gives the efficiency of the cell for one bandgap energy. By calculating this area as a function of energy the dependence of η on bandgap energy is obtained as shown in Figure 4. From this curve both the bandgap energies required to maximize and the value of the peak efficiency are found.

Figure 4 shows the calculation performed for sun concentrations of one and a thousand ($C = 1$ and 1000) and indicates that efficiencies of 28.8% and 34.9% should be obtained for bandgap energies of 1.35 and 1.25 eV, respectively. Henry's results which are for the actual measured solar spectrum give efficiencies of 30% and 37% and bandgap energies of 1.35 and 1.25 eV. Because for the actual measured solar spectrum energy is lost from the low energy side of the spectrum, due to water absorption, Henry's calculation slightly favors higher efficiencies and bandgap energies. Thus our calculation is in very good agreement with Henry's results. Furthermore we have also extended this calculation to multiple bandgap cells and obtained very close agreement with Henry's data.

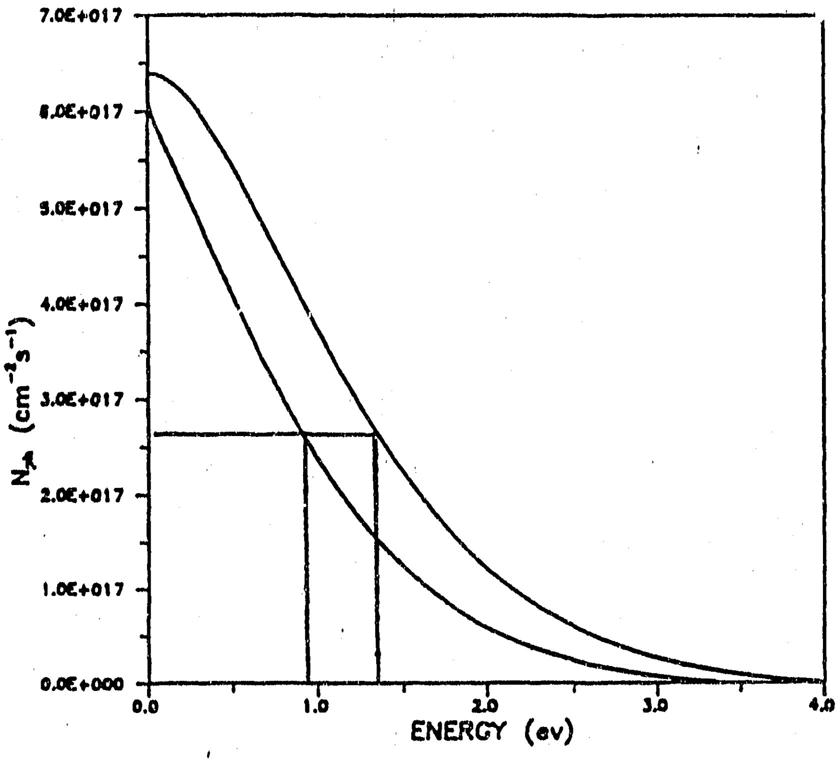

Figure 3. Graphical representation of the efficiency of an ideal solar cell as developed by Henry. The outer curve is the absorbed photon flux vs. the energy gap. The inner curve is the work done per absorbed photon vs. the absorbed photon flux.

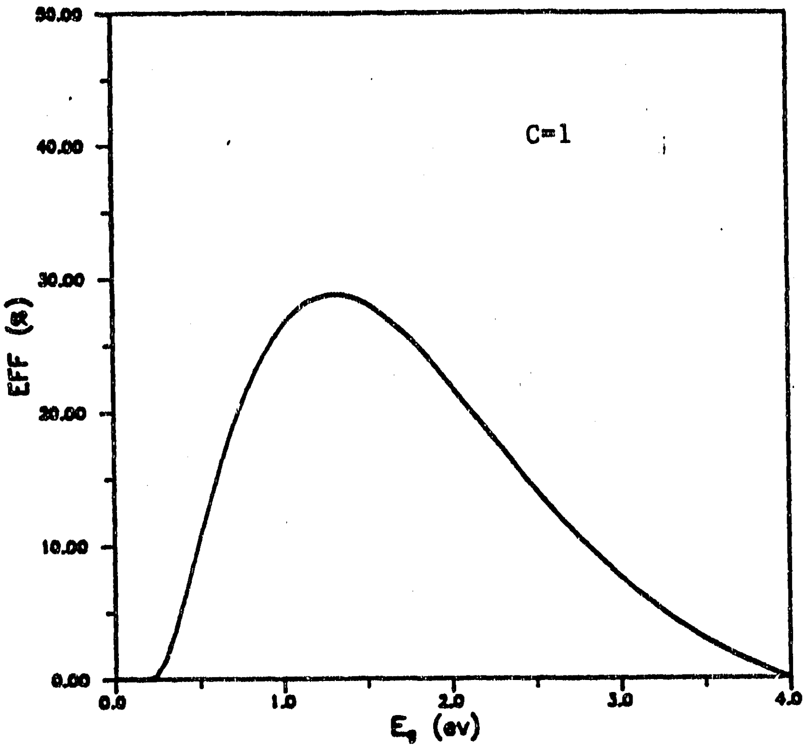

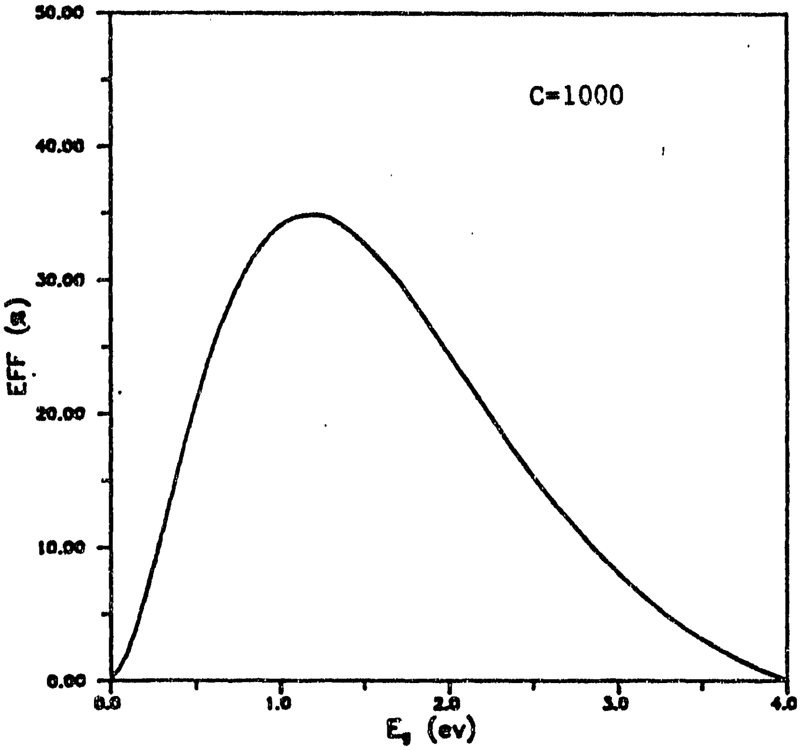

Figure 4. Solar-cell efficiency vs. energy gap for sun concentrations of 1 and 1000, respectively.

To investigate the heterojunction avalanche photodiode solar cell it is necessary to; (1) incorporate into this theory the greater collection efficiency expected from the use of two bandgap energies and the impact ionization phenomena, and (2) to fully consider the effect of the electrical properties of the heterojunction on cell performance.

2.1.3 Model Calculation for Heterojunction

In the heterojunction solar cell proposed by Pearsall and shown in Figure 1 light enters the p-n diode from the wide bandgap side. Thus photons with energies greater than E_{G2} are absorbed by the top p-type layer and photons with energies between E_{G2} and E_{G1} by the smaller bandgap n-type layer. When $E_{G2} \geq 2E_{G1}$ a photon excited electron in the wide bandgap material has sufficient potential energy to impact ionize a second electron-hole pair on the low bandgap side of the cell as it crosses the interface. Thus for 100% ionization the effective quantum efficiency of photons with energies greater than E_{G2} is two. However, it should be noted that the open cell voltage of the heterojunction is still limited by the smaller bandgap material.

The effective increase in photo-collection efficiency for this cell structure is then given by:

$$\eta_{pb}(E_{G1}) = \int_{E_{G1}}^{E_{G2}+\gamma E_{G1}} \frac{d \cdot n_{pb}}{dE} \cdot dE + g \cdot \int_{E_{G2}}^{\infty} \frac{dn_{pb}}{dE} \cdot dE \tag{14}$$

Where γ is the ratio of the bandgap energies (E_{G1} to E_{G2}) and g is the impact ionization efficiency. Thus

$$\gamma = \frac{E_{G2}}{E_{G1}} \geq 2, \tag{15}$$

and

$$1 < g \leq 2. \tag{16}$$

To calculate the efficiency of this structure the same procedures as discussed previously were used. Except that in this calculation Equation 2 is replaced by Equation 14 and the open cell voltage is calculated only for the small bandgap (n-type) side of the cell, as this controls the built-in voltage of the heterojunction.

From the discussion presented below we believe that this is a good approximation to the actual situation. In Figure 5 we show schematic representations of the band edge alignments for, an undoped heterostructure, an unbiased p-n heterojunction and an optically (forward) biased p-n heterojunction for the following conditions $\Delta E_v = 0$, $\Delta E_v \leq 0$, $\Delta E_v > 0$, and $\Delta E_c \geq E_{G1}$. Also shown are the structures under an optical bias V_{oc} (E_{fn} - E_{fp}), where E_{fn} and E_{fp} are, respectively, the Fermi-levels in the n- and p-type material. The maximum possible value of V_{oc} is at the valance flat band position, when there is alignment between the top of the valence bands on both sides of the junction. If V_{oc} should increase above this value then the valence band on the p-side of the junction will become lower than on the n-side of the junction and start to reduce the hole current. Note that for the flat band condition shown in Figure 5 the band alignment condition $\Delta E_v \geq 0$ gives the least impediment to current flow. Also Figure 5 shows the requirement that ΔE_c equals Δ_{G1} is met when $E_{G2} = 2E_{G1}$ at flat band, but that if this condition is not realized, then for some conditions of optical bias the condition $\Delta E_c > \Delta E_{g1}$ can be realized for bandgap energies E_{G2} smaller than $2E_{G1}$. Finally we note that because the valence band heavy hole effective mass, which controls the magnitude of E_{fp}, is not strongly dependent on bandgap energy, calculating V_{oc} for a single bandgap cell is expected to be a good approximation to the heterojunction situation.

2.1.4 Heterojunction Results

Figure 6 shows the efficiency calculation for the superlattice avalanche photodiode solar cell as calculated by the above approach. In this calculation ideal collection conditions are assumed and values of $\gamma=2$ and g=2 are used. For both 1 and 1000 suns concentration little enhancement is observed for cells with bandgap energies greater than 1.8 eV. This is because as shown by Figure 2 there are very few photons with energies above 3.6 eV. However, as the energy gap decreases below 1.8 eV more photons with energies greater than twice the bandgap energy are absorbed which can impact ionize and double the effective number of electrons contributing to the photo-current. Figure 6 shows that as E_G goes to zero the total gain in the effective

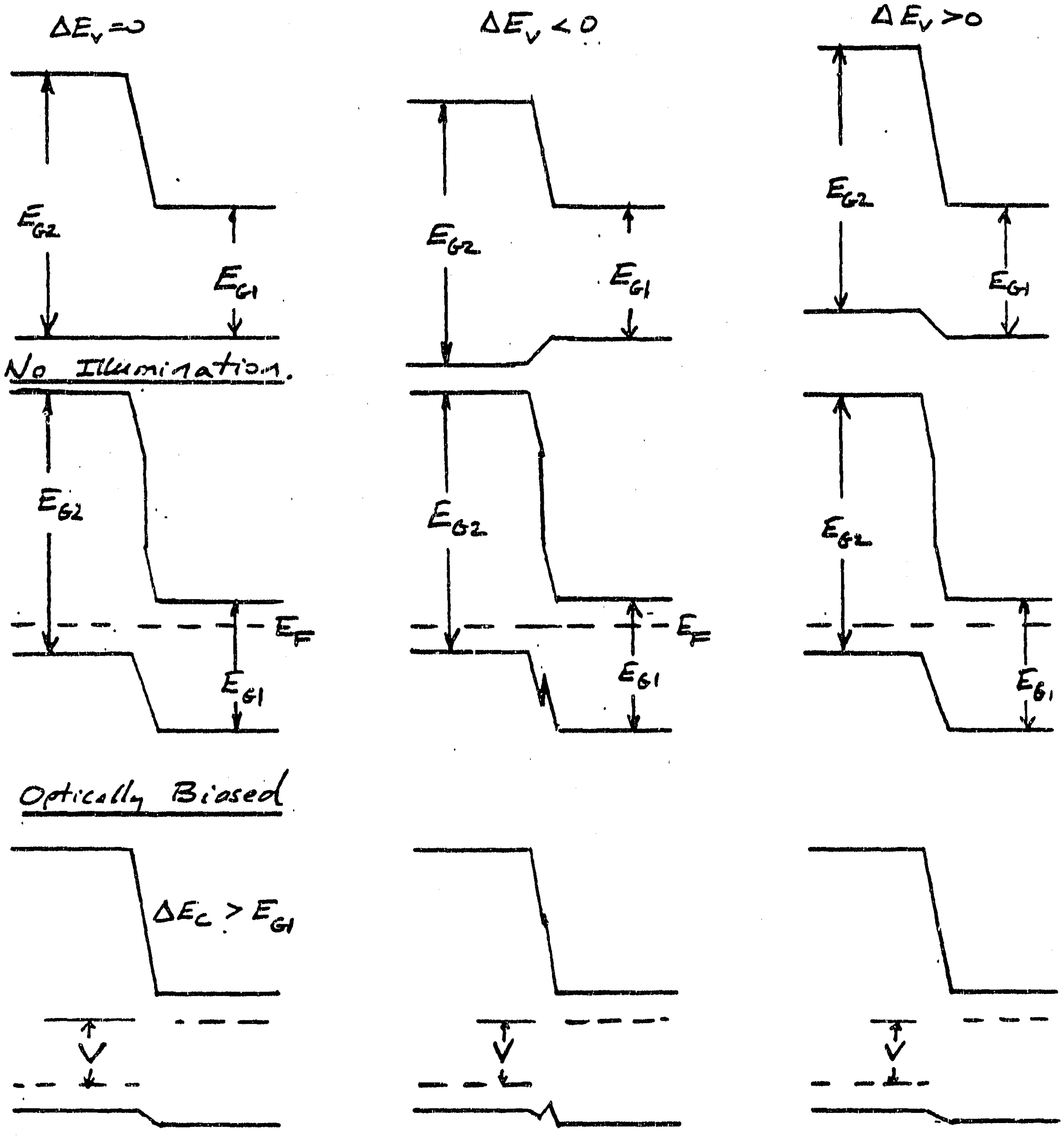

Figure 5. Schematic of band edge alignments for undoped heterostructure and homojunction devices.

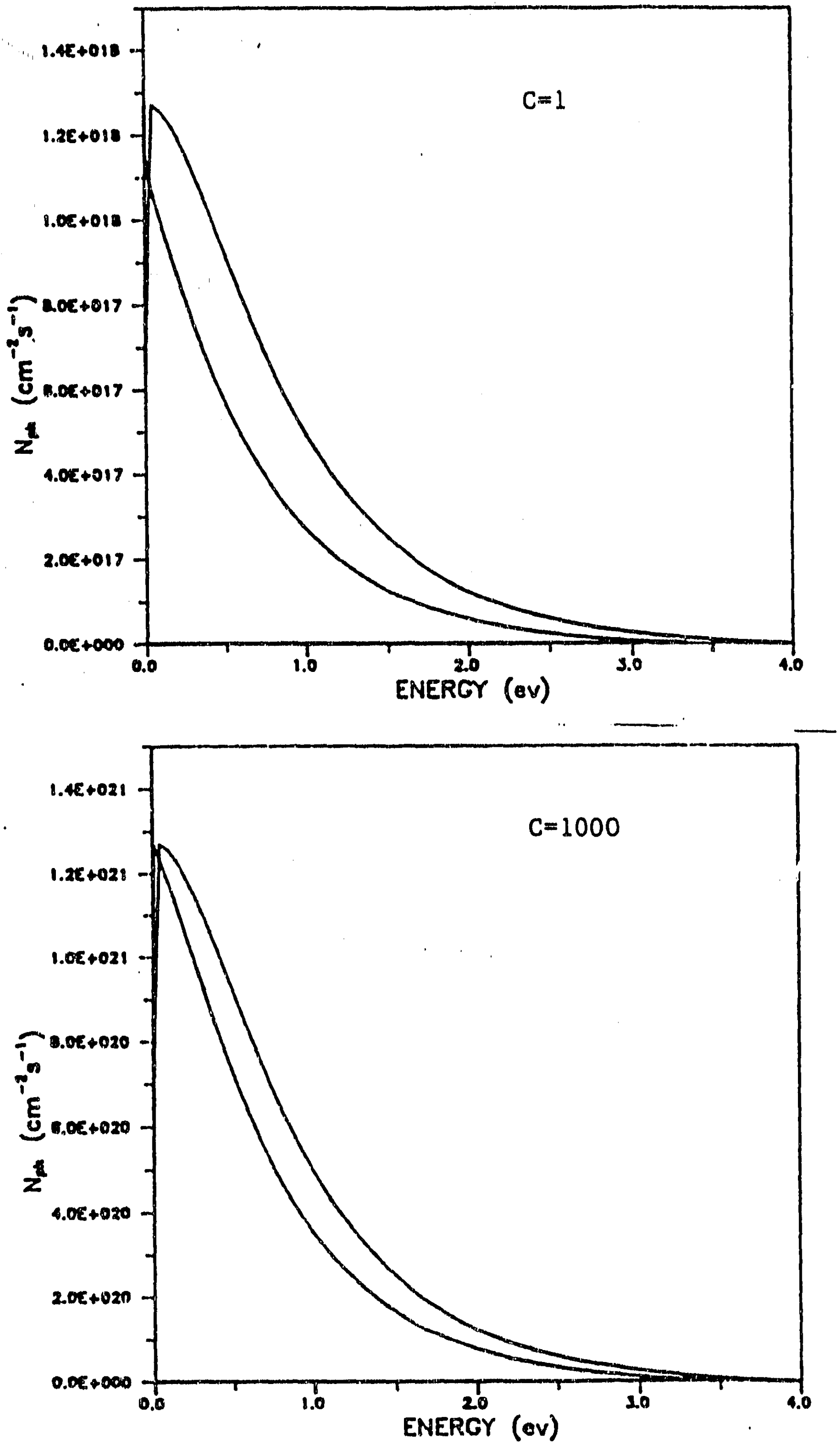

Figure 6. Graphical representation of the performance of an ideal avalanche photodiode solar cell for 1 and 1000 suns. As in Figure 3 the outer curve is the absorbed photon flux vs. the energy gap, and the inner curve represents the work done per absorbed photon vs. the absorbed photon flux.

number of carriers collected is doubled in the APD-solar cell design. This improvement in collection efficiency occurs for both 1 and 1000 suns concentration factors. The figure also demonstrates, when compared to Figure 3, that for low bandgap energies the effective work done by the cell increases due to the increased photon collection. This effect is very pronounced for high (1000) suns concentration as shown by Figure 6b.

The dependence of the efficiency of the APD-solar cell on the bandgap energy, E_{G1}, of the smaller bandgap is shown in Figure 7. From these curves it is shown that for a sun concentration of one a maximum efficiency of 35.3% is obtained when E_{G1} = 1.15 eV. For a sun concentration of 1000 the efficiency increases to 45.4% for a bandgap energy of 0.95 eV. A comparison between Figures 4 and 7 shows that for bandgap energies greater than 1.8 eV both the conventional and avalanche solar cell have the same efficiencies. Thus it is only for smaller bandgap cells with values of E_{G1} less than 1.8 eV that appreciable increases in performance are realized.

We also show in Figure 7 the effect of decreasing the multiplication ratio from 2.0 to 1.5 in steps of 0.1 for a concentration factor of 1000. As shown both the peak efficiency and the optimum bandgap energy decrease uniformily towards the curve shown for a simple homopolar junction. Basically, therefore, the avalanche photodiode solar cell collects twice the number of E_{G1} photons for ideal ($\gamma = 2$, $g = 2$) conditions and responds in a similar manner to increasing the collection efficiency. In Figure 8 the reverse effect of changing the bandgap ratio, g is shown for the maximum multiplication ratio, $\gamma = 2$. As shown a 10% variation in this value has approximately a 1% change in the total efficiency, from 46.5 - 44.5%, but produces little change in the optimum value of E_{G1}.

A more practical calculation which takes into account the nonideal electrical characteristics of a solar cell was also investigated. For this situation the diffusion and generation - recombination currents must be included. As discussed by Landsberg and Evans[5] the total current now becomes:

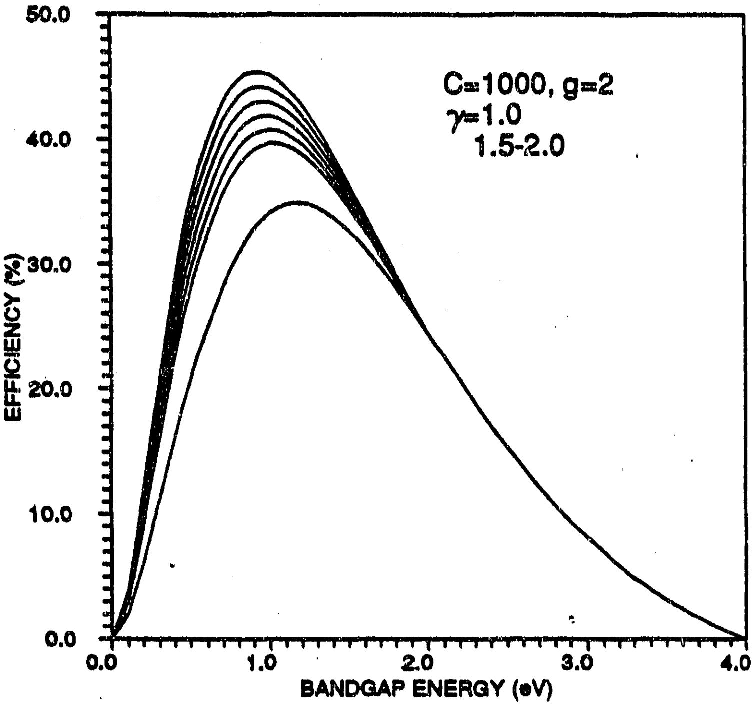

Figure 7. Efficiency of avalanche heterojunction solar cell as a function of bandgap energy, and impact-ionization ratio for ideal bandgap ratio and 1000 suns concentration.

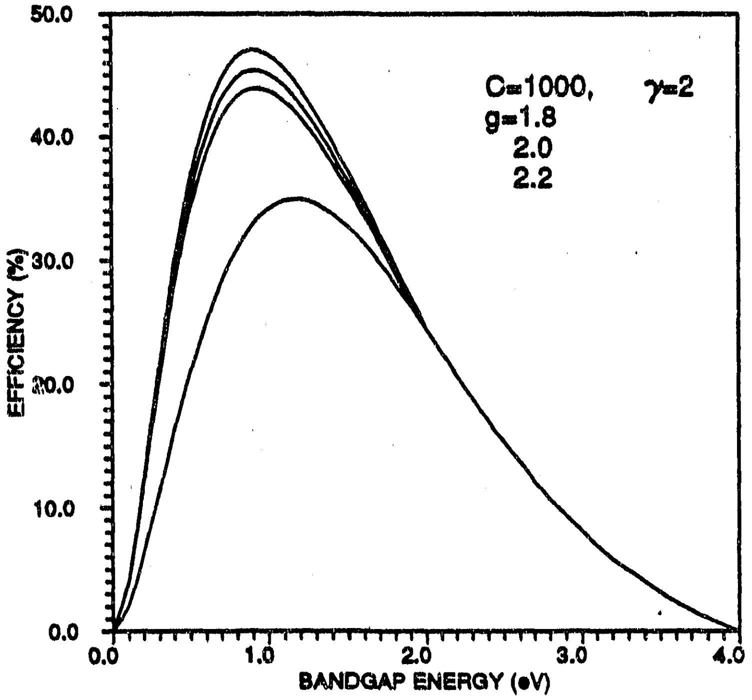

Figure 8. Efficiency of avalanche heterojunction solar cell as a function of bandgap energy, and bandgap ratio for ideal impact-ionization conditions and 1000 suns concentration.

$$
\begin{aligned}
J = {} & \eta_{pb} + Ae^{-E_g/kT} - Ae^{(eV-E_g)/kT} \\
& - A_D(e^{V/kT}-1) - A_R(V_B - V)^{1/2}(e^{V/kT}-1) \\
& - \frac{A_A}{2}\,\frac{(e^{V_s/kT}-e^{V/kT})(e^{V/kT}-1)}{(V_B - V)^{1/2}}
\end{aligned}
\tag{17}
$$

where:

$$A_A = 2q\eta_i^2(B_1 n_{op} + B_2 P_{op})kTA_w$$

in which

$$A_w = \sqrt{\frac{2\epsilon\,\epsilon_0(N_D+N_A)}{q(N_D N_A)}}$$

is the depletion wide of the device.

In the above the diffusion coefficients are given by:

$$A_D = \frac{qD_n\eta_{po}}{L_n} + \frac{qD_p P_{no}}{L_p}\ ;\ D = \frac{kT\mu}{q}\ ;\ L = \sqrt{D\tau}$$

$$= q\eta_{op}\sqrt{\frac{kT\mu n/q}{\tau_n}} + qp_{on}\sqrt{\frac{kT\mu p/q}{\tau_p}}$$

$$A = \frac{q(\eta^2+1)E_G^2 kT}{4\pi^2\hbar^3 c^2}$$

$$V_{oc} = kT\ln\left(\frac{q\eta_{pb} + A_e^{-Eg/kT} + A_D}{A_e^{-E_s/kT} + A_D}\right)$$

Note that Âuger terms are not included in this analysis.

$$A_R = q\eta_i^2 B_R A_w$$

Note: ideal V_{oc} ignores diffusion currents: $A_D = 0$.

$$P_{w\eta} = JV = Vq\eta_{ph} + VA[e^{-Eg/kT} - e^{(V-E_i)/kT}]$$

$$-VA_D(e^{V/kT}-1) - VA_R(V_B - V)^{1/2}(e^{V/kT}-1)$$

$$-V\frac{A_A}{2}(V_B - V)^{-1/2}[e^{(V_s+V)/kT} - e^{2V/kT} - e^{V_s/kT} + e^{V/kT}]$$

maximize power by $\frac{a(JV)}{aV}=0$

$$0 = \frac{\alpha(JV)}{\alpha V} = qn_{ph} + A[e^{-E_i/kT} - e^{(V-E_a)/kT}]$$

$$-\frac{VA}{kT}e^{(V-E_i)/kT} - A_0(e^{V/kT}-1) - \frac{VA_D}{kT}e^{V/kT}$$

$$-A_R(V_B - V)^{1/2}(e^{V/kT}-1) + \frac{VA_R}{2}(V_B - V)^{-1/2}(e^{V/kT}-1)$$

$$-\frac{VA_R}{kT}(V_B - V)^{1/2}(e^{V/kT}-1)$$

$$-\frac{A_A}{2}(V_B - V)^{-1/2}[e^{(V_s+V)/kT} - e^{2V/kT} - e^{V_s/kT} + e^{V/kT}]$$

$$-\frac{VA_A}{4}(V_B - V)^{-3/2}[e^{(V_s+V)/kT} - e^{2V/kT} - e^{V_s/kT} + e^{V/kT}]$$

$$-\frac{VA_A}{2kT}(V_B - V)^{-1/2}[e^{(V_s+V)/kT} - 2e^{2V/kT} - e^{V_s/kT} + e^{V/kT}]$$

The above equation is solved by the Newton Raphson method, which requires the derivative of the function, i.e., $\frac{a^2(JV)}{aV}$. This is given below as:

$$f' = \frac{\alpha^2(JV)}{\alpha V^2}$$

$$= \frac{-q\eta_{ph}}{kT} e^{-V/kT} - \frac{A}{kT} e^{-(E_t + V)/kT} - \frac{a}{kT} e^{-E_t/kT}$$

$$-\frac{A_D}{kT} e^{-V/kT} - \frac{A_D}{kT} - A_R\left[(V_B - V)^{-1/2}(e^{-V/kT} - 1) + \frac{1}{kT}(V_B - V)^{1/2}\right]$$

$$-\frac{1}{kT}A_R(V_B - V)^{1/2} e^{-V/kT} - A_R V\left[\frac{1}{4}(V_B - V)^{-3/2}(e^{-V/kT} - 1)^{-1/2}\frac{1}{kT}(V_B - V)^{-1/2} e^{-V/kT} - \frac{1}{2kT}(V_B - V)^{-1/2}\right]$$

$$-\frac{A_A}{2}\left[\frac{1}{2}(V_B - V)^{-3/2} + \frac{1}{2}(V_B - V)^{-3/2} + \frac{3}{4}V(V_B - V)^{-5/2}\right][e^{V_B/kT} - e^{V/kT} - e^{(V_B - V)/kt} + 1]$$

$$-\frac{A_A}{2kT}[(V_B - V)^{-1/2} + 1/2\, V(V_B - V)^{-3/2}][-1e^{V/kT} + 1e^{(V_B - V)/kT}]$$

$$-\frac{A_A}{2kT}[(V_B - V)^{-1/2} + 1/2\, V(V_B - V)^{-3/2}][e^{V_B/kT} - 2e^{V/kT} + 1]$$

$$+A_A V(V_B - V)^{-1/2}(k/T)^2 e^{V/kT}$$

Using these equations the same calculations as described before were performed. These studies showed that the same results are obtained provided the n- and p-type concentrations forming the junction are no greater than 10^{17}cm^{-3} and 10^{15}cm^{3}, respectively. Although these carrier concentrations are easy to realize to optimize the junction characteristics they will result in very high contact resistances to the device. Thus it will be necessary to control the profile in these devices such that the above carrier concentrations can be maintained in the active photo-collection region of the junction and also increased to values of $>10^{18}$cm^{-3} near the contact areas. This would allow independent optimization of the photoconductive properties of the cell where photons are absorbed and the electrical properties of the structure where connections are made to the external circuit. Further optimization of the solar cell can also be achieved with the use of hetero- (wider-bandgap) layers for the contact regions. The inclusion of the Âuger terms would place even more stringent requirements on material properties.

2.2 Experimental Investigations

From the theoretical analysis performed in the previous section it was shown that a conduction band offset of 0.8 to 1.0 eV was required to optimize the efficiency of a heterojunction avalanche photodiode solar cell. Possible material combinations with the required energy gap range under closely lattice matched conditions are:

AlInAs/GaInAs (a = 5.8A, E_G = 1.6 - 0.7 eV)
AlInSb/GaInSb (a = 6.25A, E_G = 1.5 - 0.4 eV)
CdMnTe/HgCdTe (a = 6.48A, E_G = 2.3 - 0 eV)
MnHgTe/MnHgTe (a = 6.45A, E_G = 2.3 - 0 eV)
ZnCdTe/ZnHgTe (a = 6.22A, E_G = 1.9 - 0.8 eV)

Of these materials, only a few are presently known to satisfy the requirement that the energy gap discontinuity occur principally in the conduction band. The most promising materials are the CdMnTe/HgCdTe, and the MnHgTe/MnHgTe systems. In the HgTe-CdTe system the valence band offset has been measured as 40 meV from optical measurements on SL structures,[6,7] and 0.35 eV from photoemission studies[8] on HgTe layers grown on CdTe. Despite the discrepancy these results both show that the concept can work in this and the CdMnTe system. For values of E_{G1} = 1.7 eV and E_{G2} = 0.8 eV a barrier height of ~1 eV will be needed in the conduction band, and the valence band offset will be <0.17 eV under the worse possible circumstances. This is not expected to be a serious block to hole transport in this structure. However, these material systems are not sufficiently well developed to grow these structures.

Conversely for the AlInAs/GaInAs and AlInSb/GaInSb systems whose material properties are technologically well advanced, and which are close to fulfilling the required conditions, the energy band difference does not occur principally in the conduction band. Capasso et. al., have proposed the doping interface dipole technique in which thin n- and p-type doping layers are placed on either side of the interface as a means of altering band edge alignments.[9] Thus, in this program an experimental study was undertaken of the materials technology required to control band edge alignments, so as to determine if this group of materials can be used for the above applications.

Because it may also be necessary to use slightly lattice-mismatched alloys to achieve the required energy gap alignments and to use lower n- and p-type doping concentrations which will produce longer depletion lengths a variable spaced superlattice was proposed as means of providing a method to inject electrons across the heterojunction. This structure was recently proposed by Summers and Brennan[10] and is shown in Figure 9 under zero and reverse bias. It consists of a variably spaced superlattice formed from alternating layers of a semiconductor of bandgap E_{G1} and a larger bandgap semiconductor or insulator of bandgap E_{G2}. These materials form the quantum wells (QWs) and barrier layers of the structure respectively, and must satisfy the condition that the conduction band edge discontinuity (ΔE_c) be large.

The SL structure is designed such that under reverse bias the levels in each QW are closely aligned with each other, and with the conduction band of the high gap material. This energy level scheme is obtained by a judicial choice of well thickness and barrier widths, such that electrons can tunnel through the first thin insulator layer into the first QW of the SL and then continue to resonantly tunnel from one QW to the next. Thus electrons are injected into the conduction band of the active semiconductor layer at an energy E_1 above the conduction-band edge, where E_1 is the energy of the first sub-band in the last quantum well. Throughout the structure, the QW widths are designed such that the bound states lie at an energy equal to the voltage drop between any two adjacent wells, and the barrier widths are optimized to enhance the resonant tunneling between adjacent wells. Thus the VSSEF device affords high-energy injection by providing a tunneling channel in a biased superlattice. An additional and equally important feature of this structure is that the distribution of hot electrons is nearly monoenergetic about the injection energy, thus greatly enhancing the efficiency of the impact ionization process.

The predominant carrier transport mechanism within the SL structure arises from resonant tunneling between the aligned quantum levels in adjacent quantum wells. Efficient high-energy injection is obtained by reducing the energy lost to phonon processes by channeling the electrons between adjacent quantum levels. Therefore, they cannot lose energy to phonons since no states are available for the electrons to be scattered into. The SL provides an alignment of successive quantum levels such that

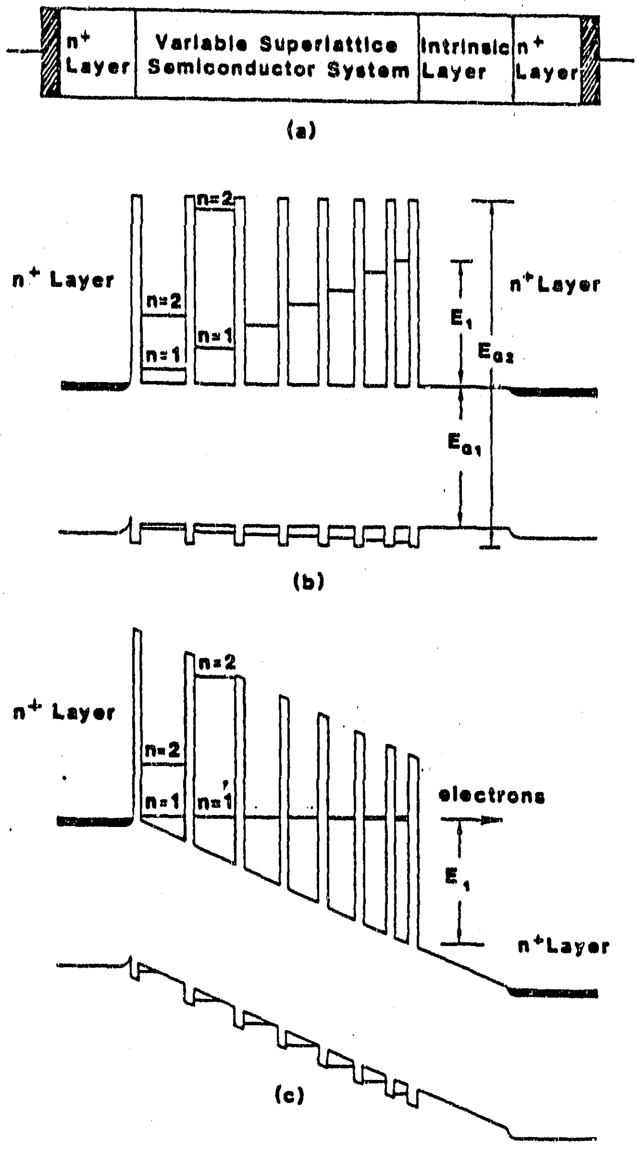

Figure 9. Illustration of variably space superlattice injection scheme (a) device geometry, (b) zero bias, (c) applied bias, $eV=E_1$.

the electrons continuously gain potential energy (the applied or built-in electric potential inverts the superlattice) until they are finally injected into the active semiconductor region at high kinetic energy. Upon injection into the semiconductor, the distribution is initially monoenergetic, broadened only by the quantum mechanical energy broadening of the levels.

In principle, the structure can be incorporated into either a PIN device or a conventional MIM structure. In the former case, it acts as a minority carrier device and has applications to optical and infrared detectors, and solar cells, whereas in the latter situation it behaves as a majority carrier device, thus enabling high electron densities to be injected into an "active" semiconductor layer. The critical issues concerning the operation and efficiency of the structure are therefore, the number of source electrons that can be injected into the SL, the width of the quantum wells required to produce the spatial quantization levels, the barrier widths needed to obtain effective resonant tunneling and the spatial and energy distribution of the electron population injection into the low-potential side of the structure. To accurately design these structures Brennan and Summers have recently developed a comprehensive resonant tunneling calculation for a biased SL[11] which was used for designing test structures. Essentially, this model corresponds to the Tsu and Esaki scheme,[12] but under bias.

From the above device description it is apparent that the VSSEF structure can be used as the electron injection structure for a p-n heterojunction (or conversely as the hole injection structure for a n-p heterojunction). The application of this concept to the heterojunction avalanche photodiode solar cell proposed by Pearsall is shown in Figure 10. For zero electrical and optical bias the band structure and band edge alignments will be determined by the continuity of the Fermi level throughout the structure, and thus the p- and n-type doping levels in the high and low band gap regions, respectively. Under optical illumination, the photon-excited electrons on the p-side will initially tunnel through the VSSEF by phonon-assisted tunneling. On emerging from the VSSEF structure into the n-side of the heterojunction the electrons will have an energy which has been designed to equal or exceed the threshold energy required to initiate impact ionization. For most III-V and II-VI semiconductors in which the hole effective mass exceeds the electron effective mass, this is approximately 1.1 E_{G2}. By this

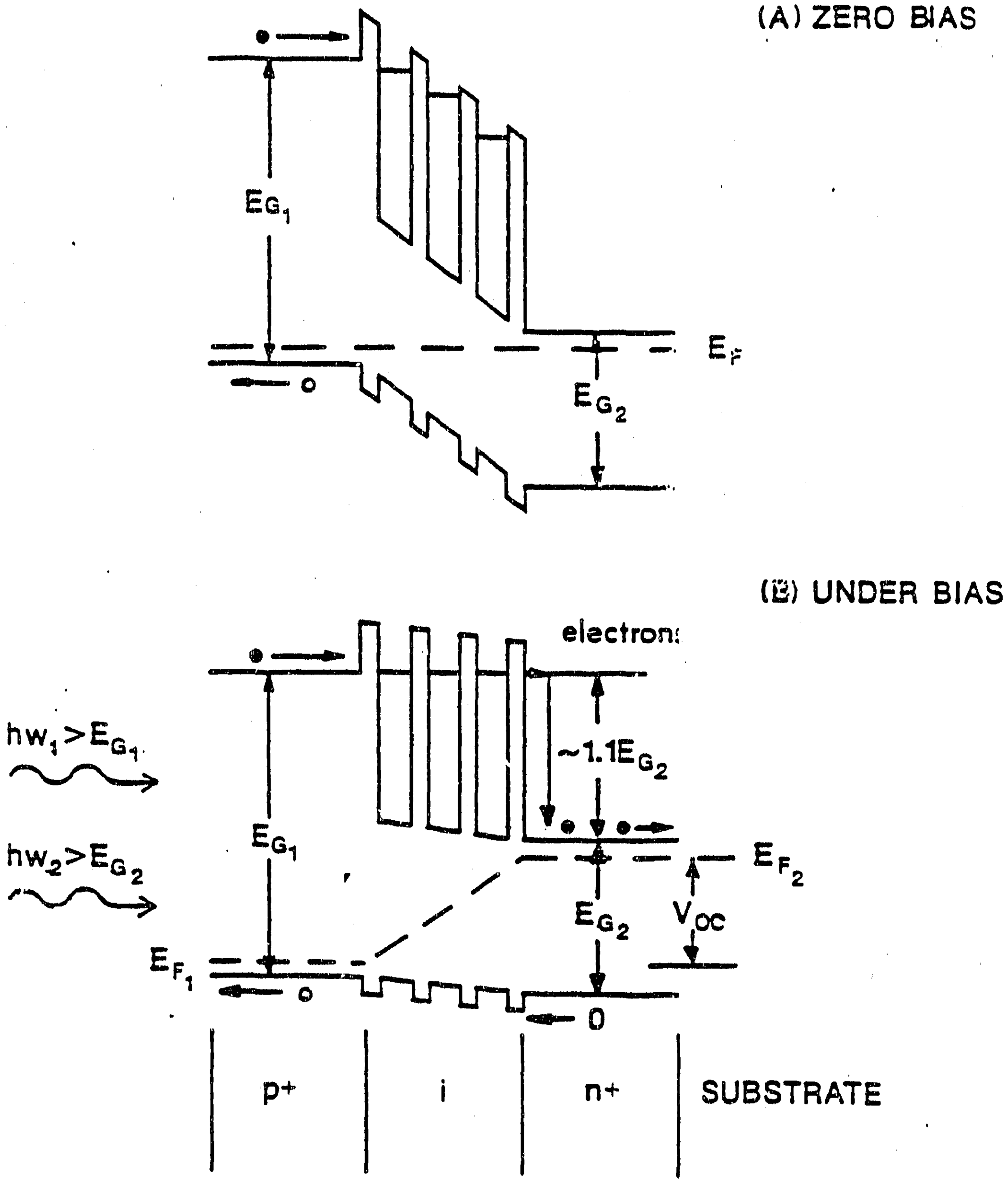

Figure 10. Solar cell with VSSEF structure in junction region.

means, the energy absorbed from high energy photons will be conserved. As a result of the current flow and external circuit, the band edge alignments will change until the steady state condition shown in Figure 10 are attained under full optical bias. For this condition the band edge alignments will result in the VSSEF structure becoming fully aligned, such that electrons will resonantly tunnel through the p-n interface into the low bandgap side of the junction.

As indicated by the figure, a solar cell effectively operates under forward bias conditions which are induced by the incident optical flux. This alters the energy band alignments between the two sides of the heterojunction, a fact that was not considered by Pearsall. From the analysis performed in Section 2.1, the highest efficiency is estimated to occur when $E_{G1} = 1.7$ eV, $E_{G2} = 0.8$ eV and $V_{oc} = 0.7 - 0.6$ V, and demonstrates that the barrier height for a viable structure are <1.0 eV. Possible efficiences can exceed 40% which makes this concept competitive with other proposed structures. It is also possible that higher efficiencies can be obtained by incorporating this concept with other methods of enhancing cell efficiency; or by possibly using a three bandgap cell.

Essentially the advantage of the VSSEF structure over a simple heterointerface is that it provides a conductive path for electron transport through the interface which can be made less abrupt. Thus electronic depletion effects are minimized, and if necessary, the transition region can be made longer by putting an intrinsic region between it and the doped regions so as to affect a smoother transition. This can be a very important factor in cell design. In the heterojunction scheme proposed by Pearsall high doping concentrations are needed to make the depletion length at the hetero-interface less than the phonon scattering length. However, high doping concentration also reduce the lifetime, mobility, and therefore the diffusion length of minority carriers.[1] Thus the collection efficiency of the junction can be reduced.

The VSSEF structure can, therefore, be used to minimize this conflict and also has the advantage that the built-in field acts on the carriers so as to accelerate them across the junction thereby moving them further from the junction interface. The transition region provided by the VSSEF also has beneficial effects in crystal growth. For example, the n-and p-type doping regions can be separated by a greater distance, thus minimizing profile broadening effects which can spoil the heterointerface due to impurity trapping. Also the VSSEF structure will act as a block to impurities and dislocations, and can be used to accommodate the rigorous requirement on lattice matching across the interface. This effect will greatly reduce the formation of interface traps which can provide a significant recombination path for the photo-generated electron-hole pair population.

2.2.1 Material Growth

Because of the need to obtain very abrupt and perfect interfaces for the heterojunction and VSSEF structures to be investigated in this program considerable effort was spent at the beginning of this program in refining MBE growth techniques and in developing a reflection high energy electron diffraction (RHEED) capability. As discussed by many investigators this is a powerful insitu characterization tool which can be used to both set up optimum growth conditions and to provide insitu measurements of the growth rate.

In this technique a 10 KeV electron beam is directed at a shallow angle to the growing crystalline surface such that the diffracted and reflected electrons form a pattern on a phosphor screen. The diffracted pattern can be related to the surface conditions such as crystallinity, surface composition, etc. Also the specular reflection beam during crystal growth exhibits an intensity oscillation which is indicative of layer by layer deposition of a thin film. As an example, Figure 11 shows the growth of GaAs, AlAs and AlGaAs during the deposition of 10 monolayers (ML) of material. From these figures the following information can be obtained.1.

The growth rate can be measured directly and instantly during deposition. In Figure 11 the growth rates are

R_{GaAs} = 0.505 ML/sec

R_{AlAs} = 0.219 ML/sec

$R_{Al_xGa_{1-x}As}$ = 0.746 ML/sec

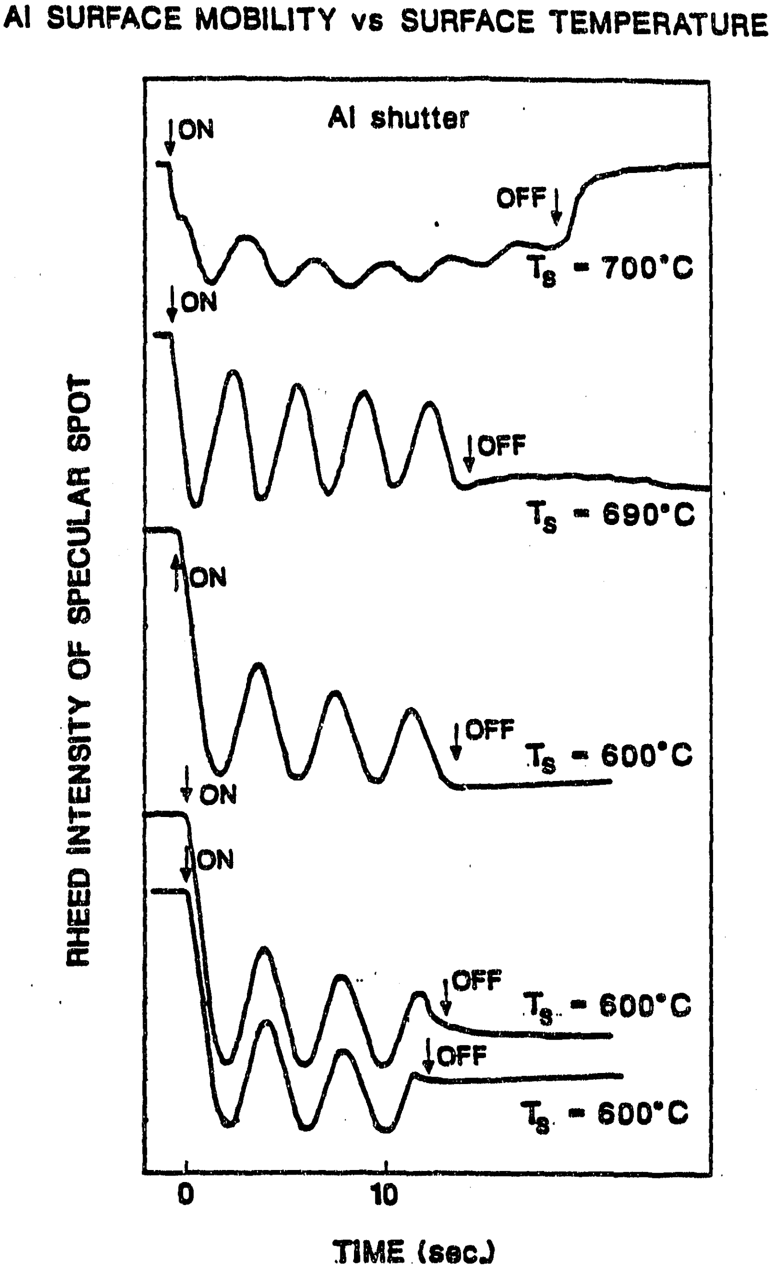

Figure 11. RHEED oscillations for AlGaAs, AlAs and GaAs growth.

2. The Al mode fraction can be obtained directly from the relationship

$$X=\frac{R_{AlAs}}{R_{Al_xGa_{1-x}As}}=0.302$$

3. Because the oscillations are directly related to the atomic layer deposition of the material, they can be used to grow quantum well structures with precisely known and predetermined widths and composition profiles.

The RHEED technique was also used to determine the optimum conditions for obtaining very smooth and planar interfaces. As can be seen in Figure 11 the amplitude of the RHEED oscillation decreases with time, i.e., the monolayers growth becomes less well defined as the deposition progresses. This is attributed to the roughening of the growth surface by the generation of many small islands. Essentially before the complete growth of one monolayer, island sites occur on the top of this layer and act as nucleation centers for the initiation of the next monolayer of growth. Hence, the maximum intensity never recovers to its original value. However, as shown by Figure 11, when growth is terminated by interrupting the Ga flux after many monolayers of growth, the specular spot intensity increases and approaches a value close to its original intensity. This effect is attributed to a smoothing of the surface by the surface diffusion of the atoms forming the island nucleation centers to the edges of each monolayer. Thus the surface becomes smoother and under the right conditions can produce very flat interfaces. This effort is very important for fabricating high quality multiple quantum well and superlattice structures.

The signal recovery time, i.e., the time required for surface smoothing has been shown to be very dependent on substrate temperature, and on the species of the group III element impinging upon the surface. Figure 12 shows the signal recovery for AlAs at 600°C and indicates that the AlAs surface shows no recovery effect at all. Thus, Al atoms on an AlAs surface at 600°C have no significant surface mobility. This figure provides an understanding for the accepted practice of growing AlAs on GaAs to obtain a sharp interface, rather than the reverse process. In order to investigate if higher Al surface mobilities could be obtained RHEED oscillations were studied at higher substrate temperatures. As observed from Figure 12 little effect was detected until a

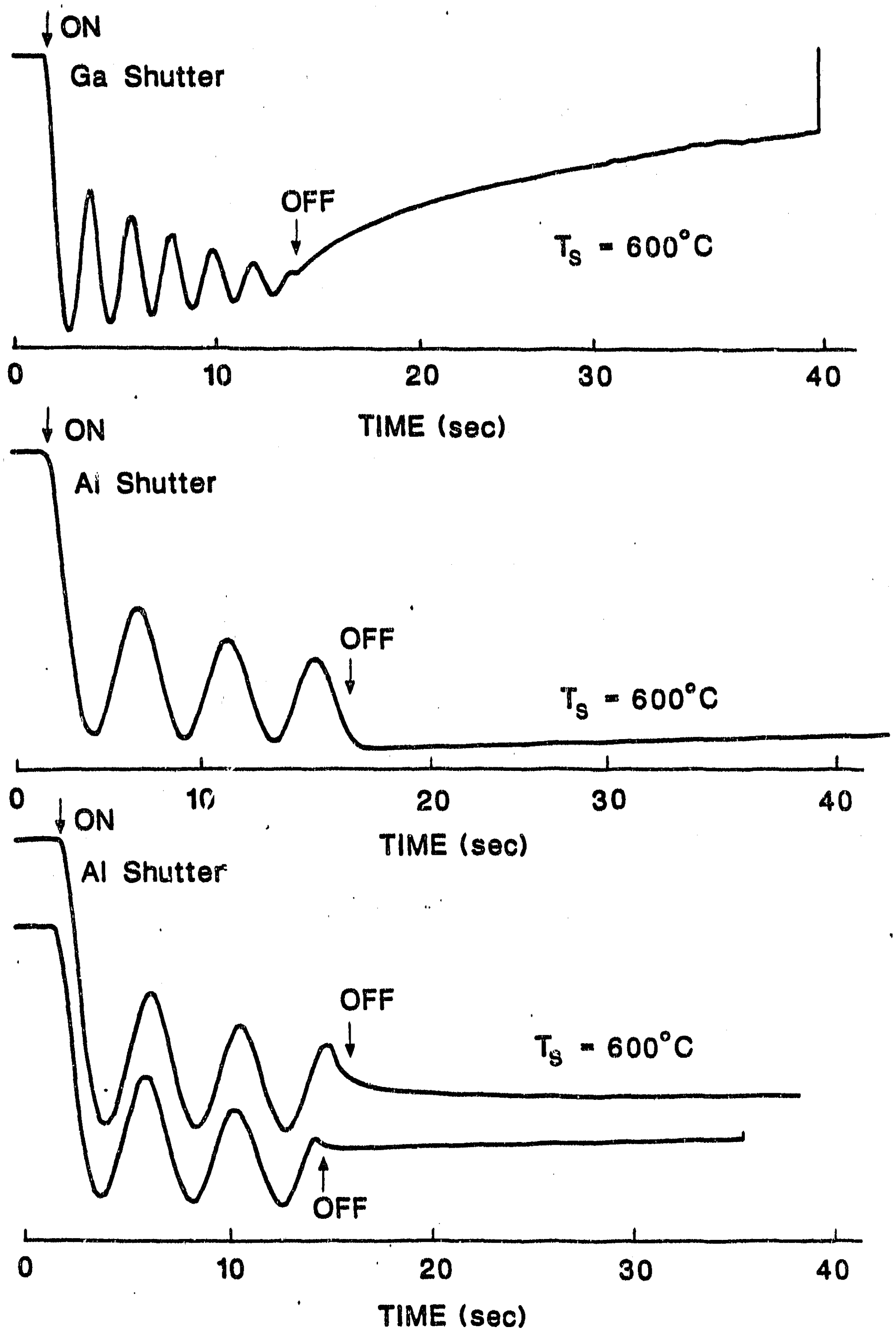

Figure 12. Al atom surface mobility vs. growth surface temperature.

temperature of 690°C was reached. At 700°C a strong increase in the RHEED intensity was observed within 10-20s and was attributed to surface smoothing, due to the high surface diffusion of Al. Thus for AlGaAs growth a more planar surface or interface is expected to be obtained at 700°C than at lower temperatures. For growth temperatures above 650°C it has also been reported that the Ga sticking coefficient decreases rapidly with increasing temperature and at 700°C and 750°C has values of approximately 0.75 and 0.50. Thus although more planar surfaces are obtained at 700°C the strong dependence of growth conditions on temperature requires very high temperature stability and accurate measurements of growth rate. From this analyses the following growth procedure was used to grow AlGaAs/GaAs multiple quantum well structures. The GaAs was grown at 600°C and the AlGaAs at 700°C with the growth being interrupted for 60s at each interface. This allows both the substrate temperature to be changed, and the surface to smoothen. At both of these growth temperatures accurate growth rate measurements were made using RHEED oscillations. Since the AlGaAs surface recovers upon interruption of growth, the migration of Ga atoms is attributed to the observed smoothening of the surface. This indicates that the deposition of AlGaAs on GaAs provides a sharp and smooth interface, while GaAs on AlGaAs will produce a rough interface, as has been previously suggested.

2.2.2 Variably Spaced Superlattice Structures

Using the theory described previously to design VSSEF structures capable of injecting electrons at relatively high voltages between 0.5 and 1.0 eV shows that very narrow quantum well widths are required and that for this situation the control over energy level positions becomes more difficult. It is, therefore, necessary to investigate structures in which resonant tunneling can be achieved between higher energy states in a quantum well, as then higher injection energies can be obtained for wider quantum well widths and more control is obtained over the VSSEF design. To date resonant alignment in these devices has only been observed between the n=1 levels in each quantum well. In this task of the program, therefore, a theoretical and experimental study was made of resonant tunneling in VSSEF structures in which alignment was designed to occur between the n=1 states in the first quantum well and the n=2 states in the second and third quantum wells. For these designs the same material parameters and theoretical calculations were used as described in an earlier publication.[13] Also all length parameters were calculated in multiples of the (001) layer atomic spacing, 2.8267 Å, so as to correspond to a practical situation.

In previous modelling studies it was found that a barrier width of 50.88 Å (18 ML) was the near optimum value to use for these structures. For narrower barrier widths the interwell interaction between energy states in adjacent quantum wells becomes strong enough to prevent close alignment. Essentially, as the levels are brought into alignment by the applied field, the overlap between the wave functions in adjacent quantum wells produces a strong repulsion between the symmetric and antisymmetric states of the structure which can separate these states by as much as 0.1 eV for small barrier widths. For barrier widths greater than 50.88 Å the separation between the symmetric and antisymmetric states was typically less than 0.005 eV, but the transmissivity of the total structure decreased rapidly for larger barrier widths. Thus in this work all barrier widths were kept at a constant value of 18 ML, although values of 18 ± 4 ML can be acceptable in multiple quantum well structures. The calculation was performed for $Al_xGa_{1-x}As$ barriers with an x-value of 0.35 corresponding to a conduction band discontinuity of 0.27 eV and the band parameters given by Adachi and Miller, et.al.,[14] i.e., electron effective masses of 0.067 m_o in the GaAs QWs and 0.096 m_o in the AlGaAs barriers, with nonparabolicity factors of 0.61 for GaAs and 0.484 for AlGaAs.

The first structure to be designed was, a two-well VSSEF in which the n=2 level in the second QW aligns with the n=1 level in the first QW under the appropriate bias, which was chosen to be 0.2 volts. This structure is shown in Figure 13 and demonstrates that resonant alignment is predicted for well widths of 67.84 and 98.93 Å (24 and 35 ML) respectively, for a $Al_{0.35}Ga_{0.65}As$/GaAs quantum well system. For a two-well VSSEF structure in which the resonant tunneling alignment was designed between n=1 states for a bias of 0.2 V the first and second well widths were 59.44 and 31.09 Å (21 and 11 ML), respectively. Thus a considerable increase in the total length of the structure can be obtained by using the n=2 state in the second well. Also because less voltage has to be dropped across the first quantum well, its width is increased because a lower energy level state is sufficient to achieve alignment with the lowest conduction band emitter states. The transmissivity of this structure as a function of the incident electron energy is shown in Figure 14 and peaks with a value of 10^{-3} at 0.02 eV. This value equals that obtained for the two-well VSSEF in which alignment is between the n=1 states in the first and second quantum wells, and demonstrates from a theoretical viewpoint that using higher quantum well states does not compromise the effectiveness of these structures. However, the observation of resonant tunneling in this structure does not necessarily experimentally confirm that electrons will be injected from the structure of an energy of 0.2 eV. Because electrons can only tunnel from the $E_{1,1}$ state into the $E_{2,2}$ state when the two states are brought into alignment by a bias voltage of 0.2 V, it is impossible from the I-V characteristic to distinguish if an electron in the $E_{2,2}$ state is directly transmitted through the last barrier at an energy of 0.2 eV, or first decays into the $E_{2,1}$ state before tunneling into the collector. The possibility of this second path occurring can be estimated from the characteristics of the structure and the mechanisms of the electron-phonon interaction in GaAs. From Figure 14 the separation between the n=2 and n=1 levels ($E_{2,2}$ - $E_{2,1}$) in the second quantum well is 0.11 eV. This energy difference is two to three times the longitudinal optical phonon energy in GaAs and thus it is possible for electrons in the n=2 state to decay into the n=1 state by LO-phonon emission. The probability of this occurring can be roughly estimated by comparing the time it takes for electrons to pass through the QW with the interaction time between these electrons and LO-phonons.

Because of the ambiguity of the two-well structure a three-well VSSEF was designed in which alignment was designed to occur between the n=1, n=2 and n=1 states in the first, second and third quantum wells, respectively. The purpose of using an n=1 state in the last well is to provide only one path for electron transmission through the structure. In this structure the last n=1 state essentially acts as a filter and only allows electrons which have resonantly tunneled into the $E_{2,2}$ state to pass completely through the structure by resonantly tunneling into the n=1 state in the third quantum well. The design for this structure is shown in Figure 15 and requires well widths of 73.49, 107.41 and 25.44 Å (26, 38, and 9 ML), respectively, to achieve electron injection at 0.2 V. Note that the structure is now 408.1 Å long and that all of

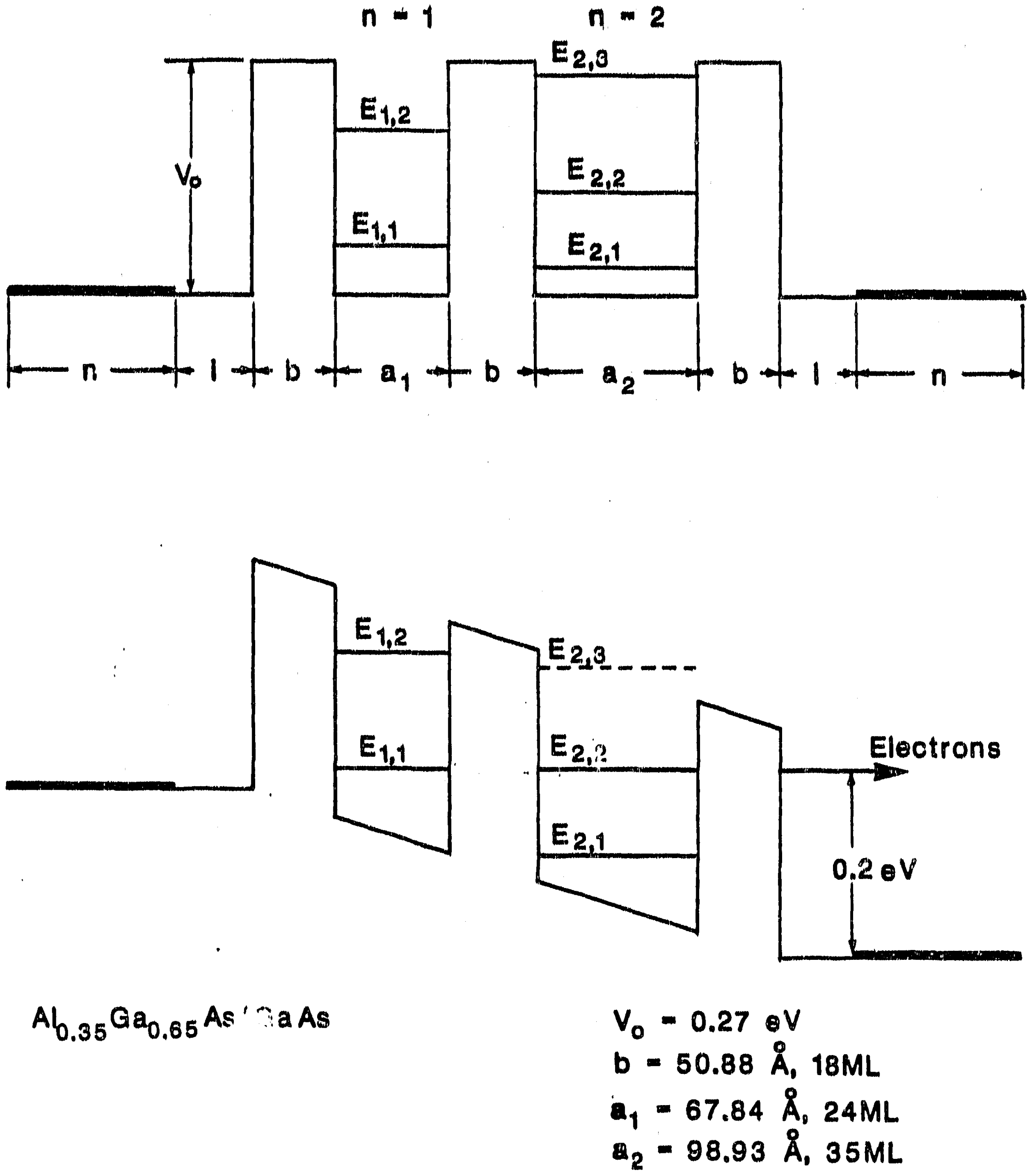

Figure 13. Two-well VSSEF structure designed for alignment of n=1 and n=2 states in the first and second quantum wells at an injector energy of 0.2 eV.

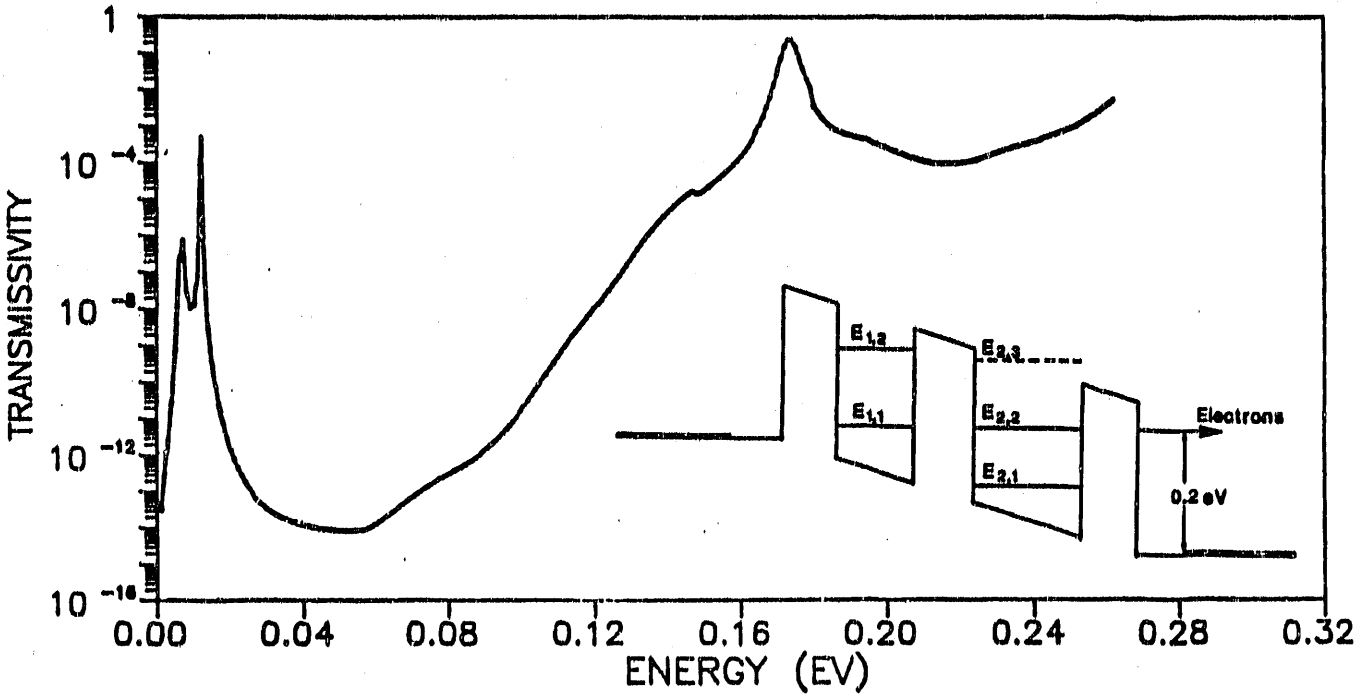

Figure 14. Transmissivity of two-well (n=1, n=2) VSSEF structure.

the wells are wider; because more voltage is dropped across the barriers and the wider second quantum well. The width of this well (107.41 Å) is estimated to be small enough to minimize electron-LO-phonon interactions and ensure a high transmissivity, close to that calculated by the simple theory. As shown in Figure 15 the transmissivity of this structure peaks at an incident emitter electron energy of 0.02 eV with a value (5×10^{-3}) very close to that obtained with simpler structures. Thus, this VSSEF design should provide a good test structure for determining the effect of LO-phonons on resonant tunneling in a multiple quantum well device. The peak transmissivity is assigned to the first QW and the two peaks at lower energy to the third and second QWs, respectively. This assignment was obtained by observing the changes that were produced in the transmissivity plots for small changes in the well width of each quantum well, and also by plotting out the wave function distribution at the energy corresponding to each peak in the transmissivity spectrum. For high emitter electron energies the transmissivity decreases rapidly. Thus, for energies between 0.25 and 0.35 eV, corresponding to bias voltages between 0.20 and 0.4 V, no electrons should be transmitted by the structure. The high transmission values obtained at energies of 0.142 and 0.168 eV correspond, respectively, to the n=3 and n=2 states, $E_{2,3}$, and $E_{1,2}$, in the second and first QWs, when biased by 0.2 V. The unity transmission observed for the $E_{1,2}$ state is a reflection of the fact that this energy is at a higher potential energy than the third and fourth barriers and, therefore, electrons passing through it pass over the rest of the VSSEF structure. However, it should be realized that these states are well above the conduction band minima where the electron density is very low and consequently negligible current is carried by these states.

To further explore the potential of these structures, three well VSSEF's aligned for 0.2 V bias using the n=1, n=1, n=2, and the n=1, n=2, n=2 levels in the first, second and third QWs were also investigated (see Figures 16 and 17). The well widths in the first of these designs were 73.49, 45.23 and 84.80 Å (26, 16, and 30 MLs), respectively. All of these distances are considerably less than the electron-LO-phonon interaction length in GaAs and make this structure an important consideration. However, its total length, 405.28 Å, is only 21% longer than that achieved (334.67 Å) using n=1 state alignments in a three-well VSSEF. In the second structure the well

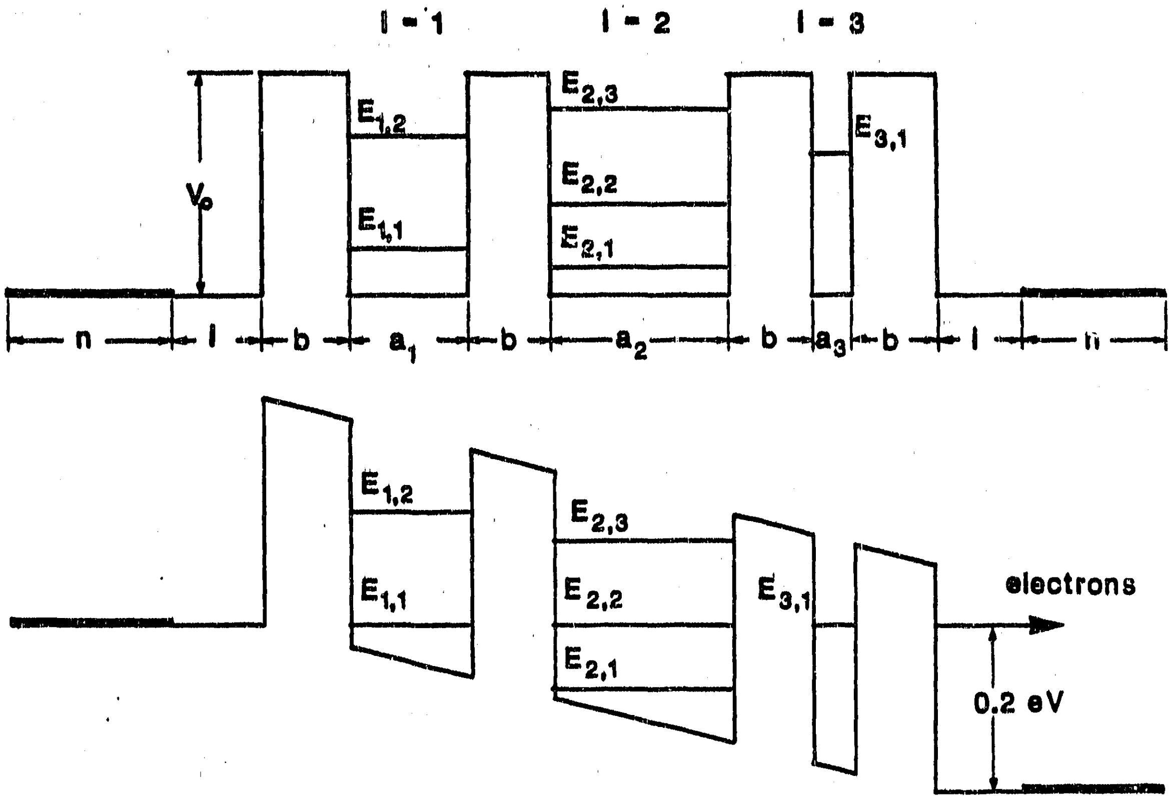

$Al_{0.35}Ga_{0.65}As/GaAs$

V_o = 0.27 eV

b = 50.88 Å, 18ML

a_1 = 73.49 Å, 26ML

a_2 = 107.41 Å, 38ML

a_3 = 25.44 Å, 9ML

Figure 15. Three-well VSSEF structure designed for alignment of n=1, n=2, and n=1 states in the first, second and third quantum wells at an injector energy of 0.2 eV.

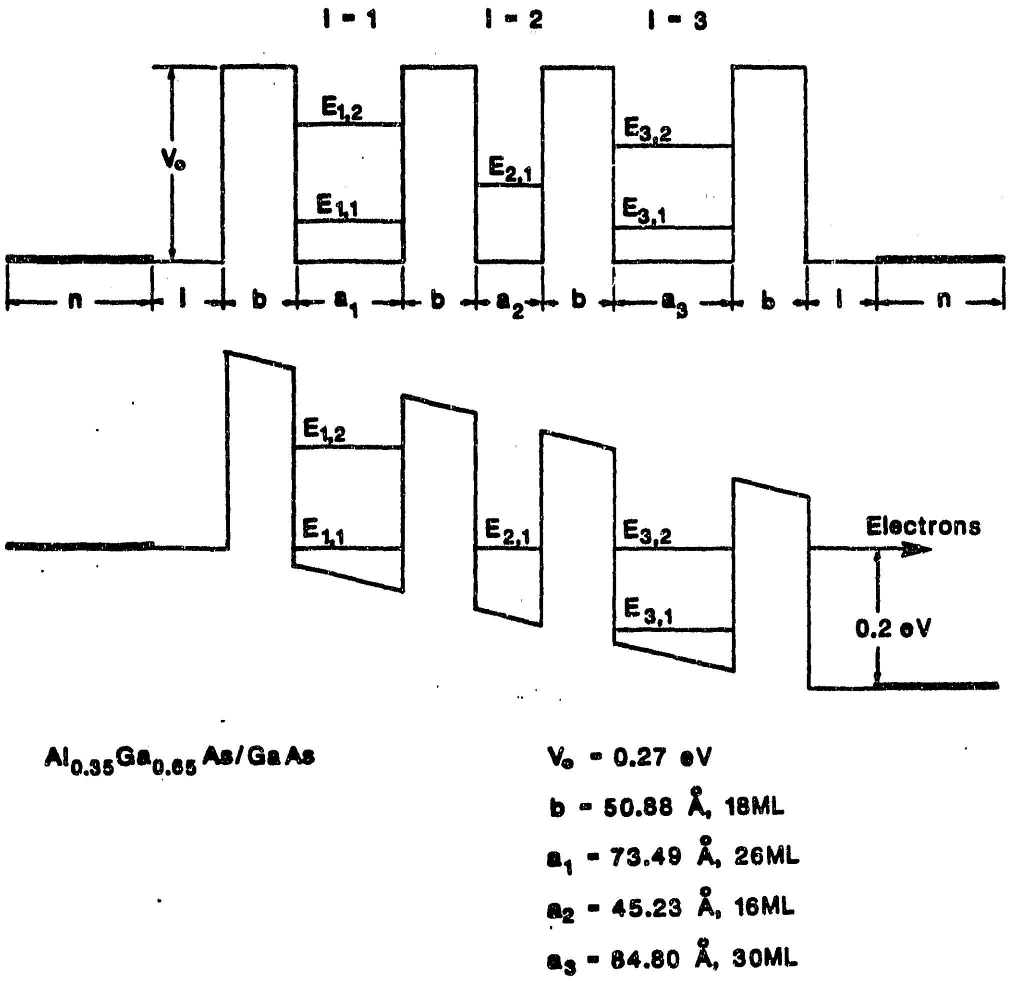

Figure 16. Three-well VSSEF aligned for n=1, n=1, and n=2 states.

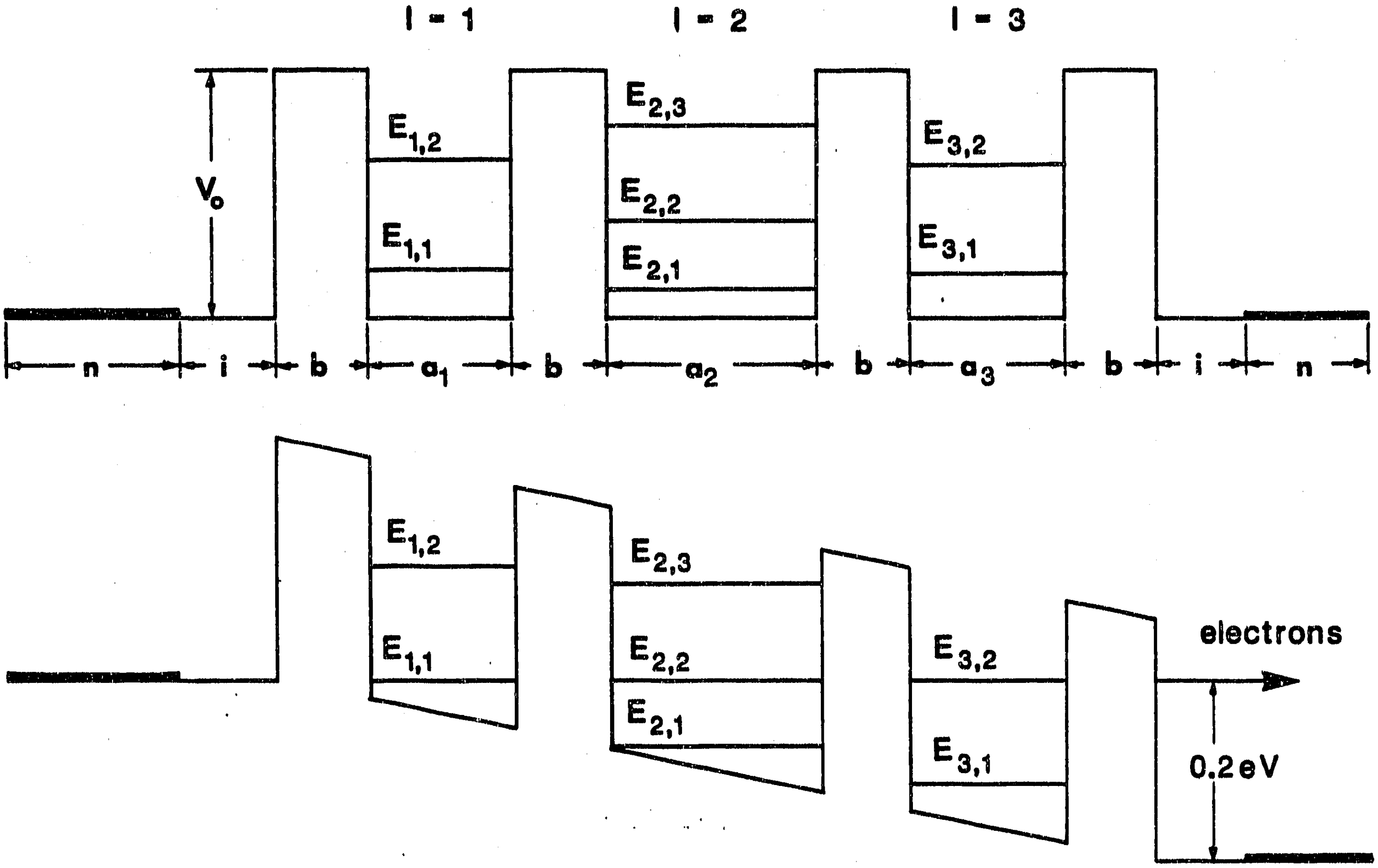

$Al_{0.35}Ga_{0.65}As/GaAs$

V_o = 0.27 eV

b = 50.88 Å, 18ML

a_1 = 79.15 Å, 28ML

a_2 = 115.89 Å, 41ML

a_3 = 84.80 Å, 30ML

Figure 17. Three-well VSSEF structure aligned for n=1, n=2, and n=2 states.

widths were 79.15, 115.89, and 84.80 Å (28,41 and 30 ML), respectively, producing a total device length of 481.6 Å. This is ~43.9% longer than the three-well (n=1,1,1) VSSEF and 99% longer than the two-well (n=1,1) VSSEF design whose total length is only 241.71 Å. The transmissivity calculations also show that very high transmission coefficients that equal or exceed those calculated for n=1 aligned structures can be obtained for all of these designs. However, it should be noted that this calculation does not take into account scattering effects which could occur in n=2 (or higher) quantum number states when the well width exceeds >100 Å. Finally to complete this investigation a two-well VSSEF device in which the n=2 state occurs in the first QW was designed. To achieve alignment at 0.2 V well widths of 138.51 and 28.27 Å (49 and 10 ML) were required in the first and second QWs, respectively. Table 1 summarizes the properties of the structures grown.

Following these theoretical design studies, devices were grown using the special interrupted growth techniques and temperature profiles described in Section 2.2.1 in order to obtain abrupt interfaces and to minimize the diffusion of Si into the barriers. Dopant diffusion into the barriers was also inhibited by reducing the dopant concentration from 5 x 10^{17} to 1.0 x 10^{17}cm^{-3} near the VSSEF structure and by the growth of a 50.88 Å wide undoped GaAs layer on either side of the structure. The actual structures, therefore, consisted of: 1) an n^{+}-substrate: 2) a doped 25 period 14 Å spaced AlGaAs/GaAs SL (to act as a diffusion and dislocation barrier) and a 0.7 μm GaAs layer doped from 5 to 1 x 10^{17}cm^{-3}: 3) a 50.88 Å layer of undoped GaAs: 4) the VSSEF structure: 5) a 50.88 Å layer of undoped GaAs: and 6) 0.9 μm of GaAs doped from 1 to 5 x 10^{17}cm^{-3}.

Following growth these structures were fabricated into mesa structures using conventional photolithographic techniques. The full details of this process are listed in Appendix I. Briefly, devices were fabricated by evaporating Au:Ge/Ni/Au metallization layers and ohmic contacts were formed by alloying at 380°C for two minutes in an inert atmosphere. This was followed by electroplating an overlayer of 1 μm of Au to increase the structural integrity of the device for the dicing and bonding steps. Mesas 20-50 μm in diameter were defined using conventional photolithographic techniques. The devices were then diced and epoxy bonded into an integrated circuit package and 0.7 mil Au

Table 1. Design Parameters of VSSEF Devices

For $Al_{0.35}Ga_{0.65}As/GaAs$ structures with:
b = 50.88 A,
V_b = 0.2 V, and
V_o = 0.27 eV.

Two-Well

First Well/Level	Second Well/Level
59.36 Å; n=1	31.09 Å; n=1
67.84 Å; n=1	98.93 Å; n=2

Three-Well

First Well/Level	Second Well/Level	Third Well/Level
67.84 Å; n=1	39.57 Å; n=1	25.44 Å; n=1
73.49 Å; n=1	45.23 Å; n=1	84.80 Å; n=2
73.49 Å; n=1	107.41 Å; n=2	25.44 Å; n=1
79.15 Å; n=1	115.89 Å; n=2	84.80 Å; n=2

leads were bonded to the top surface using a low pressure bonding procedure. The I-V measurements were performed either in a liquid nitrogen dewar or a Vari-Temp cryostat using a standard curve tracer. Figure 18 shows a reasonably good quality I-V curve that can be obtained by this simple technique. As the voltage is increased there is at first little current flow until the energy states approach close alignment with the emitter levels. The current then increases rapidly until all states are aligned. A further increase in voltage destroys the conditions for resonant tunneling resulting in a rapid decrease in the tunneling current. For higher voltages the current increases again when electrons can tunnel through the first few barriers and be emitted over the rest of the structure. The character of the negative resistance curve can be strongly influenced by the external measuring circuit and consequently display both external and possibly intrinsic bistability effects. To measure the true I-V characteristics it is, therefore, necessary to make sure that the device is completely stabilized. This was attempted in this program, but because of the high frequency response of these devices was more difficult than expected. As part of this work a special circuit for recording very accurate I-V and derivative spectra to give more information on the energy band structure of these devices was constructed and tested. Full details of this development are given in Appendix II. From this study some stabilization and understanding of the I-V characteristics was obtained so that more accurate data could be collected on these devices using the simpler curve tracer measurement technique. A more complete understanding of resonant tunneling and the bistability effects observed in these structures was not pursued, because at present it was considered to be outside the scope of this program.

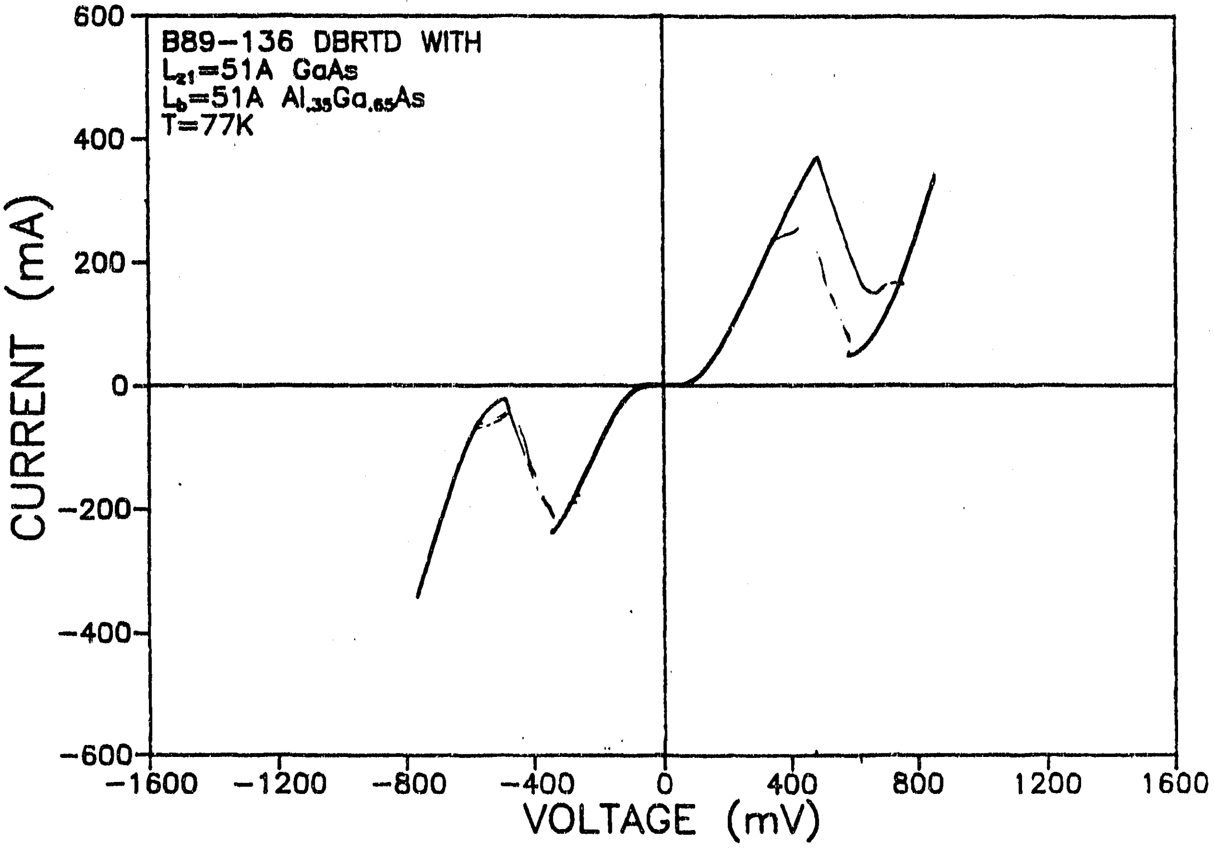

Figure 18. Current-voltage characteristics of double barrier quantum well structure.

2.2.3 Experimental Investigations of VSSEF Devices

The principal characteristics of these samples, the voltage and current values at resonant alignment and the peak current to valley current ratio, are listed in Table 2, in order of the growth run and are also shown in Figures 19 - 22. Table 2 shows that all but two of the samples exhibited very close agreement in the RT bias voltage position between ~0.42 - 0.66 volts. The second important fact to note is that the double barrier single quantum well device has the highest peak current value, with the two- and three-well VSSEF devices with all n=1 states in alignment having slightly lower current values of 220 and 275 mA, respectively.

Figure 19 shows the I-V curve measured at 300 and 77 K for the two-well (n=1, n=2) VSSEF structure with well widths of 24 ML and 35 ML of GaAs, respectively. Note that even at room temperature a clear negative differential resonance (NDR) peak was observed for forward bias due to transmission through the aligned $n_1 = 1$ and $n_2 = 2$ levels. At 77 K a good peak-to-valley current ratio of 6 was obtained. The NDR occurs at 0.44 V, even though the structure was designed to show strong transmission at a voltage of 0.2 V. This was attributed to the depletion region formed in the collector electrode due to the relatively low doping concentrations ($1 \times 10^{17} cm^{-3}$) near the VSSEF structures. Figure 19 also shows details of the I-V curve at lower voltages. Note that the NDR effects observed at lower voltages in both the forward and reverse directions occur at nearly the same bias voltage, of 50 and 75 mV, respectively. The small forward bias peak has a magnitude of 7.5 mA and is due to electrons directly tunneling into the ground state of the second well from the emitter and then out into the collector electrode. The small reverse bias peak with a magnitude of 13 mA, is attributed to electrons tunneling into the ground state of the wide well and then through the second well into the collector. The low peak currents reflect the fact that the transmission probabilities are low due to the thicker barrier plus well region.

As a test of the accuracy of the growth process developed for the VSSEF devices, the above two-well structure was also precisely grown in the reverse order, that is with $L_{W1} = 35$ ML and $L_{W2} = 24$ ML. Nearly identical results were obtained when the forward and reverse biases were interchanged, which was a strong indication of the precision of the model and the repeatability of the growth and fabrication steps.

Table 2. Experimental Values of VSSEF Devices at 77K.

Device No.	VSSEF Structure	V_p	V_p	P/V Ratio
B89-134	n=1, n=1 (59/31 Å)	450 mV	220 mA	7.3
B89-135	n=1, n=2 (68/99 Å)	425 mV	140 mA	5.5
B89-136	n=1 (51 Å)	430 mV	370 mA	7.8
B89-137	n=2, n=1 ( )	350 mV	115 mA	
B89-138	n=1, n=1, n=1	420 mV	274 mA	65
B89-139	n=1, n=2, n=1	570 mV	130 mA	5.2
B89-140	n=1, n=1, n=2	420 mV	90 mA	8

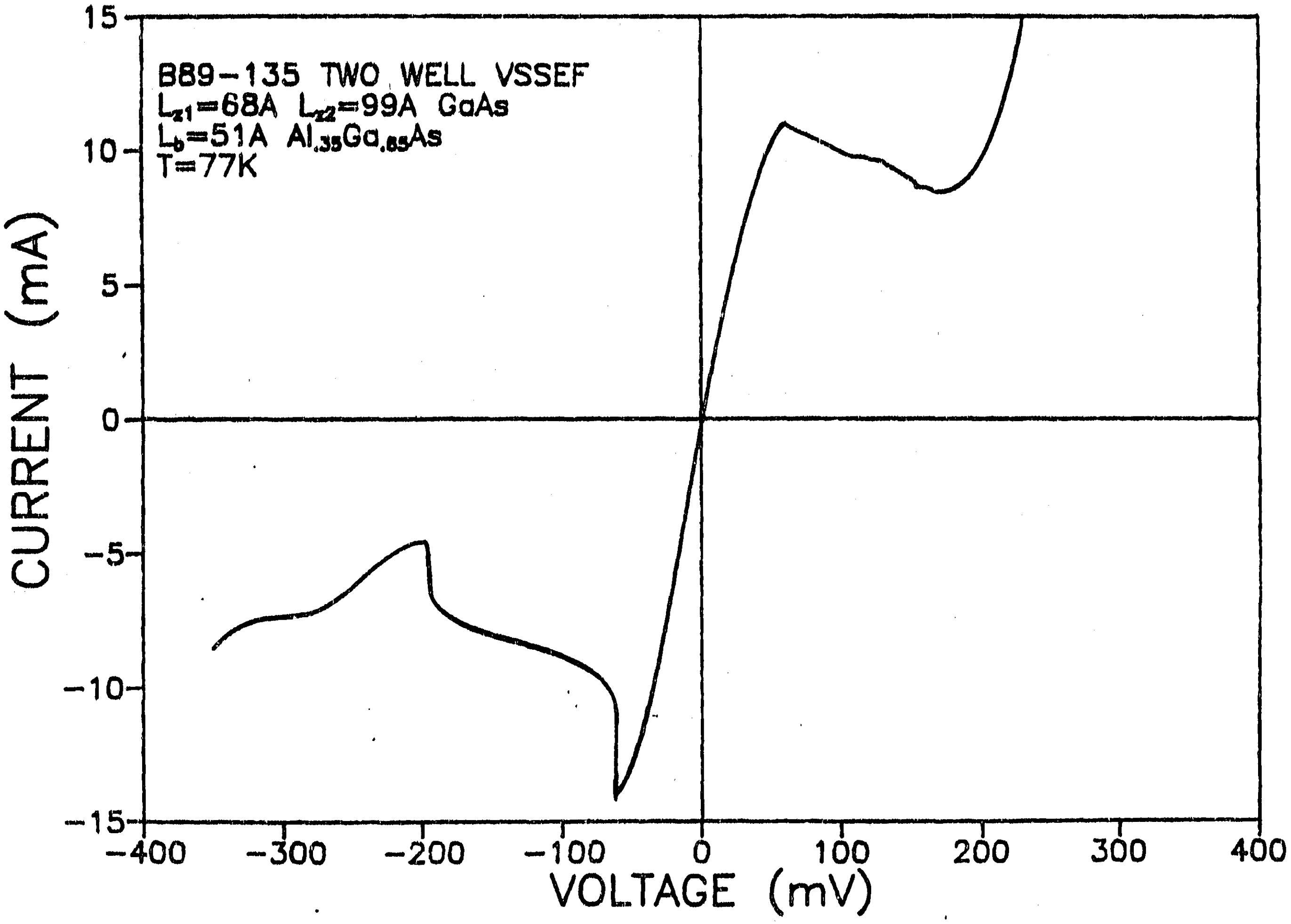

Figure 19. Current-voltage characteristics for a 0.2 eV two-well (n=1, n=2) VSSEF structure at 77 K.

Figure 20 presents the I-V curve for the three well structure with $L_{W1} = 28ML$, $L_{W2} = 38ML$, and $L_{W3} = 9ML$. At resonance bias, the $n_1 = 1$, $n_2 = 2$, and $n_3 = 1$ states are in alignment, which is evident by the I-V curve for this three well structure, shown in Figure 20. The room temperature peak to valley current ratio is ~2.0 and upon cooling increases to 5.5, mostly due to a decrease in the valley current. This indicates that at room temperature most of the current is carried by thermionic emission of hot electrons over the barrier structure. The valley current at low temperature, however, is attributed to tunneling via donor states in the barriers. At 77K a pronounced NDR effect is observed at 0.20 volts, associated with resonant tunneling through the VSSEF. The lack of additional features of the same magnitude indicates that the energy levels are aligned, and that resonant tunneling occurs according to the prediction of the model. A small peak in the forward direction at 0.38 V indicates that a small number of electrons can tunnel non-resonantly through the 28ML wide quantum well through the ground state of the second (35ML wide) and into the collector. This signal is not observed in the reverse bias direction, indicating that the transmission probability through the thin 9 ML wide well is much higher than the transmission probability through the 26ML well. Additionally, we have grown structures for $n_1 = 1$, $n_2 = 1$, $n_3 = 1$ alignment at specific bias, Figure 21. The I-V curves of these structures do not show any such small signal NDR effects in either the forward or reverse direction because no additional low energy states exists for tunneling. This supports the assignment of the origin of the small peaks in the I-V curve. Figure 22 shows similar data for the three well VSSEF structures with $n = 1$, $n = 1$, $n = 2$, and $n = 1$, $n = 2$ and $n = 2$.

For all of the VSSEF structures designed for resonant tunneling through an $n=2$ excited state, the maximum current values are observed to be approximately 50% lower than for the multiple well VSSEF devices. This lower value is, in fact, found to be approximately supported by the theoretical transmissivity curves shown in Figures 12 and 14 when compared to similar transmissivity curves that we have published for $n=1$ aligned VSSEF devices. It is also important to notice that the maxium current for the three-well VSSEF with resonant alignment between the $n=1$, $n=2$ and $n=1$ states in the first, second and third quantum wells has almost exactly the same magnitude (130

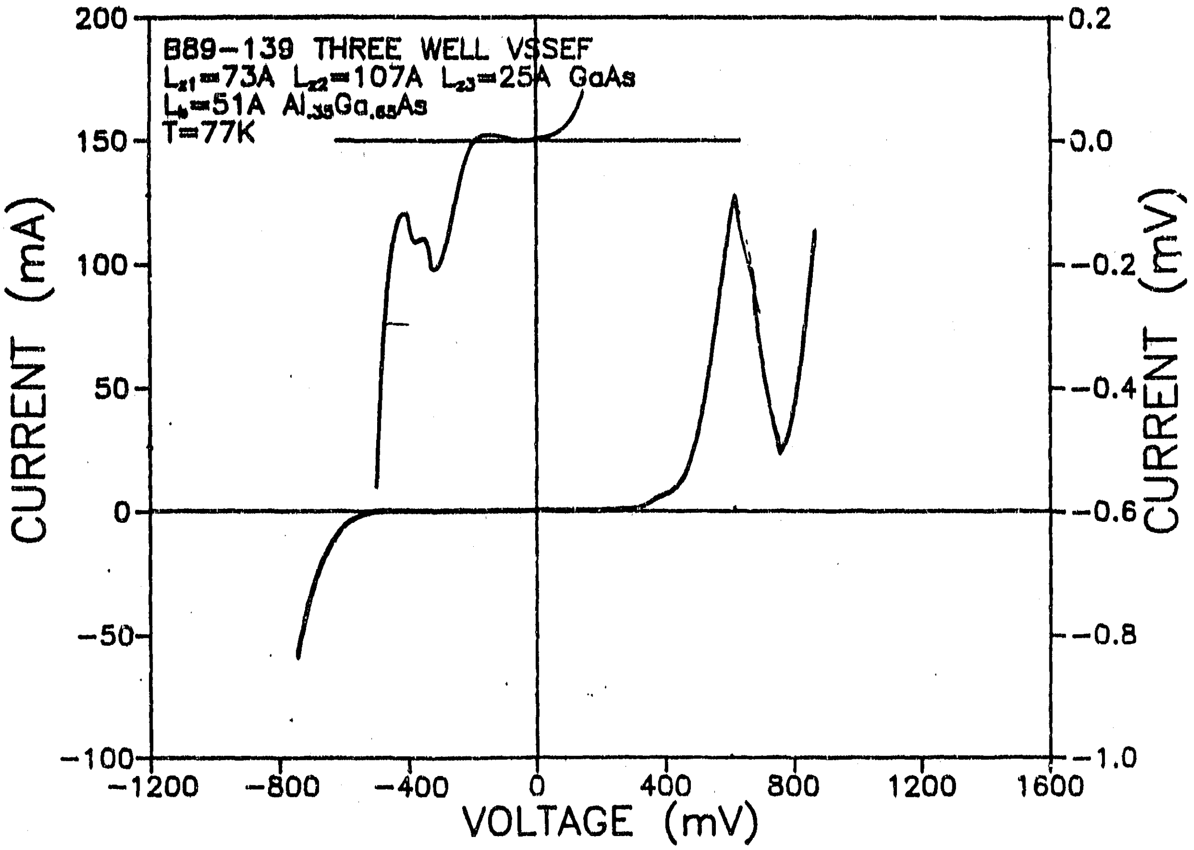

Figure 20. Current-voltage characteristics for a 0.2 eV three well (n=1, n=2, n=1) VSSEF structure at 77 K.

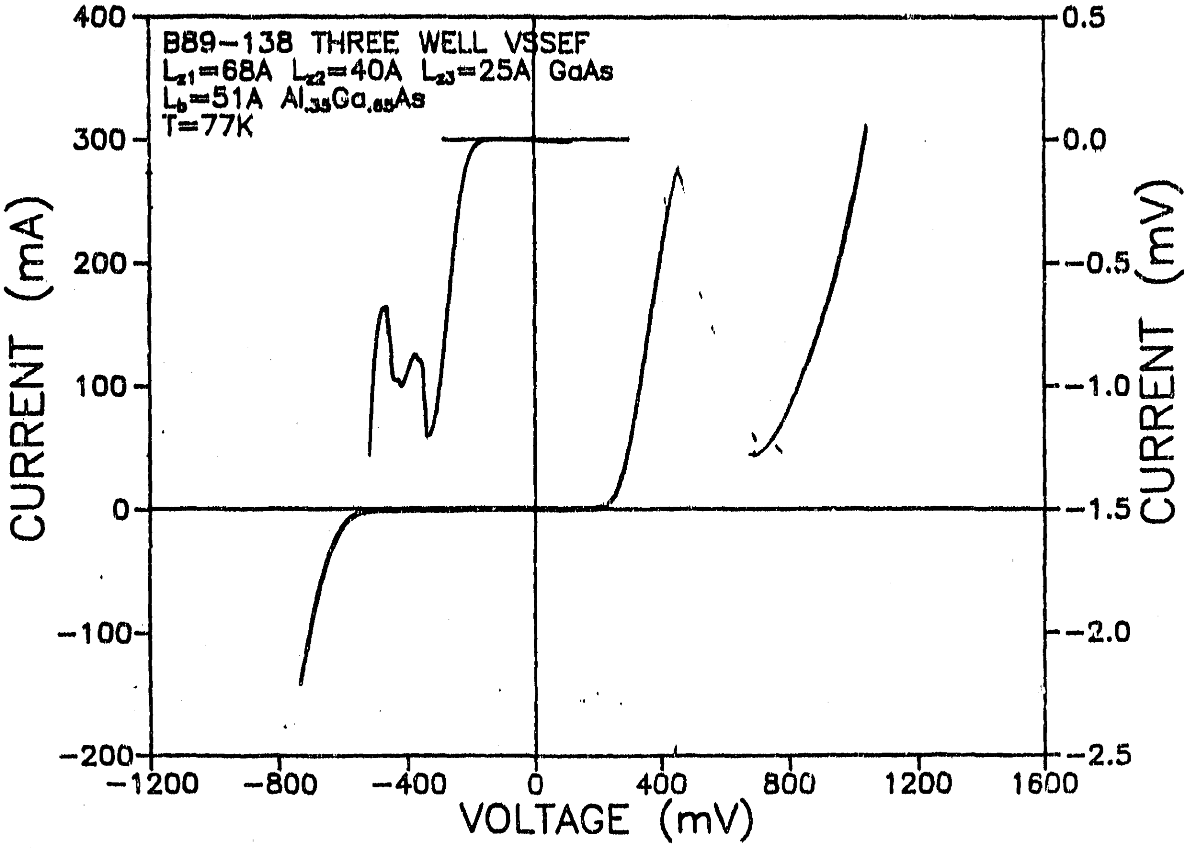

Figure 21. Current-voltage characteristics for a 0.2 eV three well (n=1, n=1, n=1) VSSEF structure at 77 K.

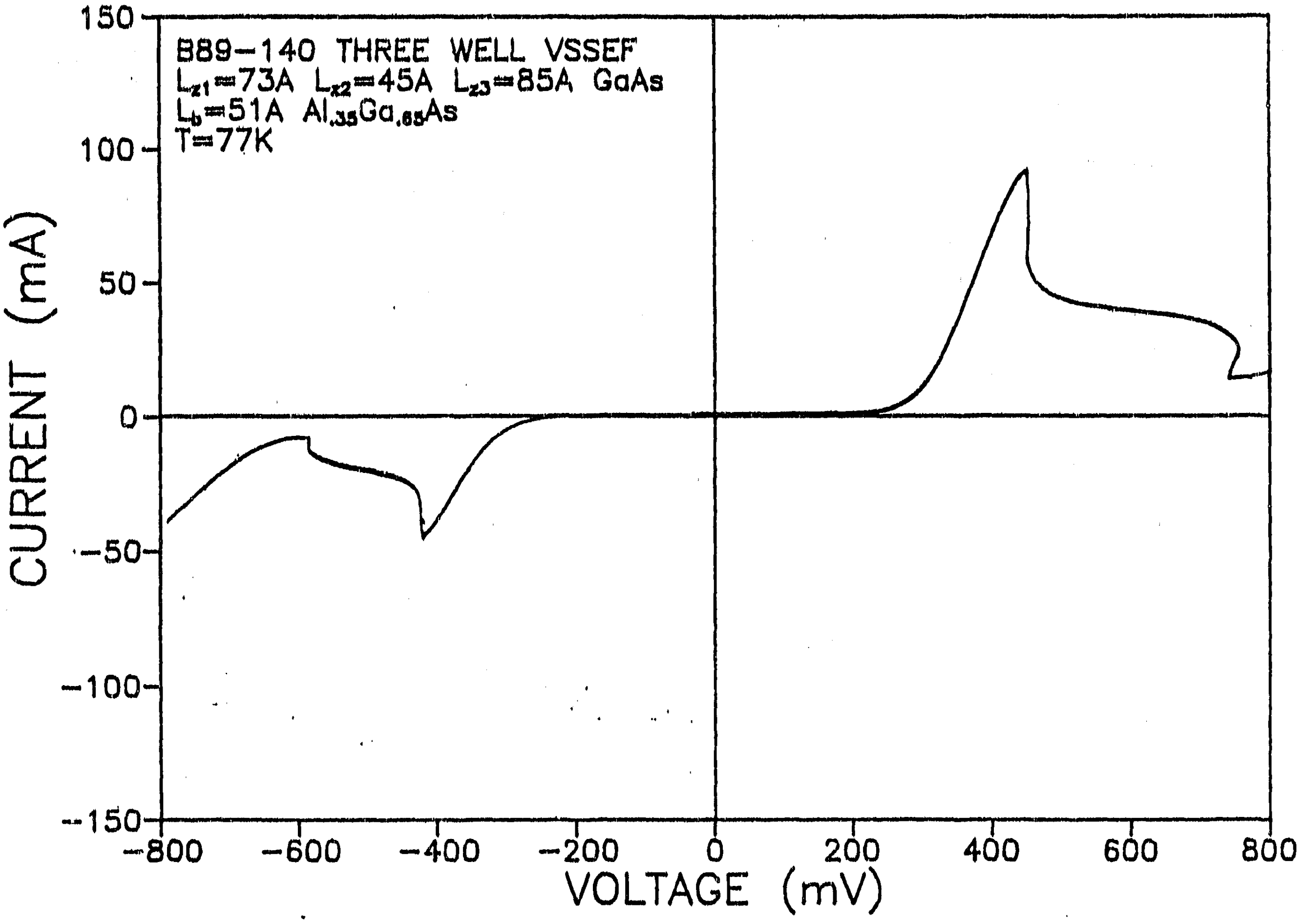

Figure 22. Current-voltage characteristics for a 0.2 eV three-well (n=1, n=1, n=2) VSSEF structure at 77 K.

mA) as that measured for the two-well VSSEF (140 mA) in which the resonant alignment is between the n=1, and n=2 states in the first and second quantum wells. Thus the filtering effect of the third quantum well state in sample B89-139 appears to have no measurable effect (within experimental error) on the transmission characteristics of the structure. This strongly suggests that resonant tunneling occurs very efficiently through the n=2 exicted quantum well states and that few electrons are captured by the lower n=1 state in the center well.

This observation is also supported by sample B89-137 in which the n=2 first QW, and the n=1 second QW states are aligned and the magnitude of the tunneling current is measured to be very close to that observed for the reverse situation. Additionally, validity to this conclusion is given by the high tunneling current values observed for sample B89-140 and B89-14 in which the n=1, n=1, n=2, and n=1, n=2, and n=2 states are aligned to give current values of ~90 mA. In addition, as discussed previously, the magnitude of the resonant tunneling current when only one quantum state is aligned with the emitter in two- and three-well VSSEF structures, as would have to occur if the electrons fell into the lowered state, is found to be one- to two-orders of magnitude less than when all states are in resonant alignment. These results strongly suggest that electron tunneling through excited states can occur with great efficiency, thus giving greater flexibility to the design of variably spaced superlattice structures and increasing their application to other devices. However, although this data supports the fact that electrons should tunnel straight through the complete structure without loss, the evidence for unbiased devices suggests that this is not obviously the case.

Recent calculations by Chamberlain et al.[15] indicated that the transition rate for the n = 2 to n = 1 inter-subband transition in a single 45 Å wide quantum well with 100Å wide barriers can be as small as 1.5×10^{11}sec^{-1} and increase to 10^{13}sec^{-1} in wider wells. These numbers correspond to lifetimes of 0.1 to 6 psec for electrons in the excited states of a quantum well. Model calculations by Choi et al. and fits to experimental data indicates 0.2 psec lifetimes for electrons in the excited states of a quantum well.[16] On the other hand the time for electrons to tunnel out of a double barrier single quantum well structure have been determined from measurements of the photoluminescence decay times by Tsuchiya et al.[17] and by Jackson et al.[18] In both cases decay times of >0.8 ns were measured for wells with barrier widths > 45Å. If the tunneling rate for excited states is of the same order of magnitude as it is for the ground state, then the probability of a transition to the ground state is much higher than the probability of transmission out of the quantum well. However, this is very unlikely as the double mode like distribution of the wave function for excited states results in a considerable extension of the wavefunction into the barriers. Thus in excited states the electrons are located close to the barriers and can more rapidly tunnel through them than for n=1 states. This should effect the transition rate by many orders of magnitude. There remains the possibility that the ground state can become totally populated without electrons in the n = 1 level leaving the well. Then the excited n=2 state will also become partially populated and carriers can travel through this state into the next well and out to the collector.

A point to be noted is that the calculations by Chamberlain et al. and the experimental results of Jackson et al. and of Tsuchiya et al. have been carried out at zero bias conditions and the transmission rates should be different for a device under a bias. However, the data of Choi et al. which are for a device under a bias indicate that the rates should not be substantially different to alter out results. This view is further enhanced by a simple calculation of the transmission coefficient out of well into the electrode of the form $T \alpha e^{-2bk}$, where k is the electron momentum vector along the current direction and b is the difference in barrier height and electron kinetic energy. Thus the tunneling probability of an electron out of a well into the electrode is much greater than its tunneling probability into the neighboring well, if all else is kept constant.

2.2.4 Dipole-Interface-Doping Studies

Because of the need to tailor the band edge alignments in these structures an investigation was also made of the technique of dipole-interface-doping (DID). In this technique a sheet of acceptors and donors of exactly equal carrier concentrations are placed at equal distance on either side of a heterojunction. If the thickness, t, of the doping sheets are kept below 100 Å, then both are fully depleted of free carriers.

Essentially, the electrons on the donor atoms transfer to the acceptor atoms so that sheets of positively charged donor atoms and negatively charged acceptor atoms are formed in the crystal. Consequently, the DID structure acts as a microscopic capacitor. The electric field, F, between the two doping sheets is then

$$F=\frac{\sigma}{\epsilon_s\epsilon_o}=\frac{eNt}{\epsilon_s\epsilon_o}$$

where σ is the total charge within each sheet and the potential difference, $\delta\phi$, across the structure is:

$$\delta\phi=\frac{\sigma}{\epsilon_s\epsilon_o}\bullet d$$

For distances far removed from the DID, the potential across the DID structure appears to effectively shift the relative alignment of the valence and conduction bands such that the effective discontinuity in the conduction band at the heterojunction is increased for the doping scheme depicted in Figure 23.

Thus, the DID technique can be used to enhance or decrease the conduction band discontinuity in a heterostructure. It should be noted that the opposite effect will be induced in the valence band. For doping concentration of $5\text{x}10^{17}\text{cm}^{3}$ in 100 Å thick sheets separated by 200 Å (each 100 Å from the interface), the DID technique can produce a potential difference of ~0.14 eV. Consequently, for the AlGaAs system in which the highest n-type (Si) doping concentrations that can be achieved without impurity segregation are of the order of $5\text{x}10^{18}\text{cm}^{-3}$; offsets of the order ~1.0 eV could be obtained.

2.2.5 Pulse and Delta-Doping Studies

From these previous discussions it is obvious that the DID scheme requires that the doping be confined to a thin layer near the AlGaAs/GaAs interface. Also to increase the conduction band offset requires heavy p-type doping in the AlGaAs layer and n-type doping in the GaAs layer and exact compensation between the n- and p-type doping. Studies were, therefore, performed to accurately calibrate the growth procedure for these structures.

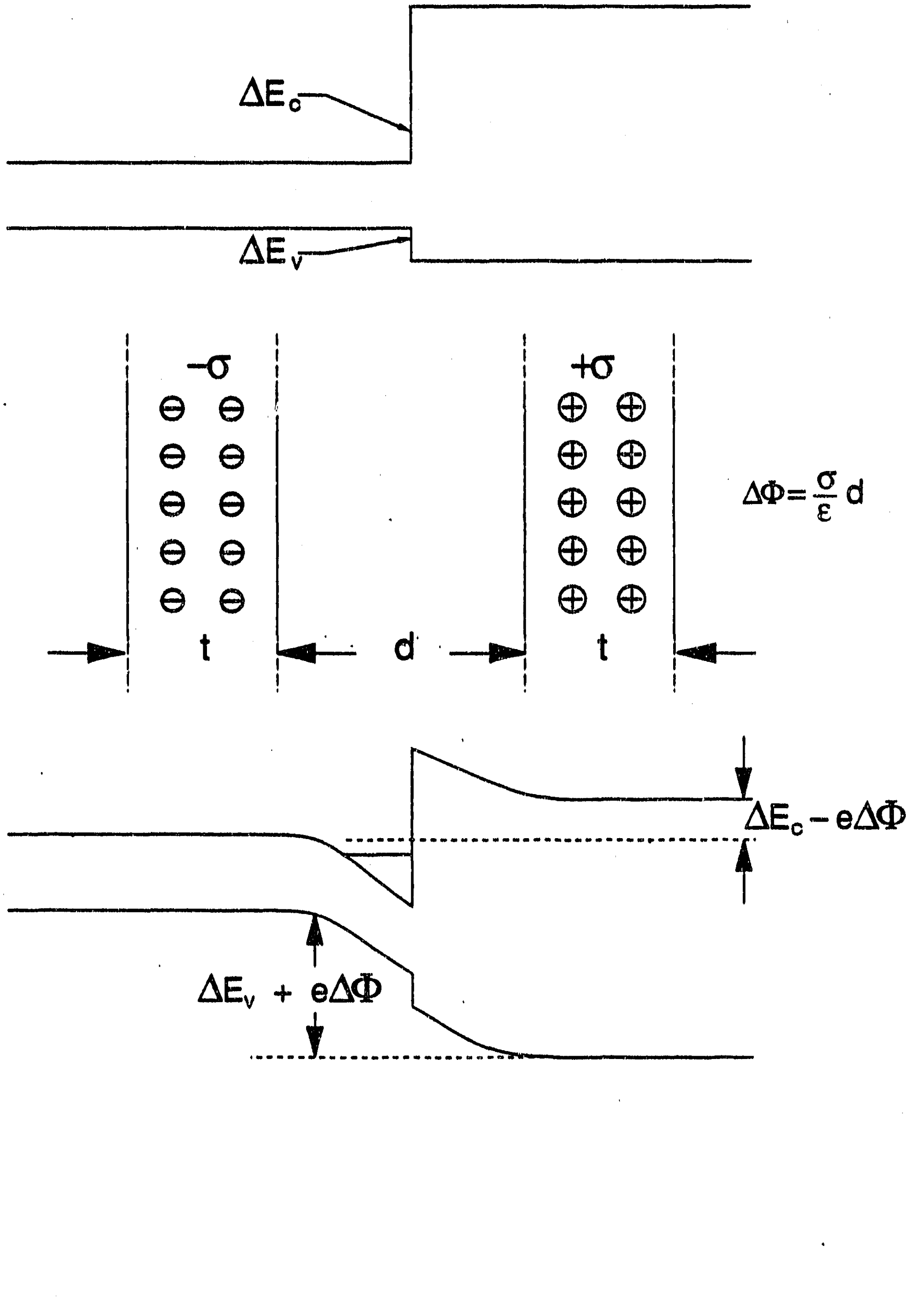

Figure 23. Dipole-interface-doping scheme to increase bandgap discontinuity.

The first doping experiments were step doping studies in which the dopant concentration was instantaneously raised from ~1×10^{17}cm^{-3} to ~1×10^{18}cm^{-3} for 0.5 μm of GaAs growth and then reduced back to 1×10^{17}cm^{-3} for a further 0.5 μm. This structure was used to enhance the Polaron measuring technique which measures the results of the doping run. For these doping concentration levels, the depth resolution of the Polaron technique is ~500-1000 Å, which is close to the best resolution possible by an electrical measuring technique. The results of this investigation showed that the first "interface" was smeared over ~0.2-0.5 μm, whereas the second interface was very abrupt. Reducing the growth temperature from 600°C to 520°C resulted in no change to the shape of the profile.

Because of the problems experienced in growing and analyzing the step doping profiles, work was initiated on delta-doping. Recently this doping scheme has been investigated and analyzed by many authors[19-30]. In this scheme a high dopant concentration is introduced as a very thin sheet in the semiconductor and can produce very narrow carrier profile widths and increased doping density. For doping GaAs with Si this technique could, therefore, be very useful as at high doping concentrations (5 x 10^{18}cm^{-3}) Si becomes amphoteric and auto-compensation takes place. Also surface segregation and bulk diffusion increases as the doping concentration increases, and thus it is more difficult to obtain controllable dopant profiles. Therefore a spatially well confined doping technology will enable very high fields to be obtained and overcome any material problems such as segregation. The technique is relatively simple, growth is interrupted by shuttering the Ga flux and waiting for the surface to become smoother. For these experiments an interrupt time of 60s was used as determined from the RHEED studies performed earlier. The Si flux was then turned on for a given time before being shuttered and growth resumed. Thus, a high density of Si atoms were substituted onto a single Ga plane. Throughout this procedure the As flux was maintained to prevent any loss of As from the growth surface. The time, t, that the surface is exposed to the Si flux, and the magnitude of the Si-flux, F_{Si}, determine the total dose, N_d, deposited, according to the relationship:

$$N_d = F_{Si}\, t.$$

The accuracy in determining N_d, therefore, depends on having a precise value for the Si flux rate. This is normally too low to measure accurately by the nude ion gauge in the growth chamber, and so was obtained by bulk doping GaAs and measuring the resulting carrier concentration, n by Hall effect measurements. The relationship between n, and F_{Si} is simply:

$$n=\frac{F_{Si}}{R}$$

where R is the growth rate which was accurately measured from RHEED oscillation measurements.

To obtain a high degree of self consistency in the calibration for N_d, special structures were grown. The magnitude of F_{Si} was obtained by doping the GaAs layer during continuous growth for 0.2 μm and then performing the delta-doping after growing approximately 1 μm of undoped GaAs. After delta-doping, 0.2 μm of undoped GaAs was grown, followed by a further 0.1 μm surface layer of doped GaAs. This layer was used to control (reduce) the surface depletion length so that C-V measurements could be used to measure the doping profile. The optimum doping concentration of this layer was established to be ~2.3×10^{17}cm^{-3}. A schematic of the actual device profiles grown to investigate delta-doping is shown in Figure 24. Initially eight samples were grown for a range of substrate temperatures and doping levels to investigate the effectiveness of this technique (Table 3). Because of the success of the initial study, a special study was then initiated to determine the practical limits of this doping technique. The structure used for these -doping studies is shown in Figure 25. A 100 nm thick buffer layer of GaAs was followed by a short period GaAs/AlGaAs superlattice buffer, a 250 nm Si doped GaAs calibration layer and a 500 nm undoped GaAs layer. Five periods of δ-doped GaAs each separated by 51 nm of undoped GaAs were then deposited. A 25.5 nm thick contact layer of n-GaAs doped at $N_d = 1.9\times10^{17}$cm^{-3} completed the structure. Before each δ-doping deposition, the growth was interrupted to obtain a smooth GaAs surface. The interruption time was again determined from RHEED surface recovery time experiments to be > 30s at a growth temperature of 540 °C. At lower growth temperatures this time was longer, thus we used a 60s interruption time for all growth temperatures <520°C. The Si source temperature was

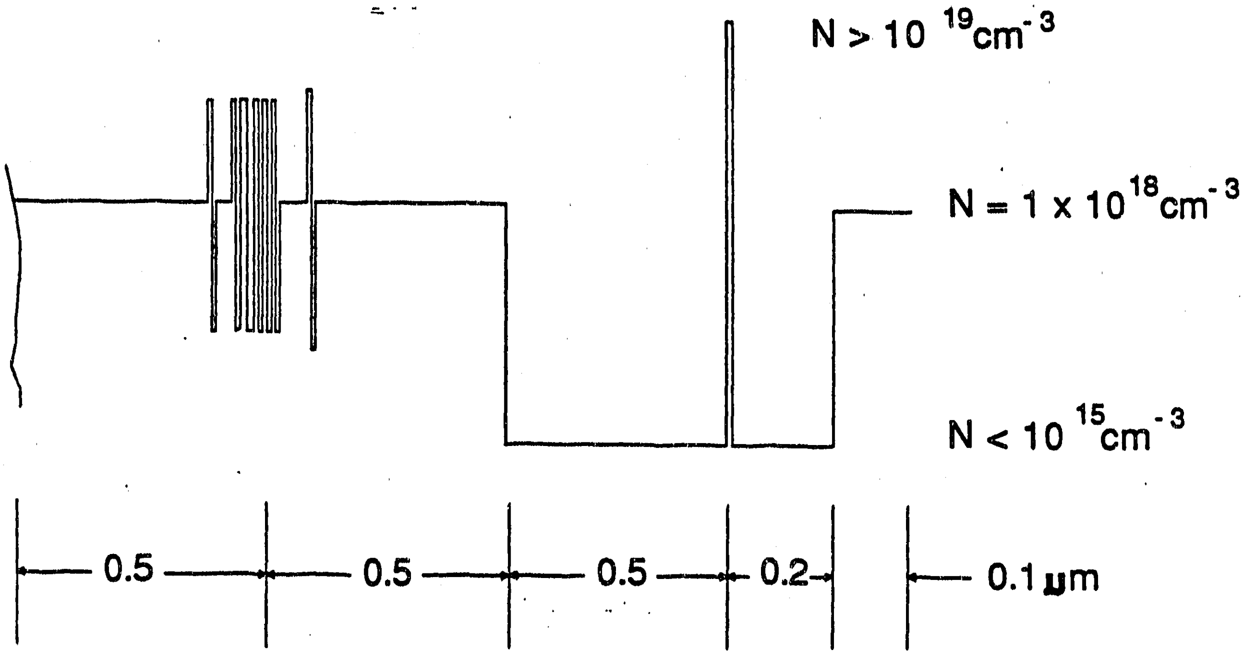

Figure 24. Delta Doping Structure for δ-doping study.

Table 3. Properties of samples studied for initial delta doping study.

RUN NO.	DOPING CONDITIONS		Spacer-layer μm	T_{ss} °C	Pause S
	δ-peak	surface			
183	5.0×10^{18}	5.0×10^{18}	0.5 μm	520	50s
184	5.0×10^{18}	5.0×10^{18}	1.0 μm	560	50s
185	5.0×10^{18}	5.0×10^{18}	1.0 μm	590	50s
186	5.0×10^{18}	5.0×10^{18}	1.0 μm	520	50s
188	5.0×10^{18}	3.0×10^{17}	1.0 μm	600	50s
189	2.2×10^{18}	3.0×10^{17}	1.0 μm	520	50s
190	2.2×10^{18}	3.0×10^{17}	1.0 μm	560	50s
192	2.2×10^{18}	3.0×10^{17}	1.0 μm	560	70s

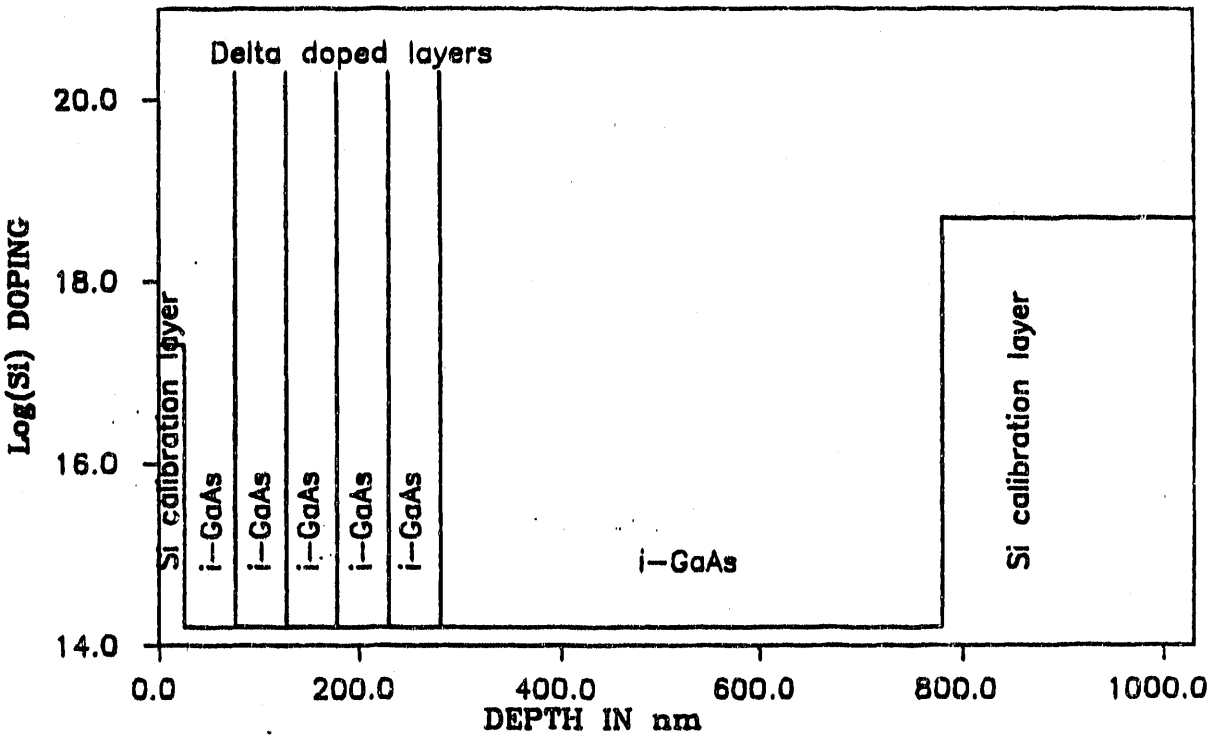

Figure 25. Delta doping structure containing five Si planar doped layers separated by 51 nm of GaAs.

set to produce a flux of $J_{Si} = 6.85 \times 10^{10}$ Si cm^{-2}s^{-1}, which corresponded to a bulk doping concentration of $N_D = 4.85 \times 10^{16}$ Si cm^{-3}. Under these growth conditions 90s of sheet doping produced a sheet density of $N_s = 6.17 \times 10^{12}$ Si cm^{-2}.

The dopant concentration profiles were first measured by secondary ion mass spectrometry (SIMS) using a 6 KeV, 300 nA oxygen beam. These conditions were selected to reduce knock-on and radiation damage effects and thus to minimize profile broadening induced by the ion beam. Next, electrochemical C-V profiling[31] was employed to measure the carrier concentration profiles as a function of depth. Etch steps of 1 nm width were selected to obtain high spatial resolution for each δ-doped profile.

The SIMS profile for a five period δ-doped sample grown at 520°C is presented in Figure 26. Only four of the peaks were measured and are shown in the figure. These peaks were slightly skewed in the sputtering direction due to the knock-on effect, which is inherent in SIMS measurements. The extent of the skewing was dependent on the ion beam energy and was noted by comparing the number of data points to the left and right of each peak. The SIMS profile indicates that the measured width of the δ-doping was independent of the position of the sheet doping in the material and was determined to be 9.0 nm at 50% of peak height and 18.0 nm at 90% of maximum peak height. In the best profile measured by SIMS, we obtained a FWHM of 6.3 nm for Si δ-doping in GaAs. The crater made by the SIMS ion beam was measured by using a Tencor Alpha step profiler and found to be very smooth and nearly flat, indicating a uniform ion beam. This measurement also provided the means for verifying the depth of the peaks. The high background count was due to the presence of Al in the SIMS system. Since many parts of the ion gun are made from Al, a large signal from Al withatomic mass of 27 is present which overshadows the smaller signal from Si of atomic mass of 28.

Figure 27 shows a electrochemical C-V profile of the same sample. Five narrow peaks due to Si doped layers were observed, however the position of the peaks are displaced by up to 12 nm. This was attributed to the large depletion width in the C-V technique, even though the surface was doped at 1.9×10^{17}cm^{-3}. Comparison of the data points to the right and left of each peak also exhibits the effect of the depletion width on the profile. Table 4 presents the results obtained from Figure 27 which shows that

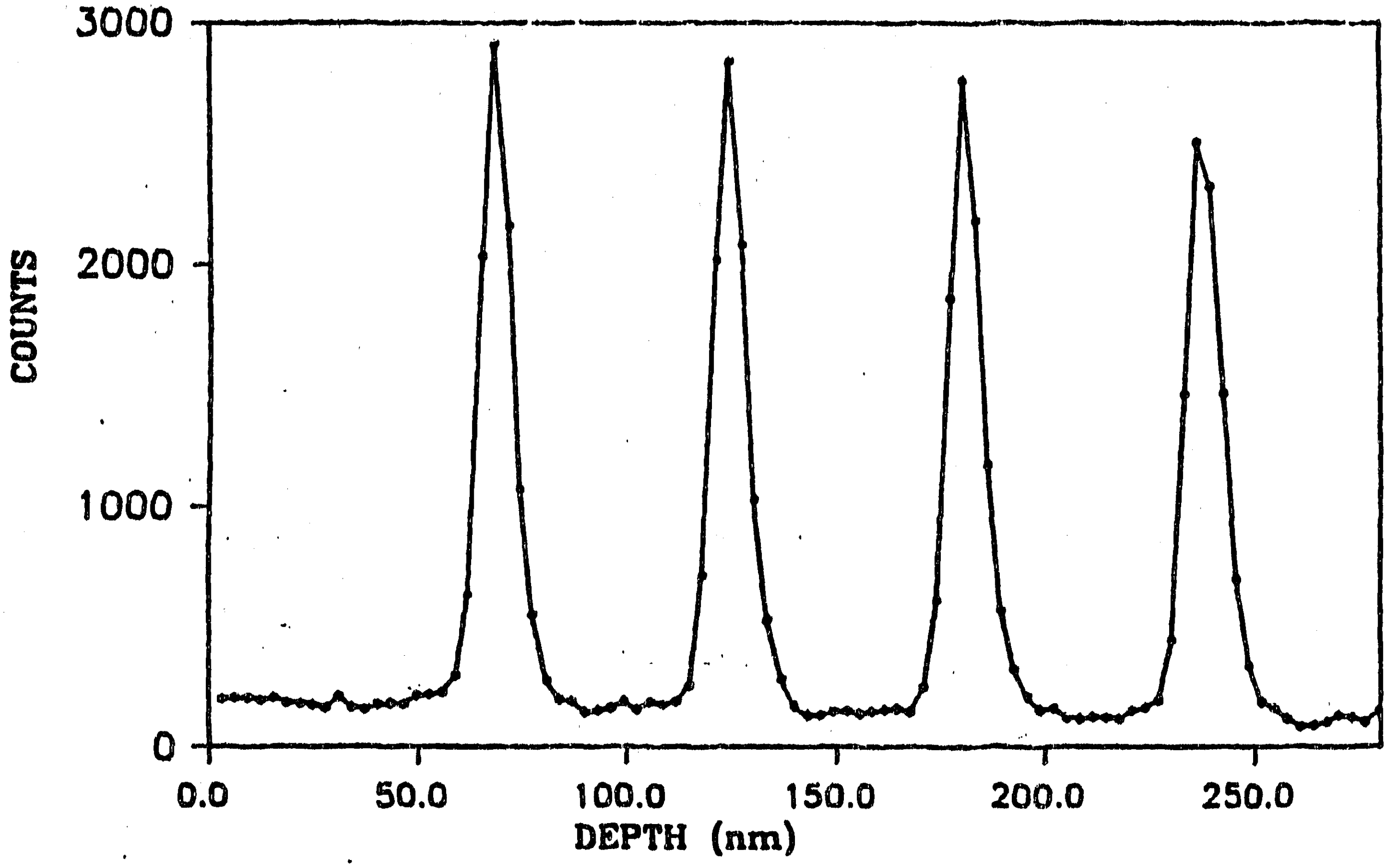

Figure 26. SIMS profile of GaAs with Si delta doped layers.

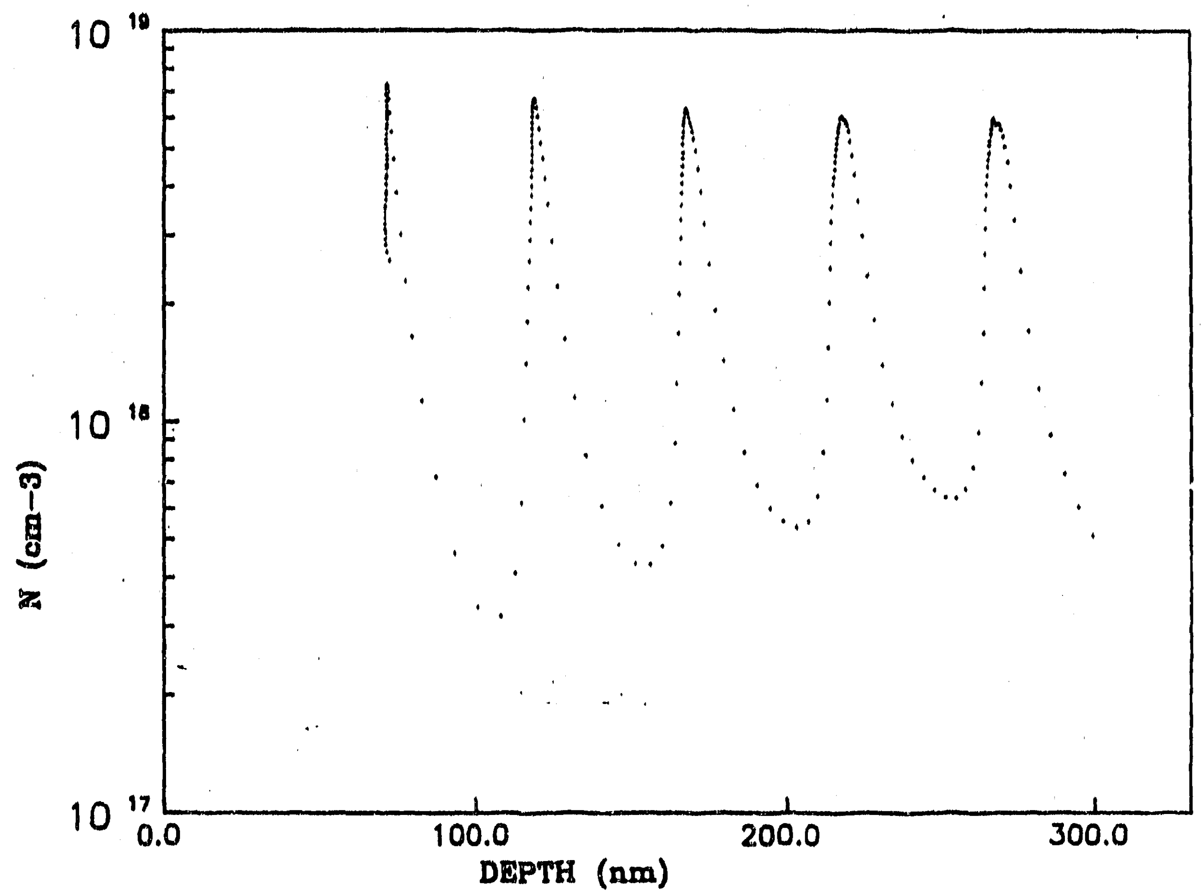

Figure 27. Electrochemical C-V profile of GaAs doped with five delta doped layers.the

width of the profile was dependent on its position within the film. The deeper layers exhibit a larger FWHM in contrast to the SIMS data, which indicated a uniform FWHM of 9 nm for all layers. Thus this variation is a manifestation of the measurement technique. A careful inspection of the crater bottom by microscope and step profiling indicated a nonuniform and rough etch front, which increased in roughness as the etch progressed. Figure 28 shows the electrochemical etch front after 0.3 μm etching. This is a typical profile of the crater created by the C-V etch as measured by Alpha step profiler. The depth of the roughness of the etch front was measured to be 45 nm, and greatly contributes to the profile broadening of the C-V profile. Therefore, the spread in the carrier concentration profile is partly attributed to the measurement technique. In an attempt to decouple this effect, the FWHM of the δ-layers is plotted in Figure 29 as function of their depth. The extrapolation of a linear fit to the data provides a means for obtaining the line width free from any instrumentation effect. This width was found to be 0.85 nm or approximately 3 atomic layers.

Table 5 presents analysis of the peak intensity of each layer, N_b and its corresponding integrated sheet density. The peak intensity for the layers diminishes as a function of depth, because of the spread of the δ-doping profile. However, the carrier sheet density remains nearly constant at $N_s = 6.6 \times 10^{12}$ Si cm^{-2}, which agrees well with the intended doping level of $N_s = 6.2 \times 10^{12}$ cm^{-2}. These values for N_s were obtained from a simple triangular integration with the FW at 95% forming the triangle base and N_b its height.

The SIMS profile of the δ-doped structure indicates that the broadening due to knock-on was much greater than the actual spread of the Si-doping. SIMS profiles of this sample obtained using a lower ion beam energy of 4 KeV gave a FWHM of 6.3 nm for the first δ-layer, again indicating that the profile width was greatly influenced by the measurement technique. This profile also showed that no segregation or diffusion of the dopant occurred either close to the surface or deeper into the film under these growth conditions. The small skewing of the profile to the left indicates that the knock on-effect, though small, was not negligible at these ion beam energies. In performing SIMS profiling, Si counts take place over an etch period corresponding to a width of 1.8 nm per point, which is considerably larger than the interatomic distance. Thus, while

Table 4. Electrochemical C-V results. d is the distance from the surface, N_b is the measured peak bulk concentration and N_{st} is the integrated carrier density.

d (nm) intended	d (nm) measured	FWHM (nm)	FW at 95% (NM)	N_b 10^{18} cm^{-3}	N_{st} 10^{12} cm^{-2}
76.5	75.0	3.14	15.6	7.21	5.65
127.5	122.1	6.02	23.9	5.50	6.58
178.5	169.7	7.45	28.2	4.84	6.82
229.5	220.4	9.19	31.4	4.52	7.09
280.5	268.8	10.78	32.9	4.31	7.08

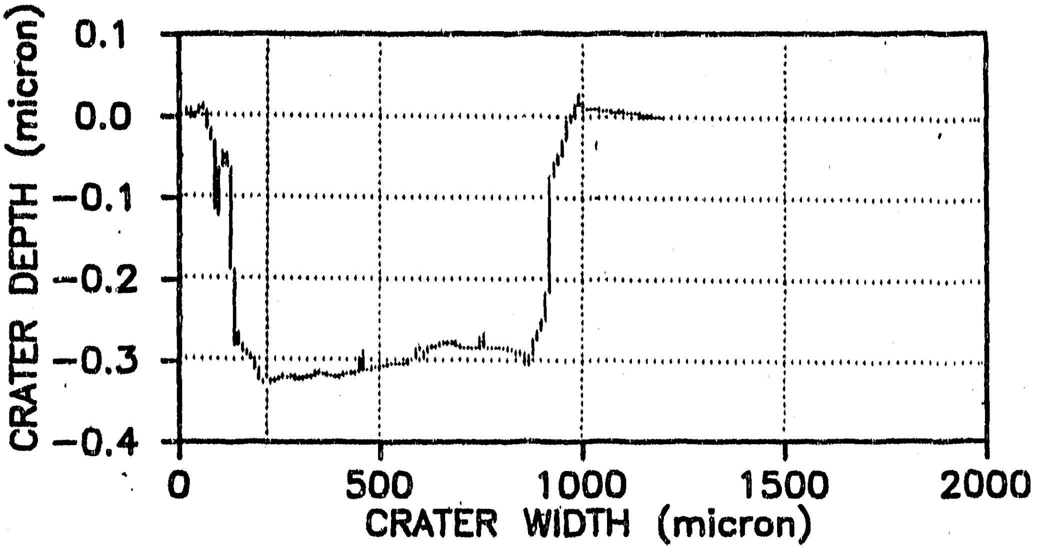

Figure 28. Roughness of the C-V etch front as measured by Alpha step profiler.

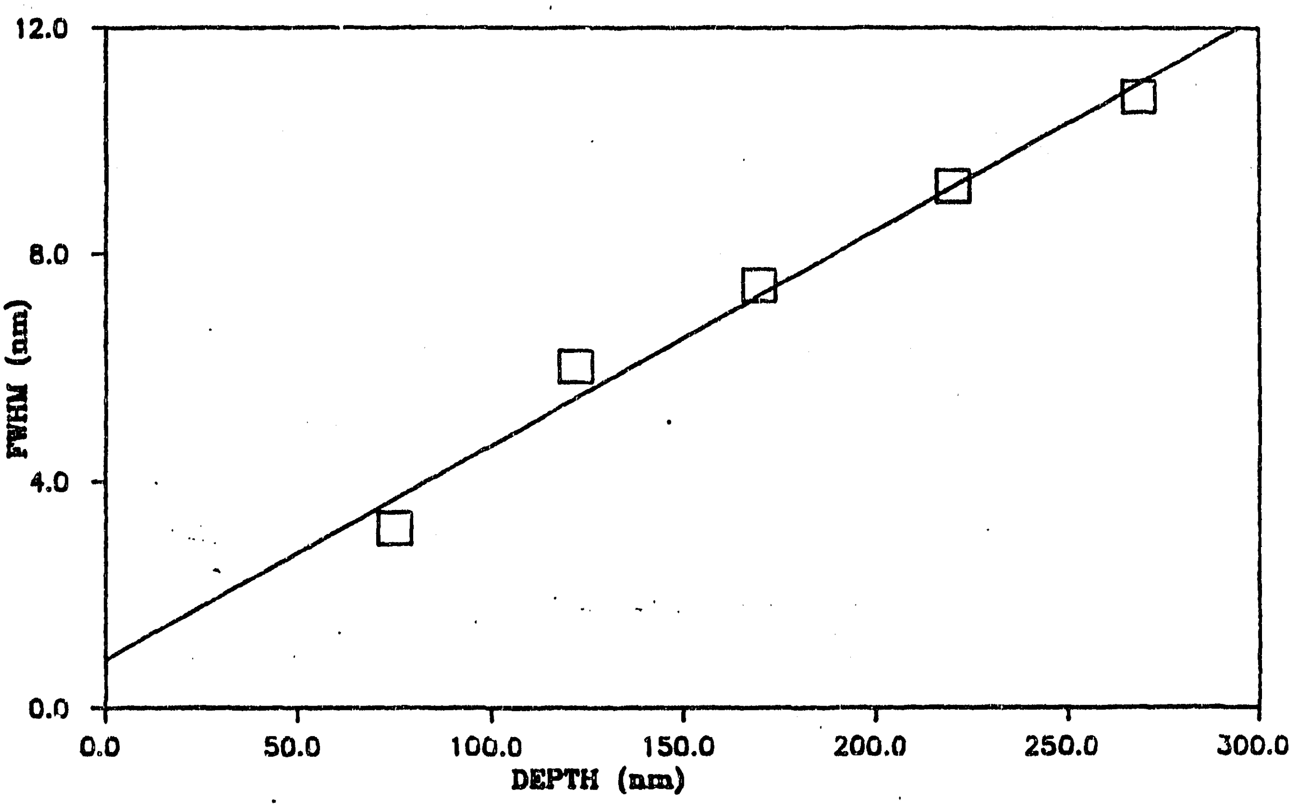

Figure 29. Full width at half maximum (FWHM) of planar doped layers as obtained from C-V profile vs. the depth of the layers.

SIMS profiling provides a means of Si profiling as a function of depth, it has neither the resolution nor the sensitivity needed for δ-doping sheet concentration and profile width measurements.

The electrochemical C-V profiling technique is intended for bulk dopant measurements at moderate 10^{16} - 5×10^{18} cm^{-3} doping levels, and is thought to be insensitive to variation in doping concentration over distances comparable to the Debye screening length[32], and thus should not be applied to δ-doped structures. However, since the profile measures both the position and concentration of the doping very accurately, the technique is obviously very useful as a means to study the multiple δ-doped layers. Further, the C-V technique has also been applied to such structures by Chin[27] and Schubert[30] with reasonable results. Our profiles are void of any unusual folding back of the profile or a change in carrier type, which are the typical problems encountered in electrochemical C-V profiles. Since the intended carrier concentration is about 10^{20} cm^{-3} the Debye length is 0.2 nm, thus enabling use of the C-V profiler as an acceptable means of characterizing the δ-doped layer. A point to note about the C-V profile is that the background concentration is high and increases as a function of depth in the same manner as the broadening of the δ-doped layers. This has been shown to be a manifestation of the technique. C-V profiling after chemically etching the surface layer significantly reduces the background concentration and sharpens the FWHM of the second and subsequent δ-doped layers(33).

Various distribution functions were used to calculate the sheet concentration as described below and are presented in Table 5. The Triangular approximation has been described earlier. If the Si distribution is represented by $N(x) = Ae^{-a|x|}$ with the center of doping at x = 0, A = N_b where a is determined from the FWHM. Integrating this function with limits at 5% of the value of N_b gives $N_{sc} = 1.9\ N_b/a$. The distribution can also be modeled as a Dirac δ-function and represented by a Gaussian in the form:

$$\delta(x) = N_b(\exp(-a_x^2))^2$$

with N_b as defined above, then one can use the measured FWHM parameter to integrate this function for each layer. The integral of above function is a definite integral:

$$\int_{-\infty}^{+\infty} \exp(-a_x^2)^2 \, dx = \sqrt{\pi/a}$$

where $N_s = N_b\sqrt{\pi/a}$. For the peak at 75.0 nm we have $\delta(3.17/2) = 1/2$ which results in a = $5.25\text{x}10^6$ cm^{-1} and N_s = $2.43\text{x}10^{12}$ cm^{-2}. This value is considerably less than the intended doping level and that evaluated by other techniques. This is the general trend for the other lines and, indicates a deviation of the doping from a Gaussian profile defined by a single FWHM parameter. The results of the calculations are also presented in Table 5.

In this study, therefore, planar doped GaAs with Si was grown by MBE and the shape of the doping profile studied. The FWHM of the δ-doped layer was measured to be 3.1 nm at room temperature. It is shown that this width and the shape of the profile are strongly broadened by the measuring technique. Extrapolation of the data indicates that the FWHM for a δ-doped layer free from instrumentation interference could be 0.85 nm or three atomic layers. The integrated doping concentration for the δ-doped layer agrees well with the intended doping levels of $6.2\text{x}10^{12}$ cm^{-2}. These results show that highly localized doping of GaAs with Si is possible and is an important step in developing the DID technique for bandgap offset control.

2.2.6 Growth Techniques for CdTe/HgCdTe VSSEF Structures

As discussed previously the range of bandgap energies and material properties required for complex solar cell designs requires the development of II-VI material systems such as the ZnCdTe and HgCdTe alloys, and the ability to grow sophisticated structures in these material system.

Table 5. Fitting parameters and the calculated carrier sheet densities. N_s=6.17X10^{12} cm^{-2} intended sheet density, N_{sg} Gaussian fit calculated sheet density, N_{se} exponential fit sheet density, and N_{st} triangular area calculated sheet density.

FWHM (nm)	a 10^6 cm^{-1}	N_{sg} 10^{12} cm^{-1}	α 10^6 cm^{-1}	N_{se} 10^{12} cm^{-2}	N_{st} 10^{12} cm^{-2}
3.13	5.25	2.43	4.41	3.31	5.65
6.02	2.77	3.52	2.30	4.54	6.58
7.45	2.24	3.84	1.86	4.94	6.82
9.19	1.81	4.42	1.51	5.69	7.09
10.78	1.54	4.94	1.29	6.37	7.08

Currently, molecular beam epitaxy is being investigated for this purpose, but the growth of high quality crystals and their reproducible doping is still a problem.[34] To overcome these limitations, a chemical beam epitaxy (CBE) system was developed under this and related programs. The advantage of this technique is that the use of hydride and/or metalorganic sources enables greater flexibility and more precise control to be achieved over the chemical reactions occurring during growth, as monomer, dimer, or tetramer species can be supplied to the growth surface depending on which is found to optimize the nucleation and growth process. To implement this study, extensive modifications have been made to a Varian GEN II MBE system as described below. These consist of the development of a turbomolecular pumping system, new types of gas sources and injectors, and a Hg-vapor source.[35,36]

<u>Pumping System</u>: Because of the relatively high loads of toxic gases used in CBE, a specially designed pumping system was implemented to handle hazardous and corrosive organometallics, hydrides and Hg vapor. Figure 30 shows a schematic representation of the pumping system, the main component of which is a Balzers MBE Series turbomolecular pump with a pumping speed of 1400 1/s for N_2 and approximately 1000 1/s for Hg. Gases exhausted from the turbomolecular pump pass into a cold trap operated at -60°C which is designed to condense the Hg vapor and minimize any contamination of the mechanical backing pump. Similarly, to minimize contamination of the turbomolecular pump due to hydrocarbon backstreaming, a micromaze oil vapor trap is included on the inlet of the backing pump.

The backing pump, an Alcatel 50 cfm Corrosion Series Pump, also uses inert gas ballasting to dilute and prevent condensation of the pumped vapors. The Alcatel pump exhausts into an Emcore toxic gas scrubber filled with a sulfur impregnated activated charcoal capable of absorbing up to 40 percent of its weight in Hg. This feature has no effect on the charcoal's ability to absorb organometallics and hydrides which can then be oxidized and disposed of in a controlled manner. As indicated in Figure 30, an array of valves enable various parts of this sytem to be isolated for removal of trapped vapors and the atmospheric pressure purging of both the pumping components and gas source lines.

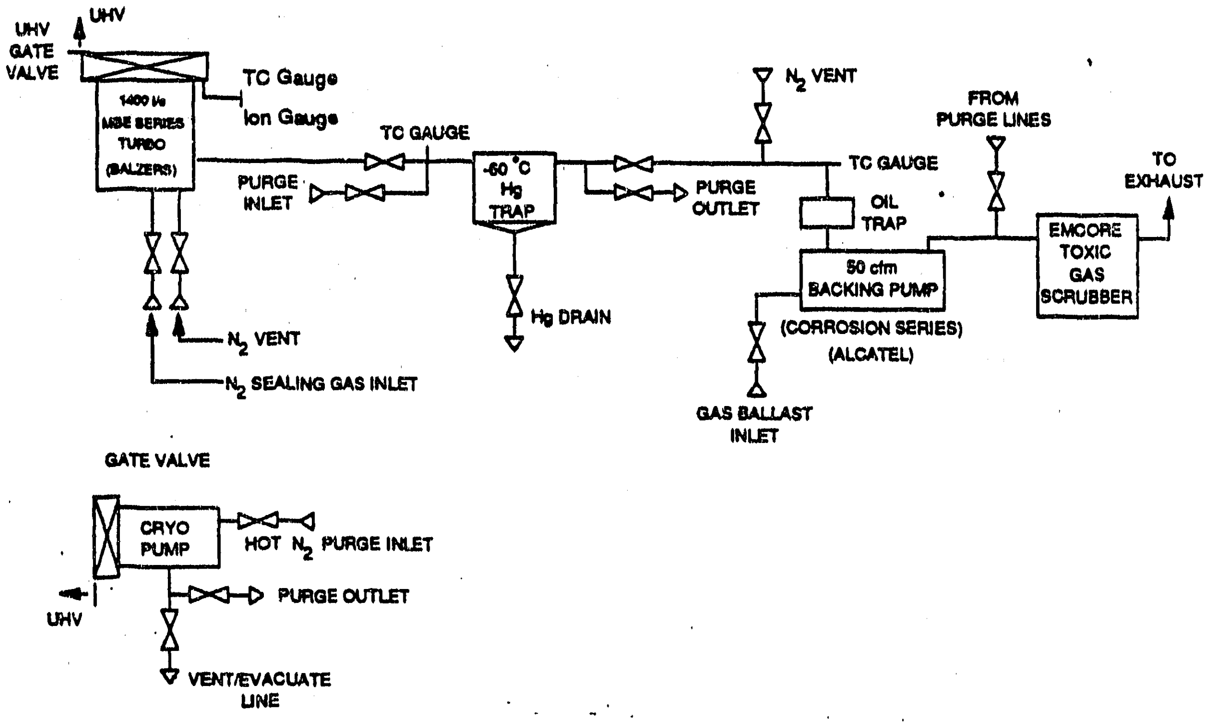

Figure 30. Schematic representation of Chemical Beam Epitaxy pumping systems.

Finally, a Varian cryopump was also attached to the system for removing Hg and organometallics from the growth ambient when needed. Provisions were made for hot gas purging of the cryopump using the gas purging system described above.

Gas Sources: The gas sources utilized in the CBE system are pressure controlled and can operate with upstream pressures on the order of a torr. Hence, the source gases can be directly injected without a carrier gas. This greatly simplifies gas source construction, minimizes the gas load on the pumping system, and makes it easier to maintain the beam fluxes in the molecular flow regime. This is especially important in the growth of Hg-based materials because of the large Hg fluxes required.

The pressure controlled vapor sources operate on the principle of choked viscous flow through an orifice and are similar in concept to a Hg source of this type, which has been designed and implemented in our laboratory.[36] The Te, Cd, and Zn sources operating on this principle use MKS Instruments 1150B flow controllers and are designed for the following source gases; diisopropyltelluride (DipTe), diethylcadmium (DeCd), and diethylzinc (DeZn). The DipTe (10 sccm f.s.), DeCd, and DeZn (5 sccm f.s.) flow controllers have repeatabilities of 0.2% and are configured to produce growth rates of up to 2 μm/hr. The precision of the flow controllers is calculated to produce a stability in the Cd to Te ratio of approximately 0.1%. For $Hg_{1-x}Cd_xTe$ alloys with $x = 0.2$, this stability corresponds to a deviation in the x value of 0.0002, a factor of 5-10 better than is currently available with conventional thermal sources.

Dopant Source: A p-type gas dopant source was also designed which operates on the same principle as the host gas sources. However, the design principles of the dopant source are even more severe as it must be able to accurately regulate flow rates that are four to eight orders of magnitude less than the host gas flow controllers. To achieve this level of control, an absolute pressure regulator was utilized, thus allowing control of the dopant gas at less than atmospheric pressure. The reduced pressure gas was then fed through a stepper motor driven leak valve which maintains the downstream pressure as measured by a high accuracy capacitance manometer. This controlled pressure exists through another leak valve (which acts as a variable orifice) and enters the CBE growth chamber. The sensitivity of the manometer and valve feedback system gives the dopant source a four order of magnitude dynamic range for a fixed orifice setting. Changing the orifice setting obviously allows the system to achieve an even greater dynamic range. Figure 31 shows a schematic of the dopant gas source. For the initial studies arsine was chosen as the dopant gas although, any of the organometallic As gases could be substituted when more fully developed. The pure arsine was contained in a small volume, low pressure bottle with a built-in flow limiting orifice, thus minimizing the safety hazards usually associated with arsine.

Injectors: To prevent gas phase reactions, separate injectors were used for the group II and group VI elements. This enabled independent optimization of the cracking conditions for each source gas. The group II injector uses a 3/4 in. o.d. high purity Ta delivery tube while the group VI injector utilizes a similarly sized pyrolitic boron nitride (PBN) delivery tube to avoid any reaction of Te with Ta. Both injectors were fitted with thermocouples to monitor the hot and cold zone temperatures and have individually designed boron nitride diffuser/nozzle elements to enhance the cracking of the metalorganic gases and to increase flux uniformity. In particular, the group VI nozzle was carefully designed to avoid the recombination of monomer Te into its dimer form, once it had been thermally dissociated from the metalorganic complex.

Results: So far preliminary system evaluations and a few test growth runs have been performed with this system. These include a study of the cracking dependence of DipTe and CdTe and HgZnTe growth using solid Cd and Zn sources. From these studies we conclude that monomer Te is produced with reasonably high efficiencies (Figure 32) and can be used to grow epitaxial CdTe and HgZnTe films (Figure 33). From these initial results we believe the CBE has the potential to solve many of the problems currently experienced by conventional growth technologies in obtaining abrupt heterointerfaces, precise stoichiometric adjustment and complex n- and p-type extrinsic doping profiles in II-VI semiconductor systems.

Substrate Temperature Calibration

In order to take full advantage of the CBE growth technique it is important to know the temperature of the substrate very accurately during the growth of compound semiconductors by chemical and molecular beam epitaxy (MBE). This is particularly

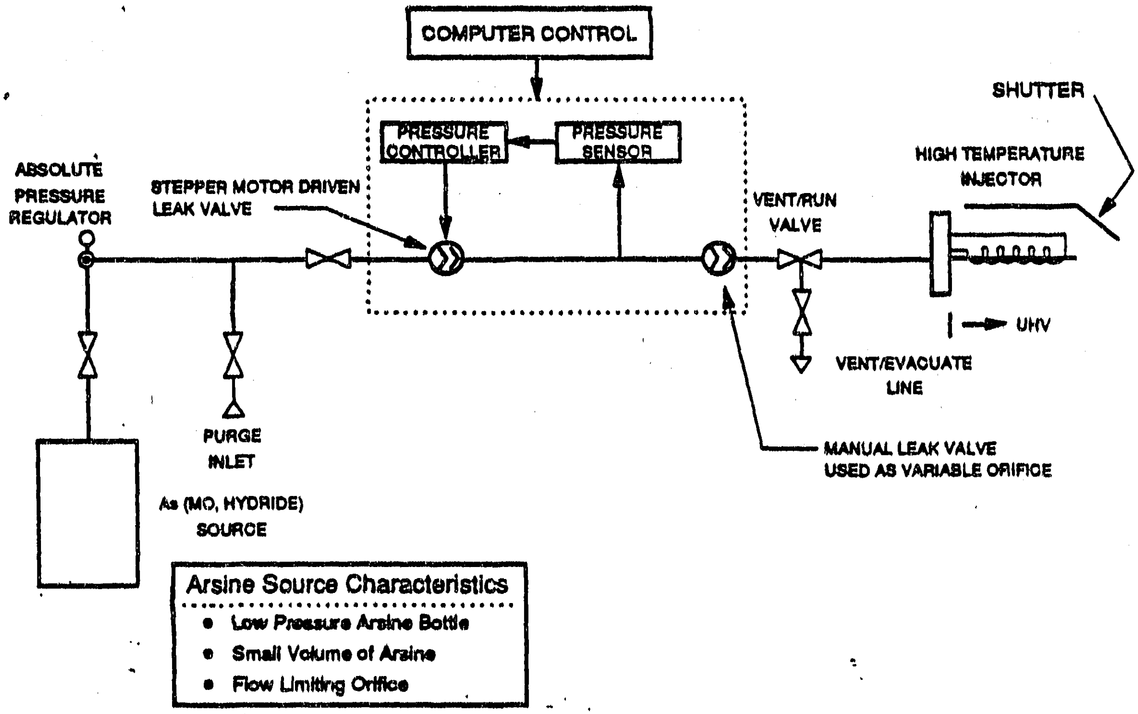

Figure 31. Schematic of arsine gas dopant source.

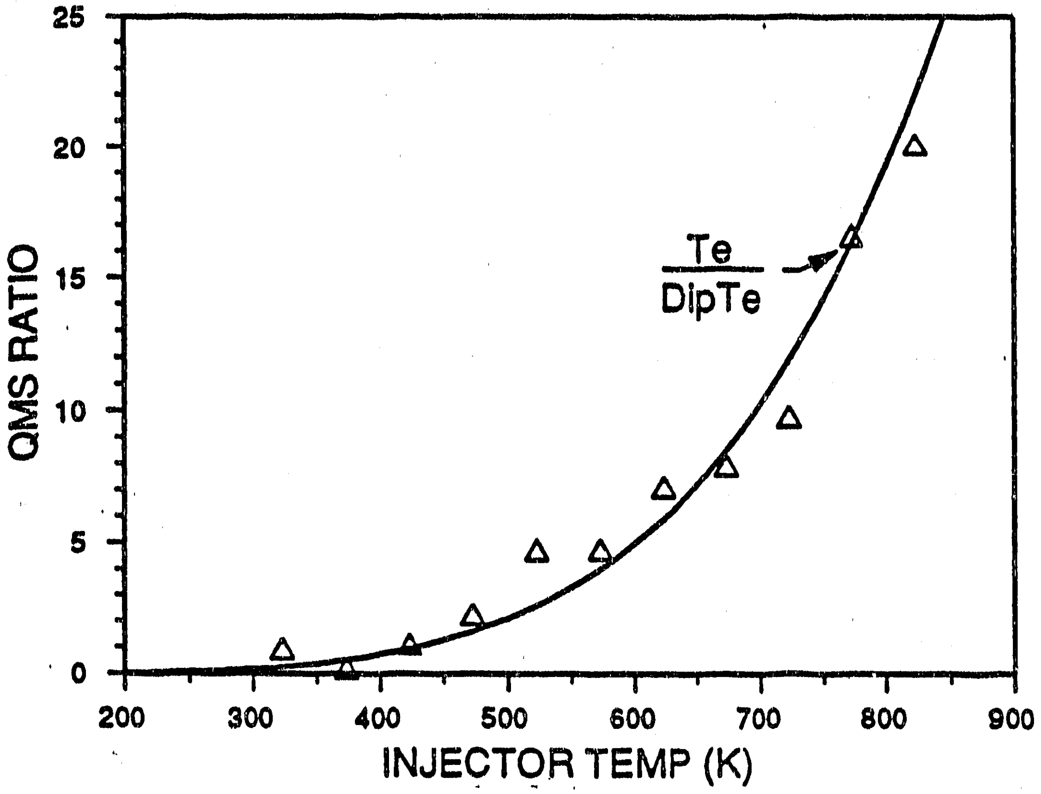

Figure 32. Ratio of QMS Te^+ current to $DipTe^+$ current as a function of injector temperature.

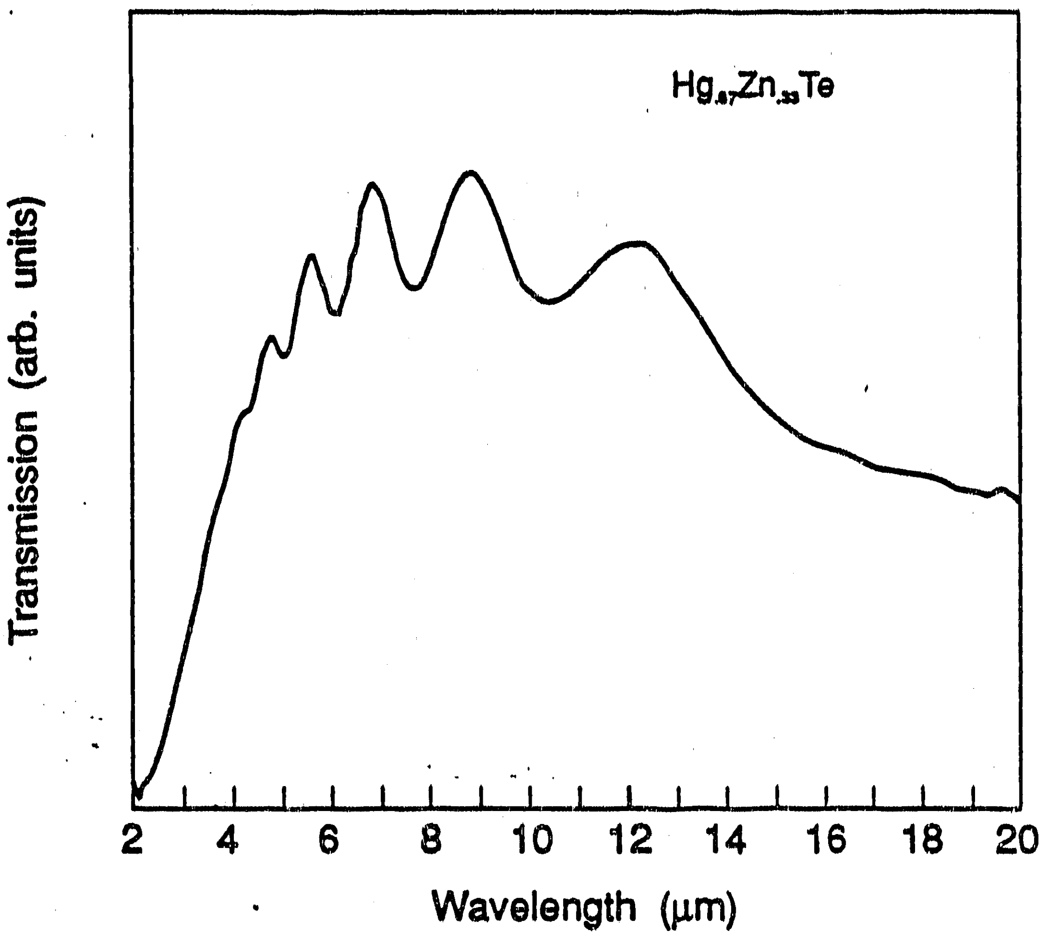

Figure 33. IR transmission spectrum of $Hg_{0.67}Zn_{0.33}Te$ layer.

true for the CBE and MBE growth and doping of CdTe and HgCdTe alloys. The growth rate and composition of $Hg_{1-x}Cd_xTe$ alloys have been shown to be very sensitive to small changes in the substrate temperature.[37] Likewise the doping of these alloys and studies of CdTe nucleation kinetics have shown a strong dependence of dopant incorporation and electrical activity on the growth surface temperature.[38,39] Thus clearly, the temperature of the substrate must be precisely measured and controlled during the growth of these materials. This is difficult, both because of the low temperature range used for the growth and doping of HgCdTe and CdTe and because a temperature reading based on the thermocouple being in contact with the substrate holder is not accurate enough to ensure reproducibility; particularly when several substrate holders are utilized. Temperature calibration by means of the melting point of elements is difficult because the exact melting point is difficult to observe, also the technique is not very practical during growth.

In this paper we report a new convenient in-situ technique to accurately measure the actual temperature of the growth surface of the substrate. The technique has the advantage that it is very sensitive over the temperature range used for the growth of CdTe and HgCdTe and also directly measures the growth surface temperature. This unique capability cannot be duplicated by any other technique and is a consequence of a pronounced change that is observed in the reflection high-energy electron diffraction (RHEED) pattern of the epilayer when a source element sublimated from an effusion-cell condenses on the substrate. In these experiments the onset of the condensation of Te_2 on CdTe surfaces was used both to determine the temperature of the epilayer and to calibrate molybdenum substrate holders.

Experimental Procedure

Experiments were performed in a Varian GEN II MBE system equippped with RHEED and dedicated to grow II-VI materials growth. The onset of the condensation of tellurium on a (001) CdTe epilayer was detected by observing the transition of the normally streaked RHEED pattern exhibited during the growth of CdTe (Fig. 34a) to a spotty pattern due to Te precipitates (Fig. 34b-34d). Condensation of tellurium is expected to occur when the pressure of the incident Te_2 flux exceeds the equilibrium vapor pressure of Te_2 over CdTe. The tellurium condensation technique was used to measure the correction to be applied to the thermocouple reading and to determine the absolute temperature on the surface of the substrate. Three Mo blocks were calibrated for temperature corrections by this in-situ technique. Doped (001) GaAs substrates were used to grow (001) and (111) CdTe films. The GaAs substrates were degreased, etched in a solution of H_2So_4, H_2O and H_2O_2 (5:1:1) and mounted at the center of a Mo substrate holder. Small pieces of indium and bismuth metals in the shape of a cone, were soldered onto two different pieces of GaAs. These samples were mounted on the same Mo substrate holder. The substrate was heated slowly in the growth chamber of the MBE system to 130°C, as read by the thermocouple in contact with the back side of the Mo substrate holder. The temperature was maintained at 130°C for about 15 minutes to allow the substrate and the Mo holder to attain thermal equilibrium. Subsequently, the substrate was further heated in steps of about 3°C every 5 minutes. The magnified shadow of the indium sample cast by the RHEED electron beam was observed on the phosphor screen. Drooping due to gravity and a change in the shape of the indium sample was taken as an indication that the temperature of the substrate was 157°C, the melting point of indium. In a similar manner, the temperature of the substrate was measured with the thermocouple at the melting point of bismuth (271°C). The difference between the actual melting point and the corresponding temperature of the substrate as measured by the thermocouple was calculated for each of the two metals. As the change in shape of the specimens upon melting is not very obvious and hence difficult to determine accurately, the error in these measurements is estimated to be ±5°C.

The thermocouple reading when the substrate was heated to almost completely desorb the oxide on GaAs in order to initiate (001) CdTe growth was also compared with the found in the literature[4]. For this part of the experiment, the substrates were first heated slowly up to 550°C (as indicated by the thermocouple) and allowed to stabilize at that temperature. Beyond 550°C, the substrate was heated in steps of approximately 5°C every 3 minutes until the RHEED pattern indicated that enough oxide on the GaAs substrate had desorbed in order to grow (001) CdTe. The substrate was then cooled to 300°C under a CdTe flux to grow a (001) CdTe layer. It was found

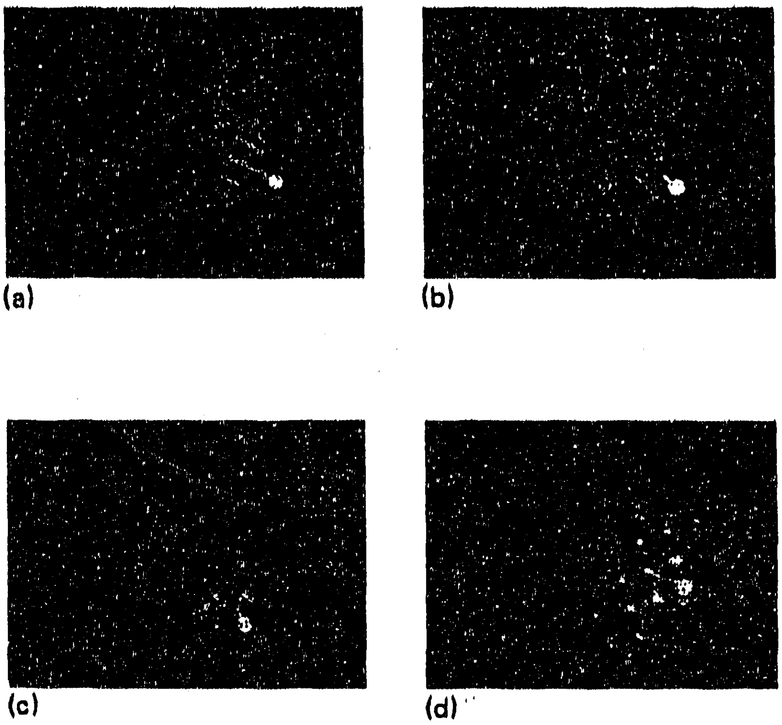
(a) (b) (c) (d)

Figure 34.

a. RHEED pattern of a Te-stabilized 2x1 surface reconstruction on the (001) surface observed along the [110] azimuth.

b. The first indication of the condensation of the incident Te_2 flux (BEP = 2.2×10^{-7} torr) is the appearance of a bright spot superimposed on the central streak. For substrate holder AA, the thermocouple temperature was 192°C.

c. RHEED pattern observed 5 s after the pattern shown in 1b. Diffraction spots due to tellurium precipitates can be seen superimposed on the streaks due the bulk and exhibit a square lattice. Spots can also be seen superimposed on the reconstruction derived streaks.

d. RHEED pattern observed 2 min after the onset of condensation, with a Te_2 flux incident on the substrate continuously. The thermocouple temperature was 192°C.

that the exact temperature at which the oxide desorbed from the GaAs substrate was dependent on the rate at which the substrate was heated. When the substrate was heated quickly, there was insufficient time for the substrate and the rest of the Mo holder to approach equilibrium. Hence, the accuracy of the temperature calibration by this method is about ±5°C. In this manner, the offset between the thermocouple measurements and the absolute temperature was established at 157, 271 and 582°C which correspond to the melting points of indium and bismuth and the desorption temperature of the oxide on GaAs

To study tellurium condensation on CdTe surfaces, a 1 μm thick CdTe layer was grown at 300°C using a binary CdTe source. A separate effusion-cell containing elemental Te was used to deposit tellurium to observe condensation. The approximate temperature at which a certain flux of Te_2, from the tellurium effusion-cell, condensed on the CdTe surface was first determined. This rough measurement was then used as a starting point to precisely determine the condensation temperature for the same Te_2 flux. The approximate condensation temperature was measured by the following procedure. CdTe growth was terminated by closing the shutter of the CdTe effusion-cell and the substrate heater turned off. The shutter of the tellurium effusion-cell was then opened so that a Te_2 flux was incident on the substrate as it cooled rapidly. The RHEED pattern and the thermocouple reading were monitored as the substrate cooled. Prior to condensation the pattern was streaked and exhibited a Te-stabilized two fold reconstruction along the (110) azimuth[41] (Fig. 34a). At the onset of the condensation of tellurium on the CdTe surface, a single bright spot was observed to be superimposed on the central streak (Fig. 34b). As condensation proceeded, more spots appeared superimposed on the bulk streaks, some closer to the shadow edge. The pattern became spottier as condensation proceeded further (Fig. 34c and 34d). For short durations of condensation, it was observed that the streaks due to the bulk and the reconstructed surface were not destroyed. The beam equivalent pressure (BEP) of the incident Te_2 flux was then measured by a nude ion-gauge that could be rotated to the position of the substrate.

In order to reuse the CdTe layer, the substrate temperature was heated to 300°C and maintained at that temperature for three to five minutes to desorb the tellurium that had condensed on the substrate. When the original streaked RHEED pattern was restored, CdTe growth was once again started and 0.1 μm of CdTe was grown to regain the initial crystalline quality of the film. In determining the condensation temperature by the above method, exact equilibrium between the film and the Mo holder was precluded. In order to determine the condensation temperature precisely, the substrate was cooled from the growth temperaturre (300°C) and stabilized at a temperature 25°C above the approximate condensation temperature determined previously. The shutter of the Te effusion-cell was then opened and the substrate was slowly cooled in steps of about 3°C every 3 min until the onset of condensation was detected. In this manner, by cooling the substrate slowly, the substrate and the Mo holder approach equilibrium. Immediately after the determination of the Te_2 condensation temperature, the pressure of the incident Te_2 flux was measured once again with the nude ion-gauge.

Results and Discussion

The reaction between excess tellurium condensed on a CdTe surface and the incident Te_2 dimer flux is expressed as

$$Te_2\ (g) \rightarrow 2Te\ (s) \tag{1}$$

The direction of this reaction is determined by the surface lifetime (τ_s) of a Te atom on the surface of the layer and the magnitude of the incident flux. The lifetime τ_s of a Te atom on the surface of CdTe is related to the absolute temperature T_s of the substrate by the following Arrhenius relationship

$$1/\tau_s = A\ \exp(-E_a/kT_s), \tag{2}$$

where A is a constant, E_a is the activation energy for the desorption of Te_2 and k is the Boltzmann constant. If τ_s is less than the average time of arrival of the incident Te_2 molecules (t_{av}) on the substrate, there is no net accumulation of Te on the surface. However, when τ_s is just greater than t_{av}, condensation commences and Te precipitates start forming on the substrate. Thus, at a temperature T_s when $\tau_s = t_{av}$, the equilibrium vapor pressure of Te_2 over the excess Te on the substrate balances the flux of the incident molecules. The temperature at which this occurs depends directly on the incident Te_2 flux and is determined in this experiment from measurement of the Te_2 flux.

The vapor pressures of gallium and arsenic over GaAs has been experimentally measured by previous workers[41,42]. It has also been reported that the activation energy for the desorption of excess Ga on GaAs is similar to the activation energy for the sublimation of Ga from metallic Ga[43]. Previous work done at Georgia Tech indicates that the activation energy for the desorption of tellurium from (001) CdTe is very close to the enthalpy of sublimation for diatomic Te from solid tellurium[44]. This indicates that the vapor pressure for excess tellurium over a CdTe surface is equal to the vapor pressure of solid tellurium. The equilibrium vapor pressure P, of Te_2 over solid Te can be calculated at an absolute surface temperature, T_s, using the relationship[9]

$$\log P(\text{torr}) = -9175/T_s - 2.71\log T_s + 19.68 \qquad (3)$$

The thermocouple temperature (T_{meas}) which is measured at the onset of condensation, is plotted versus the theoretical euqilibrium condensation temperature (T_s) of Te_2 determined in this manner in Fig. 35. The melting point of indium provides an absolute temperature datum and is in good agreement with the tellurium condensation data. The T_{meas} versus T_s plot is not linear, and deviates from the equilibrium theory at temperatures above 190°C. The reason for the departure of the Te_2 condensation temperature from the equilibrium theory at higher temperatures is not completely understood. The assumption that the vapor pressure of Te_2 over a CdTe epilayer is equal to the equilibrium vapor pressure of Te_2 over solid Te requires further investigation. The evaporation of the excess tellurium on a CdTe surface, in the growth chamber of an MBE system, approaches Langmuir (free) evaporation. Thus, in order to establish a certain pressure of Te_2, the substrate has to be heated higher than that predicted by using Eqn. 3. Also, the undercooling required to nucleate the precipitate has been neglected in this analysis. However, the inclusion of undercooling would further increase the deviation of the data from the equilibrium theory. We define T_{actual}

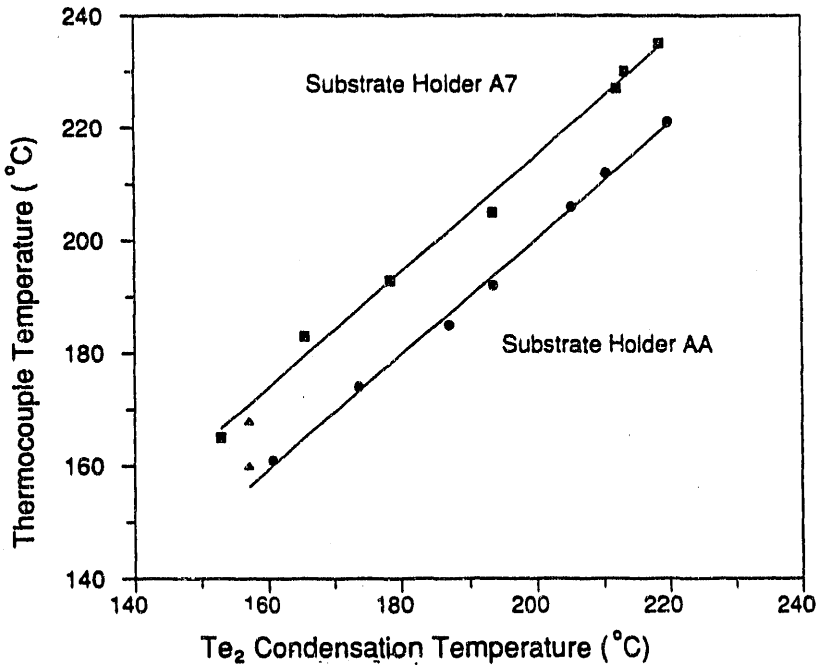

Figure 35. The thermocouple temperature plotted vs. the Te_2 condensation temperature (calculated from the equilibrium theory using Eqn. 3). The dashed lines represent quadratic fits to the experimental data. The solid lines follow from the equilibrium theory and have a slope equal to one. The In melting point data are represented by the symbol.

as the substrate temperature as determined by the melting points of indium and bismuth and the desorption temperature of the oxide on GaAs. Figure 36 shows a plot of T_{meas} versus T_{actual} for three different Mo holders. The condensation temperature for Te_2 pertaining to a beam equivalent pressure of 2.2×10^{-7} torr is also shown in the same plot. Note that excellent agreement was found between all of the different temperature measuring techniques. Additionally, the condensation temperature for the Te_2 flux of beam equivalent pressure of 2.2×10^{-7} is in excellent agreement for all holders measured. For substrate holder A8, T_s was found to be lower than T_{meas} by about 73°C as indicated by the condensation temperature of Te_2. This large a discrepancy could be due to the different emissivity and thermal conductivity of that particular substrate holder. Similar data were also observed for substrate holder A7 for which T_s was measurred to be lower than T_{meas} by an average of 14°C, and for substrate holder AA for which T_s was measured to be an average of less than 1°C lower than T_{meas}. It is also possible for T_s to be greater than T_{meas}, if the thermocouple is not in proper contact with the Mo substrate holder. However, this situation was not encountered in this experiment.

The data in Figs. 35 and 36 were measurements made for (001) CdTe. Similar studies to determine the condensation temperature for Te_2 on (111) CdTe were found to be within 3°C of the corresponding temperature for (001) CdTe. Thus, the technique is shown to be applicable to both orientations of CdTe. For condensation temperatures below 150°C, corresponding to a beam equivalent pressure of 1×10^{-8} torr, the onset of condensation is difficult to observe and therefore the measurement is prone to error. Thus the lower limit of applicability of this technique is estimated to be around 150°C for the substrate cooling rate used in this experiment. Cooling the substrate at a slower rate can extend the lower limit of applicability of this technique and is currently being studied. As the condensation of tellurium and its subsequent evaporation by heating can degrade the crystalline quality of the epilayer, occasional calibration of a substrate holder with a test substrate piece is adequate. Damage to the epilayer can be minimized if the incident flux is terminated as soon as the first signs of condensation of Te_2 is noticed.

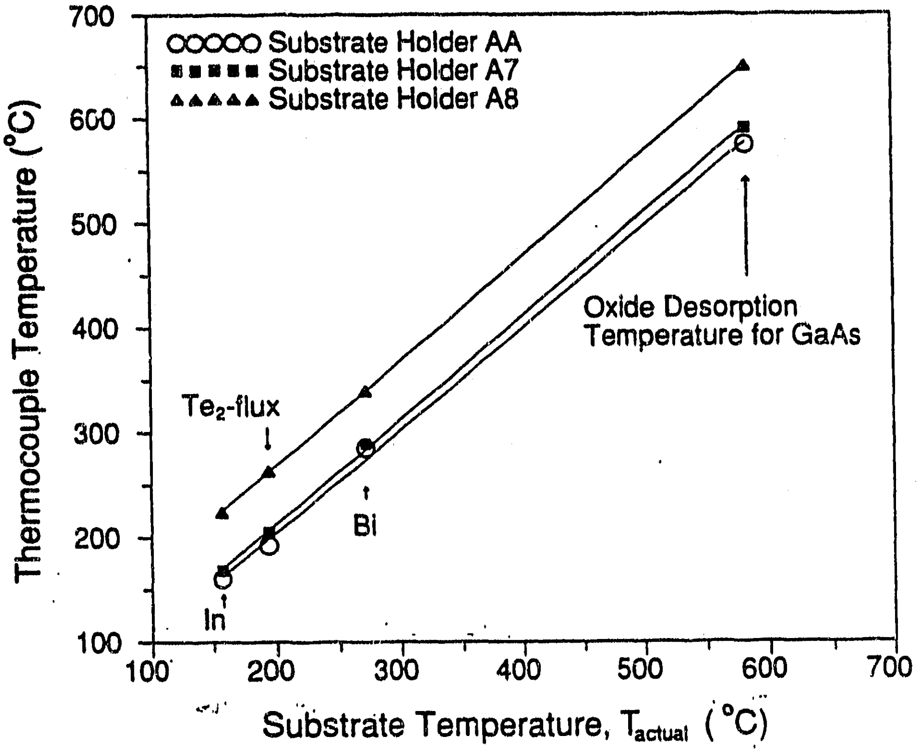

Figure 36. The thermocouple temperature plotted vs. the actual substrate temperature determined by the melting point of In and Bi and the desorption temperature of the oxide on GaAs. Also shown are the Te_2 (flux of BEP = 2.2×10^{-7} torr) condensation data.

Figures 34a-34d illustrate the sequence of the condensation of Te_2 on (001) CdTe. At the onset of condensation, the surface of the epilayer developed asperities and the RHEED electron beam was transmitted through the tellurium precipitates and displayed diffraction spots. Figure 34b shows the appearance of a bright spot on the central streak, which is the first sign of the onset of condensation (all the substrate temperature measurements were made at this initial stage of commencement condensation of Te_2 on CdTe). This spot could be seen for all azimuthal orientations of the substrate. This indicates that first atomic layers of the condensate nucleate parallel to the CdTe epilayer. The existence of a specific crystallographic relationship between the condensate and the (001) CdTe epilayer is more obvious as condensation proceeds further. Figure 34c shows the RHEED spot pattern that exhibits a square lattice indicative of the existence of four-fold periodicity. Some spots also appear on the reconstruction derived streaks, indicating twinning. Patterns similar to that shown in Figure 34c can be seen at four different azimuthal orientations, two of which correspond to the orientations exhibiting a Te-stabilized 2 x 1 surface reconstruction pattern of (001) CdTe.

Conclusion

It has been demonstrated that the condensation of Te_2, on either (001) or (111) CdTe surfaces, as detected by a change in the RHEED pattern, provides an accurate (<5°C) and convenient method of establishing the actual surface temperature on the substrate. This tecnique has been demonstrated to be applicable for substrate temperatures between 160 and 190°C and can provide an absolute sensitivity of 3°C for the cooling rates used in these experiments. It should be noted that because the surface temperature is directly measured, the technique is inherently superior to current methods. It was found that the deviation of the actual growth surface temperature from the thermocouple temperature can be as large as 70°C indicating that substrate holders have to be carefully calibrated to ensure reproducibility. This technique is particularly useful when the thermocouple is not in direct contact with the substrate holder. Finally we note that further advantages of this technique are envisioned for other materials and growth techniques such as CBE. CBE offers a more stable, quicker and better setting accuracy of the Te flux from run to run. Substrate temperature calibration in a CBE system utilizing a tellurium gas source can also be accomplished by ramping the incident flux instead of lowering the substrate temperature.

3. CONCLUSIONS

The objective of this contract was to investigate the use of new heterostructure and superlattice structures to increase solar cell performance. Specifically, to investigate novel heterojunction or superlattice, single junction solar cells, in which the energy gap of the p-side of the junction is more than twice the bandgap of the n-side. In these devices, photon-generated electrons on the p^+-side are injected by the internal electric field over the interface into the low bandgap layer. Because they experience the full difference in energy gaps, impact ionization occurs and a photo-current gain of two should be realized. Thus, the energy of the electrons in the wide bandgap region will be conserved by adding it to the current generated by the low bandgap side of the junction. The efficiency of the injection process is determined by the abruptness of the heterojunction which must be shorter than the phonon scattering mean free path ~100Å. To relieve this constraint, it was also proposed to develop variably spaced superlattice energy filter devices for the junction region, which afford high-energy injection by providing a tunneling channel in a biased superlattice.

To determine the utility of this approach, we therefore addressed the following issues: 1) the formation of a realistic theory to predict the enhancement possible with an Avalanche Photodiode (APD) Solar Cell, 2) the development of MBE growth techniques to achieve atomically abrupt interfaces in the AlGaAs/GaAs system, 3) an investigation of dipole-interface-doping (DID) techniques to achieve larger conduction band-offsets, 4) an investigation into variably spaced superlattice structures, and finally, 5) the development of an MBE system for II-VI alloy growth in order to grow structures with very large conduction band-offsets as required for these structures.

To predict the performance and characteristics of an ideal avalanche heterostructure photodiode solar cell, the method used by Henry was developed to calculate the solar cell efficiency as a function of bandgap energy and sun concentration. In this model the smaller (n-side) bandgap energy, E_{G1}, of the cell was assumed to control the I-V characteristics, while the bandgap ratio, g, between it, and the wider p-side bandgap energy, E_{G2}; and the electron impact ionization rate, $(1<\gamma<2)$, were assumed to be the principal parameters controlling the increased collection efficiency of the cell.

Assuming an ideal bandgap ratio of 2 and an impact ionization rate of 2, this calculation shows an optimum efficiency of 35.3% for a bandgap energy of 1.15 eV under unity sun concentration, and an optimum efficiency of 45.4% at a bandgap energy of 0.95 eV for 1000 suns concentration. Thus, this cell design approaches within 5% of the ideal efficiencies predicted for a conventional heterojunction solar cell, 38 and 50%, respectively. However, because its performance depends on a very efficient ionization process, very precise structures must be grown for this concept to effectively compete with the other structures.

In the material studies performed to address these issues, insitu electron beam evaluation techniques were developed to obtain precise and high quality AlGaAs/GaAs heterostructure interfaces. Delta doping techniques were also developed for the Si-doping of GaAs to achieve high electron concentrations $\sim 1\mathrm{x}10^{20}\mathrm{cm}^{-3}$ (or $3\mathrm{x}10^{13}\mathrm{cm}^{-2}$) in a 8Å thick layer. Our experiments indicate that atomic layer doping profiles are possible as we have shown that the width of the delta doped layer is narrower than the resolution of our characterization instruments such as SIMS and electrochemical C-V profiler. X-ray DCRC results indicate that the crystalline quality of GaAs was not compromised by delta doping even at high concentrations.

Investigations of new variably spaced superlattice structures were also successfully made during this program. For the first time, resonant tunneling through 2- and 3-quantum well AlGaAs/GaAs structures were observed using not only n=1, but also the higher n=2 quantum states, in the first, second, or the third quantum well. These devices exhibited excellent room temperature and low temperature resonant tunneling effects. This will allow more flexible electron injections schemes to be developed. We also developed special measuring circuitry that was required to unambiguously analyze these devices under constant current or constant voltage conditions to determine whether the resonant tunneling structures are, in fact, intrinsically bistable.

Finally, in conjunction with other programs, a chemical beam epitaxy system was constructed and alloys were grown with near state-of-the-art properties. To perform the CBE growths a Varian GEN II system was fitted with specially designed direct-injection gas sources for Hg, Cd, and Te and also a toxic gas handling system. This system was designed to meet the handling needs of Hg and metal-organic materials and includes a 1400 l/s Balzers turbomolecular pump, a -60°C Hg-vapor trap, and an Emcore toxic gas handling unit which is exhausted into a chemical flue. The Te and Cd direct injection lines are connected to a Varian low temperature injector system to precrack the MO-source material before it is incident on the substrate. Thus the chemistry of the source gas can also be separated from the surface nucleation kinetics.

Finally a unique technique was invented to calibrate the temperature of the substrate during CdTe growth. This method exploits the fact that the condensation of an incident Te_2 flux occurs on CdTe when the pressure of the incident Te_2 dimers exceeds the calculated equilibrium vapor pressure of Te_2 at the substrate temperature. In these investigations the onset of condensation was determined by a change in the reflection high-energy electron diffraction pattern of the substrate from streaked features to an array of spots. The Te_2 condensation temperature was obtained from a beam equivalent pressure measured for Te_2 and the equilibrium vapor pressure versus temperature data are in good agreement between 150-200°C, and demonstrate that the thermocouple reading can be off by as much as 70°C. The technique is currently being applied to (001) ZnTe and CdZnTe.

4. REFERENCES

1. S. M. Sze, "Physics of Semiconductor Devices," John Wiley and Sons, New York, (1969).
2. H. J. Hovel, Solar Cells, in R. K. Willardson and A. C. Beer, Eds., Semiconductors and Semimetals, Vol. 11, Academic, New York, 1975.
3. C. H. Henry, Limiting Efficiences of Ideal Single and Multiple Energy Gap Terrestrial Solar Cells, J. Appl. Phys. 51, 4494-4500 (1980).
4. T. P. Pearsall, Zap! Introducing the Zero-Bias Avalanche Photodiode Electronics Letters 18, 512-514 (1982).
5. D. A. Evans and P. T. Landsberg, Recombination statistics for Âuger effects with applications to p-n junctions; Solid-State Electronics, 6, 169-181 (1963).
6. D. Olego, J. Faurie, and P. Raccah, Optical Investigation of Hole and Electron Subbands in HgTe-CdTe Supperlattices, Phys. Rev. Lett. 55, 328 (1985).
7. Y. Guldnev, G. Bastavd, J. P. Vieren, M. Voos, J. P. Baurie and A. Million, Matnetic-Optical Investigations in a Novel Super-lattice, HgTe-CdTe Phys. Rev. Lett. 51, 907-910 (1983).
8. S. P. Kowalczyk, J. T. Cheung, E. A. Kraut and R. W. Grant, CdTe-HgTe(TTT) Heterojunction Valence-band Discontinuity: a Common Anion Rule Contradiction, Phys. Rev. Let. 56, 1605-1608 (1986).
9. F. Capasso, K. Mohammed and A. Y. Cho, Tunable Barrier Heights and Band Discontinuities Via Doping Interface Dipoles. An Interface Engineering Technique and Its Device Applications, J. Vac. Sci. Technol. B 3, 1245-1251 (1985).
10. C. J. Summers and K. F. Brennan, Variably Spaced Superlattice Energy Filter, a New Device Design Concept for High-energy Injection, Appl. Phys. Lett. 48, 806 (1986).
11. K. F. Brennan and C. J. Summers, Theory of Resonant Tunneling in a VSSEF Multiquantum Well Structure: an Airy Function Approach. J. Appl. Phys. (to be published).
12. R. Tsu and L. Esaki, Appl. Phys. Lett. 22, 562 (1973).

13. C. J. Summers, K. F. Brennan, A. Torabi, and H. M. Harris, Appl. Phys. Lett. 52, 132 (1988).

14. S. Adachi, J. Appl. Phys. 58, R1 (1985).

15. M. P. Chamberlain, m. Babiker, Semicond. SC: Technol. 4, 691-695 (1989).

16. K. K. Choi, B. F. Levine, C. G. Bethea, J. Walker, and R. J. Malik, Appl. Phys. Lett. 50, 1814 (1987).

17. M. Tsuchiya, T. Matsusve, and H. Sakaki, Phys. Rev. Lett. 59, 2356 (1987).

18. M. K. Jackson, M. B. Johnson, P. H. Chow, T. C. McGill, and C. W. Nieh, Appl. Phys. Lett. 54, 522 (1989).

19. C. E. C. Wood, G. M. Metze, J. D. Berry, and L. F. Eastman, J. Appl. Phys. 51, 383 (1980).

20. K. Ploog, J. Cryst. Growth 81, 304 (1987).

21. K. Ploog, II. Fronius, and A. Fischer, Appl. Phys. Lett. 50 (18), 1237 (1987).

22. G. Gillman, B. Vinter, E. Barbier, and A. Tardella, Appl. Phys. Lett. 52(12), 972(1988).

23. E. F. Schubert, A. Fischer, and K. Ploog, IEEE Trans. Electron Devices ED-33, 625 (1986).

24. A. Zrenner, II. Reisinger, F. Koch, and K. Ploog, in: Proc. 17th Intern. Conf. on Physics of Semiconductors, San Francisco, CA, 1984, Eds. J. D. Chadi and W. A. Harrison (Springer, Berlin, 1985), p. 325.

25. M. Shaygen, V. J. Goldman, C. Jiang, T. Sajoto, and M. Santos, Appl. Phys. Lett., 52(13), 1086(1988).

26. J. H. English, A. C. Gossard, H. L. Stormer, and K. W. Baldwin, Appl. Phys. Lett., 50(25), 1826(1987).

27. T. H. Chiu, J. E. Cunningham, B. Tell, and E. F. Schubert, J. Appl. Phys. 64(3), 1578(1988).

28. T. Makimoto, N. Kobayashi, and Y. Horikoshi, J. Appl. Phys. 63(10), 5023(1988).

29. II. Ohno, E. Ikeda, and II. IIasegawa, Jpn. J. Appl. Phys. 23, L369(1984).

30. E. F. Schubert, J. B. Stark, B. Ullrich, and J. E. Cunningham, Appl. Phys. Lett. 52(18), 1508(1988).

31. T. Ambridge, J. Stevenson, and R. Redstall, J. Electrochem. Soc. 127, 222(1980).

32. S. M. Sze "Physics of Semiconductor Devices," 2nd Edition (John Wiley & Sons, New York, 1981), p. 81.

33. J. Hillson, Private communication.

34. Summers, C. J., Benz II, R. G., Wagner, B. K., Benson, J. D. and Rajavel, D., SPIE 1106, 1989, p. 2.

35. Benz II, R. G., Wagner, B. K., and Summers, C. J., to be published in J. Vac. Sci. & Technol.

36. Wagner, B. K., Benz II, R. G., and Summers, C. J., J. Vac. Sci. & Technol. A7, 1988, p. 295.

37. S. Sivananthan, M. D. Lange, G. Monfroy and J. P. Faurie, J. Vac. Sci. Technol. B 6, 788 (1988).

38. J. D. Benson and C. J. Summers, J. Crystal Growth 86, 354 (1988).

39. J. D. Benson, D. Rajavel, B. K. Wagner, R. Benz II and C. J. Summers, J. Crystal Growth 95, 543 (1989).

40. A. J. SpringThorpe, S. J. Ingrey, B. Emmerstorfer, P. Mandeville and W. T. Moore, Appl. Phys. Lett 50, 77 (1987).

41. J. R. Arthur, J. Phys. Chem. Solids 28, 2257 (1969).

42. C. T. Foxon, J. A. Harvey and B. A. Joyce, J. Phys. Chem. Solids 34, 1693 (1973).

43. N. Sugiyama, T. Isu, Y. Katayama, Jpn. J. Appl. Phys. 28, L287 (1989).

44. J. D. Benson, B. K. Wagner, A. Torabi, C. J. Summers, Appl. Phys. Lett. 49, 1034 (1986).

45. O. Kubaschewski,and C. B. Alcock, Metallurgical Thermochemistry, ed. 5, Int. Series. Mat. Sci. Tech., Vol. 24, Pergamon Press 1979.

5. PUBLICATIONS

The following presentations and publications were supported by this contract:

Presentations

1. C. J. Summers, A. Rohatgi and K. F. Brennan, The Avalanche Heterostructure and Superlattice Solar Cell, Proc. Polycrystalline Thin FLim Program Meeting, 35-39, July (1987).
2. A. Torabi, C. J. Summers, H. M. Harris and K. F. Brennan, Resonant Tunneling in Variably Spaced AlGaAs/GaAs Multiple Quantum Well Structures, March Meeting of the American Physical Society, March 1988, Bull. Am. Phys. Soc. 33, 701 (1988).
3. C. J. Summers, A. Rohatgi, R. G. Benz II, B. K. Wagner, J. D. Benson and D. Rajavel, "Chemical Beam Epitaxy for II-VI Solar Cell Materials," Proc. of Polycrystalline Thin Film Program Meeting, 99-101, August (1989).

Publications

1. A. Torabi, R. B. Haugen, H. M. Harris, and C. J. Summers, Si Planar Doping of GaAs, J. Vac. Sci. Technol. A7, 1329-1333 (1989).
2. B. K. Wagner, R. G. Benz II and C. J. Summers, A New Fast-Response Hg Vapor Source for HgCdTe Molecular-Beam Epitaxy Growth, J. Vac. Sci. Technol. A7, 295-2999 (1988).
3. C. J. Summers, R. G. Benz II, B. K. Wagner, J. D. Benson and D. Rajavel, New Techniques for the Growth of HgCdTe by Molecular Beam Epitaxy, SPIE, 1106 (1989).
4. J. D. Benson and C. J. Summers, Nucleation Kinetics of Molecular Beam Epitaxially Grown (001) ZnTe and CdTe Surfaces, J. Appl. Phys. 66, 5367 (1989).
5. D. Rajavel, F. Mueller, J. D. Benson, B. K. Wagner, R. G. Benz II and C. J. Summers, In-situ Calibration of Growth Surface Temperature for Molecular Beam Epitaxy of CdTe, J. Vac. Sci. Technol., B8, 192 (1990).

6. R. G. Benz II, B. K. Wagner and C. J. Summers, Growth of CdTe and Hg-based alloys by Chemical Beam Epitaxy, J. Vac. Sci. Technol. A8, 1020 (1990).

6. APPENDICES

The following two appendices contain respectively full details of the processing techniques used to fabricate resonant tunneling diodes and the measurement techniques developed for their characterization.

APPENDIX I

RESONANT TUNNELING DEVICE PROCESSING DETAILS

We give below the full process details used to fabricate the resonant tunneling mesa diode structures following their growth by MBE.

1. Remove Indium
    a. Mount wafer face side down on a glass slide with black wax.
    b. Let cool and scrape excess indium off with razor blade.
    c. Immerse in beaker of HCl @ 40°C until all signs of indium are gone.
    d. Rinse in DI water.
    e. Blow dry.
    f. Remove wafer from glass slide.
    g. Remove black wax with trichloroethylene (TCE).
    h. Blow dry.
2. Lap Backside
    a. Heat lapping pedestal on hot plate.
    b. Apply paraffin.
    c. Mount wafer face down.
    d. Place lens paper on top.
    e. Place assembly in pressure fixture.
    f. Allow to cool.
    g. Remove from fixture.
    h. Remove excess wax with swab and TCE.
    i. Lap with 1000 grit slurry until backside is uniform.
    j. Rinse and blow dry.
    k. Remove excess grit with swab and TCE.
    l. Remove wafer using boiling DI H_2O [Caution - Do not slide wafer on pedestal].
    m. Rinse in methanol.
    n. Rinse in TCE.

- o. Rinse in clean methanol.
- p. Blow dry.

3. Scribe and Break
    - a. Set scribe force to 30 gms
    - b. Scribe at the appropriate position (0.4" typ).
    - c. Break by tapping with blunt end of tweezers.
4. Clean
    - a. Immerse in TCE for 1 min.
    - b. Rinse in methanol for 30 sec.
    - c. Rinse in DI
    - d. Mount on vacuum wand.
    - e. Rinse in microclean solution and gently swab surface.
    - f. Rinse in DI.
    - g. Blow dry.
5. Evaporate Front Contact
    - a. Cut charges.
        - AuGe - 45 mg
        - Ni - 10 mg
        - Au - 60 mg
    - b. Fire boats.
    - c. Clean charges in TCE.
    - d. Clean wafer.
        - NH_4OH: DI (cold)
        - 5 ml: 50 ml
        - 10 sec
    - e. Rinse 15 sec.
    - f. Blow dry.
    - g. Load in system.
    - h. Pump to 8×10^{-7} torr.
    - i. Heat wafer to 100°C (40°C on set point).
    - j. Melt charges

k. Evaporate AuGe (180 Å 1 min typical).

l. Evaporate Ni.

Ramp to 180 Å.
Open shutter.
Ramp to 220 Å for 2 sec.
Close shutter.
Ramp down to 100 Å.
Wait 10 sec.
Repeat 3 times

m. Evaporate Au (180 Å 1 min typical).

n. Remove wafer.

6. Evaporate Back Contact

Same procedure as front contact except omit wafer clean.

7. Alloy

a. Turn on forming gas
b. Allow to purge 4 min.
c. Place wafer on tray.
d. Slide to end of furnace.
e. Ramp to 375°C
f. Pull back to maintain 375°C
g. Pull back to end of furnace.
h. Cool to <150°C.
i. Remove.
j. Turn off gas.

8. Electroplate

a. Compute area to be plated.
b. Compute required current based on a current density of 2 mA/cm^2.
c. Set surrent by connecting cathode lead to anode and adjusting power supply to give the current computed in Step b.
d. Clamp wafer in plating tweezers and mount on ring stand.
e. Connect cathode lead to tweezers.

- f. Lower assembly in solution.
- g. Adjust current to value calculated in b.
- h. Set timer for 12 min.
- i. Disconnect cathode lead when completed.
- j. Remove from ring stand and immerse in breaker of DI water.
- k. Rinse in clean DI.
- l. Blow dry.

9. Mesa Photoresist
    - a. Bake at 120°C for 10 min.
    - b. Spin coat Waycoat resist (3:1) 25 sec at 4000 RPM.
    - c. Bake 10 min. at 80°C.
    - d. Expose 7.5 sec at 12.5 mW/cm^2.
    - e. Develop.
        - 90 sec in Waycoat Negative Resist Developer.
        - 15 sec in N-butyl acetate.
        - 15 sec in methanol.
    - f. Inspect.
    - g. Bake 120°C for 10 min.
10. Mount
    - a. Apply black wax to glass slide heated on hot plate.
    - b. Place wafer face side <u>up</u> on wax.
    - c. Scrub lightly.
    - d. Remove from hot plate and cool.
    - e. Measure resist thickness.
11. Etch Contact
    - a. Etch Au with Au etch (end point determined by color change).
    - b. Etch interface layer in aqua regia (dilute) 1:1 with DI (etch 6 seconds).
    - c. Rinse in DI
    - d. Inspect.
    - e. Measure thickness.

12. Etch GaAs
    a. Connect chlorox bath.
    b. Place wafer-slide assembly under recirculating flow.
    c. Color will initially change to black then back to silver remove immediately.
    d. Rinse in DI.
    e. Blow dry.
    f. Mix 3:1:1 GaAs etch 3 methanol: 1 H_2O_2 : 1 H_3PO_4.
    g. Etch for approximately 40 seconds to achieve total mesa height of 2 μm. (Note this doesn't include resist or contact layer thicknesses).
    h. Rinse in methanol.
    i. Blow dry.
13. Remove Resist
    a. Heat assembly on hot plate.
    b. Remove wafer.
    c. Remove wax with TCE.
    d. Rinse in methanol.
    e. Blow dry.
    f. Immerse in microstrip at 60°C for 3 minutes
    g. Rinse in methanol.
    h. Rinse in DI.
    i. Blow dry.
14. Dice
    a. Mount wafer piece on host wafer with Thermocarbon wax.
    b. Set dicing saw parameters.
    c. Dice wafer piece.
    d. Remove chips from host wafer by heating on hot plate.
    e. Clean chips with TCE.
    f. Rinse in RCE.
    g. Rinse in methanol.
    h. Dry on hot plate.
    i. Transfer to plastic box.

15. Assemble
    a. Select visually good chips.
    b. Mount in package with silver epoxy.
    c. Cure 5 min at 150°C.
    d. Wire bond using thermocompression bonder and 0.0007 mil Au wire.
16. Test
    a. Set curve tracer for

       500 mV

       10 mA.
    b. Connect leads to appropriate package pins.
    c. Immerse in liquid nitrogen.
    d. Increase collector voltage.
    e. Observe device I-V characteristics.

APPENDIX II
MEASUREMENT TECHNIQUES FOR RESONANT TUNNELING DIODE STRUCTURES

Introduction

Accurate measurements of I-V characteristics of VSSEF and DBSQW devices is complicated by several factors, as noted below. We describe here the activity that was generated by this program to resolve this problem and which enabled us to more fully understand the curve tracer data.

Measurement Problem

For negative differential conductance devices such as tunnel or Gunn diodes, both of which exhibit short circuit stable behavior, the simple measuring circuit shown in Figure 1 is normally used. For this circuit, it is presupposed that a large G_{ST} will lead to unconditional stability and allow one to plot the dc device current as a function of dc ramp voltage. Indeed, for a tunnel diode, this is correct as indicated by Figure 2(a).

Failure to provide stabilization by way of large G_{ST} can lead to random results such as 2(b) where L and G_S are allowed to be random values based on test leads, etc. Case 2(b) is simply a plot of the average value of I while the device is oscillating sinusoidally. Case 2(c) is simply another case where a stabilizing conductance G_{ST} having excessive self-inductance has been employed. Obviously then, a voltage stable device exhibiting negative differential conductance must be stabilized using a known low inductance G_{ST} in order to plot stable an I-V curve.

It is not the objective to obtain I-V characteristics of the combination of G_{ST} and the device; therefore, bridget networks must be employed to balance out the current drawn by G_{ST}. Lacking the bridge network, the device geometry in Figure 3 can sometimes be employed. When acceptable, the configuration of Figure 3 is preferred. Unfortunately, it is frequently the case that the algebraic sum of the current sensing conductance G_{SE} and the shunt conductance G_{ST} is far more difficult to keep sufficiently large and/or inductance free than is the simple parallel conductance of Figure 1(a).

$$(G_{ST}G_{SE})/(G_{ST} + G_{SE})$$

Therefore, we developed the simple geometry of Figure 1(a) for most of our testing. It should also be noted that by way of duality, all of the above arguments are valid for an open circuit stable device where V is a single valued function of I as opposed to the short circuit stable device where I is single valued with V. Therefore, the approach considers that the device may be either short or open circuit stable. It is interesting to consider that the new devices may be neither, in which case, the device would be intrinsically bistable and incapable of providing stable sinusoidal oscillations. In this case, the transient bahavior of the device requires study.

Comment on Bi-Stability

We will not consider the question of bistability extensively herein. It is, however, interesting to refer to Figure 4 and note the following: The device of Figure 4 exhibits discontinuous behavior of I with respect to V and can have no other I-V characteristic in the absence of oscillations; therefore, it is interesting to note some of the arguments recently published.[1,2] The device shown in Figure 4 (as previously noted) cannot sustain stable sinusoidal oscillations and give the I-V characteristics shown for the circuits of both 4(a) and 4(b).

It is, apparently, not well recognized that the behavior of such a bistable device can be altered extrinsically to provide the behavior of Figure 5(a) where, in a sense, one has presupposed open circuit stability and attempted to stabilize the I-V response using a low series conductance as indicated by 5(b). Although still bistable, the device now exhibits double valued voltage behavior with respect to the curent I. In fact, the responses of Figure 4 and 5 prove unquestionably that such a device is intrinsically bistable.

Measurement Approach, Apparatus

Given the need to test the circuits of 6(a) and 6(b), and to do so at cryogenic temperatures unique means are required for testing. Consider the following:

1) Numerous devices must be tested.

2) I_{ST} is often times about one hundred times as great as I_D (G_{ST} is large in order to achieve stability). Therefore, for accurate plotting, I_D must be resolved to about one part in ten thousand in order to obtain smooth and detailed data.

3) G_{ST} and G_{SER} must have low self inductance and the interconnections among G_{ST},G_{SER} and the device must be kept low in inductance. Therefore, G_{ST} and/or G_{SER} must be mounted adjacent to the device and operated at cryogenic temperatures along with the device. A typical geometry is shown in Figure 7.

4) The need to resolve very small I_D compared to I_{ST} requires either very accurate knowledge of G_{ST} (cryogenic) or balancing of the bridge measurement apparatus for G_{ST} prior to connection of the active device, a laborious approach of questionable accuracy because of handling and possible disturbance to a very exacting bridge balance. All four of these problems have been solved in the approach described below.

Apparatus

The simplified test circuit of Figure 8 is employed for all two terminal device testing.

Obviously, adjustment of R_1 and R_2 can eliminate (balance out) the voltage present at a-b due to current flowing in G_{ST}, leaving the remaining voltage at a a-b to represent the device current. The question, then, is how can this be conveniently achieved with precision. The following steps are used.

1) The device alone is tested first. This may lead to any of the measured responses of Figure 9(a), (b) or (c) due to random loading by the driver.

The sole purpose of this initial test is to obtain an accurate measurement of the unconditionally stable regions a-b and c-d of the device response. This response is unchanged for all conditions of loading including any value of G_{ST} and/or G_{SER} later employed. To obtain the response, R_2 is set to zero such that the voltage at a,b of Figure 8 is due only to the device current through the 1 ohm resistor R(I_{SENSE}). Both voltage and current are thus unambiguously measured.

2) Next, the stablizer is connected and R_2 (Figure 8) is readjusted to obtain the response previously noted (Figure 9, regions a-b, c-d). This is not immediately

possible without noting the following. It is readily demonstratable that the voltage V_{ab} represents the device current where:

$$I_{DEVICE} = [G_{SEN} + G_{ST}]V_{A\text{-}B} \tag{1}$$

For instance, when G_{SEN} and G_{ST} are both 1 mho, $I_{DEV} = 2\ V_{a\text{-}b}$. The exact value is not of concern. Therein lies the simplicity of our approach. Simply stated, the bridge resistance R_2 and the gain of the difference amplifier, (Y) [Figure 8], can be carefully adjusted to achieve the unchanging response in regions a-b and c-d of Figure 9. The mid-region of the response, under prevailing conditions, will then be precisely indicated by $V_{a\text{-}b}$ (Figure 8) as amplified by the difference amplifier (Y).

Measurement

The approach and circuit described have been used to evaluate a number of device types. Included are:

- o Devices exhibiting intrinsic bistability,
- o Devices exhibiting responses having stable NDR at lower voltages and a region of bistability (not due to sinusoidal oscillations) at higher voltages, and
- o Devices exhibiting only a region of stable NDR.

Conclusions

Accurate measurements of I-V for VSSEF and DBSQW devices can be routinely performed at low temperatures with a device current resolution of about .01%. This capability will contribute greatly to the comparison and optimization of device structures.

References

1. V. J. Goldman, et al., "Observations of Intrinsic Bistability in Resonant Tunneling Structures," Physical Review Letters, 58, 1256-1259 (1987).

2. T.C.L.G. Solner, Comment on "Observation of Intrinsic Bistability in Resonant Tunneling Structures," Physical Review Letters, 59, 1622 (1987) and response by Goldman, et al., Phys. Rev. Letters, 59, 1623 (1987).

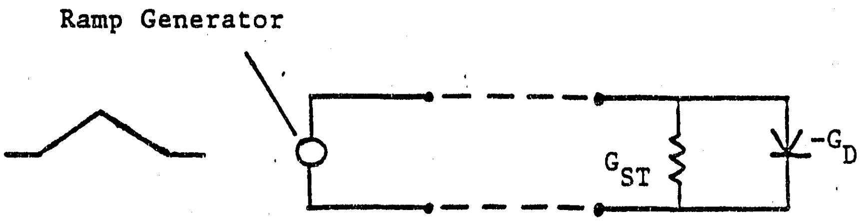

Figure 1. Circuit for Initial Test, Short Circuit Stable Device.

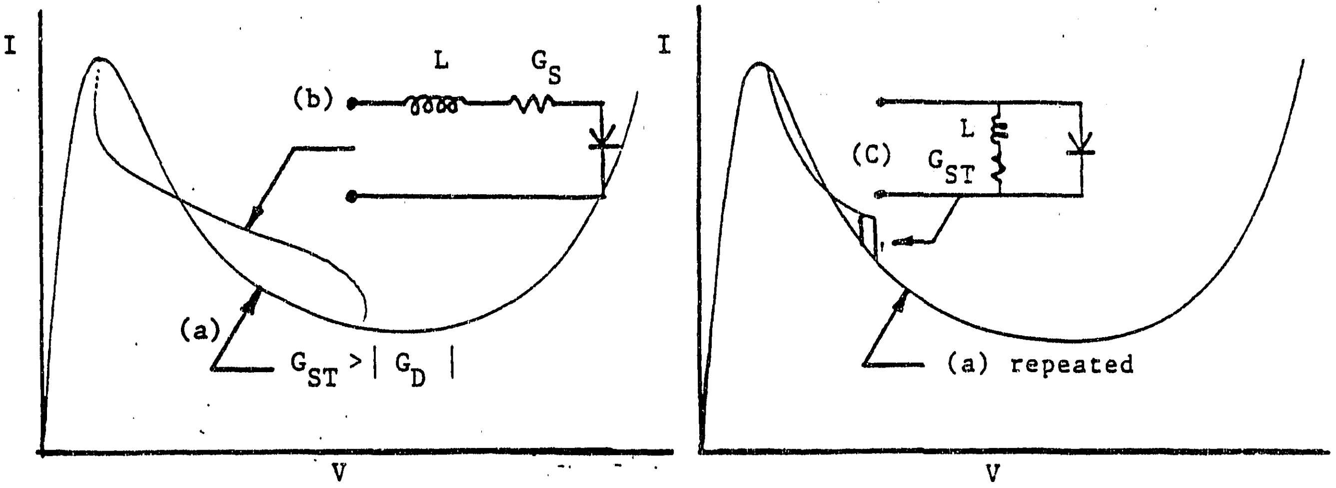

Figure 2. Stable and Oscillating I/V Curves for a Tunnel Diode.

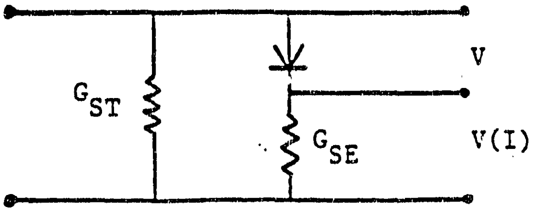

Figure 3. Unambiguous Test Geometry Using Two Conductances.

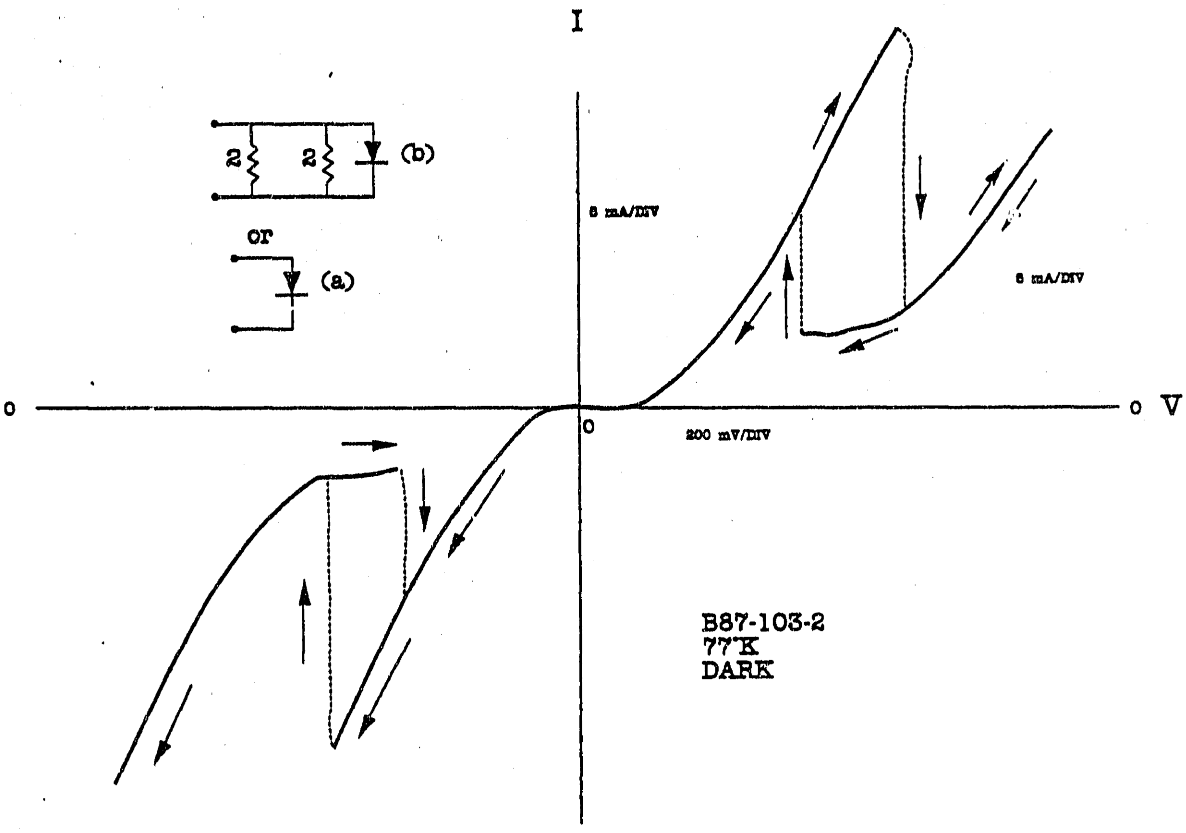

Figure 4. Bi-stable Current Behavior

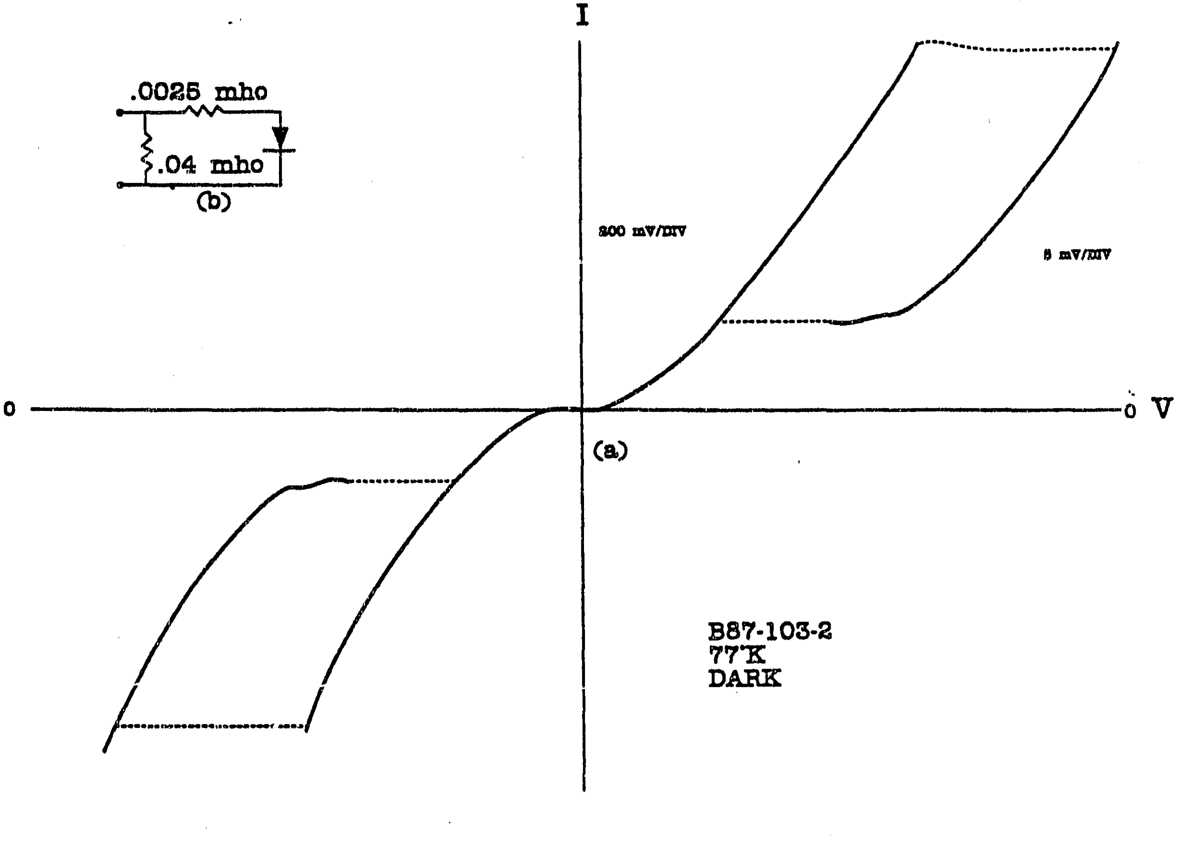

Figure 5. Bi-stable Voltage Behavior

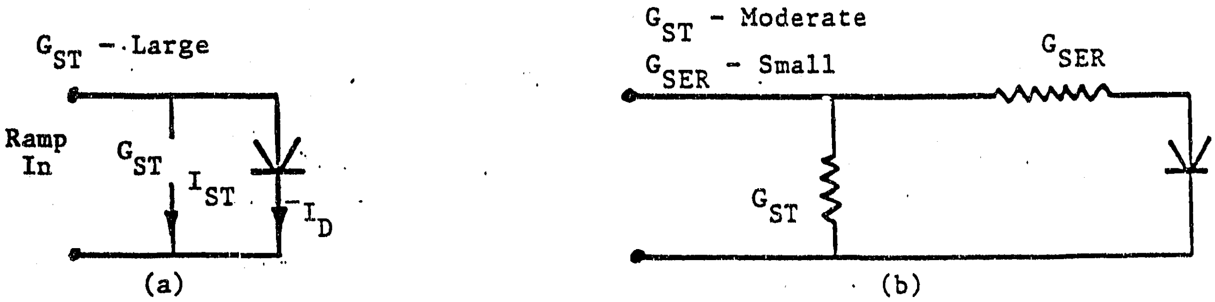

Figure 6. Short Circuit (a) and Open Circuit Test Geometries

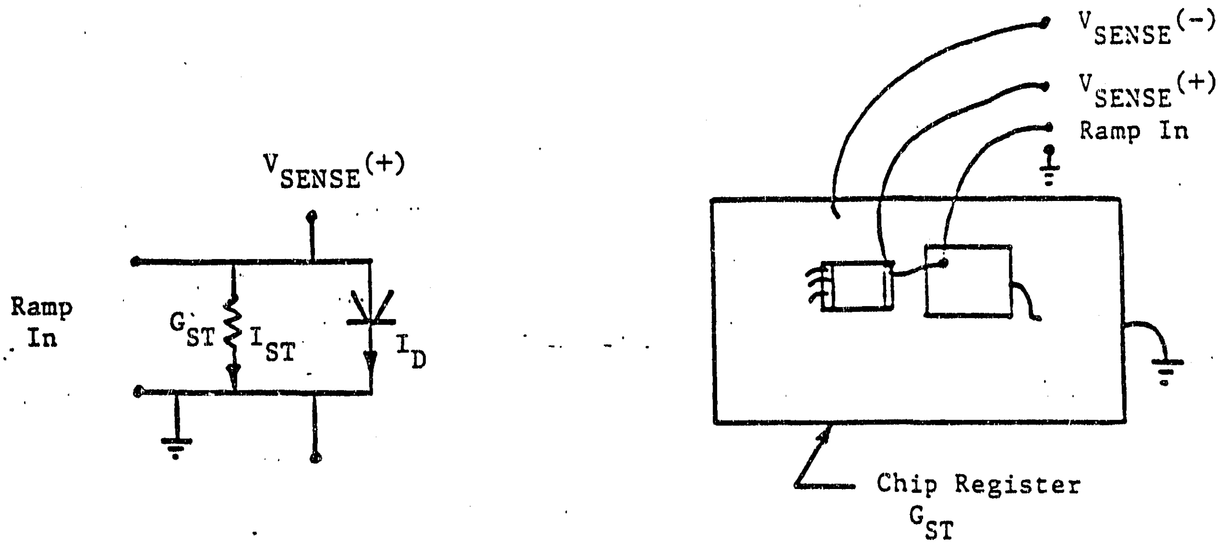

Figure 7. Typical Test Arrangement for Short Circuit Stable Geometry

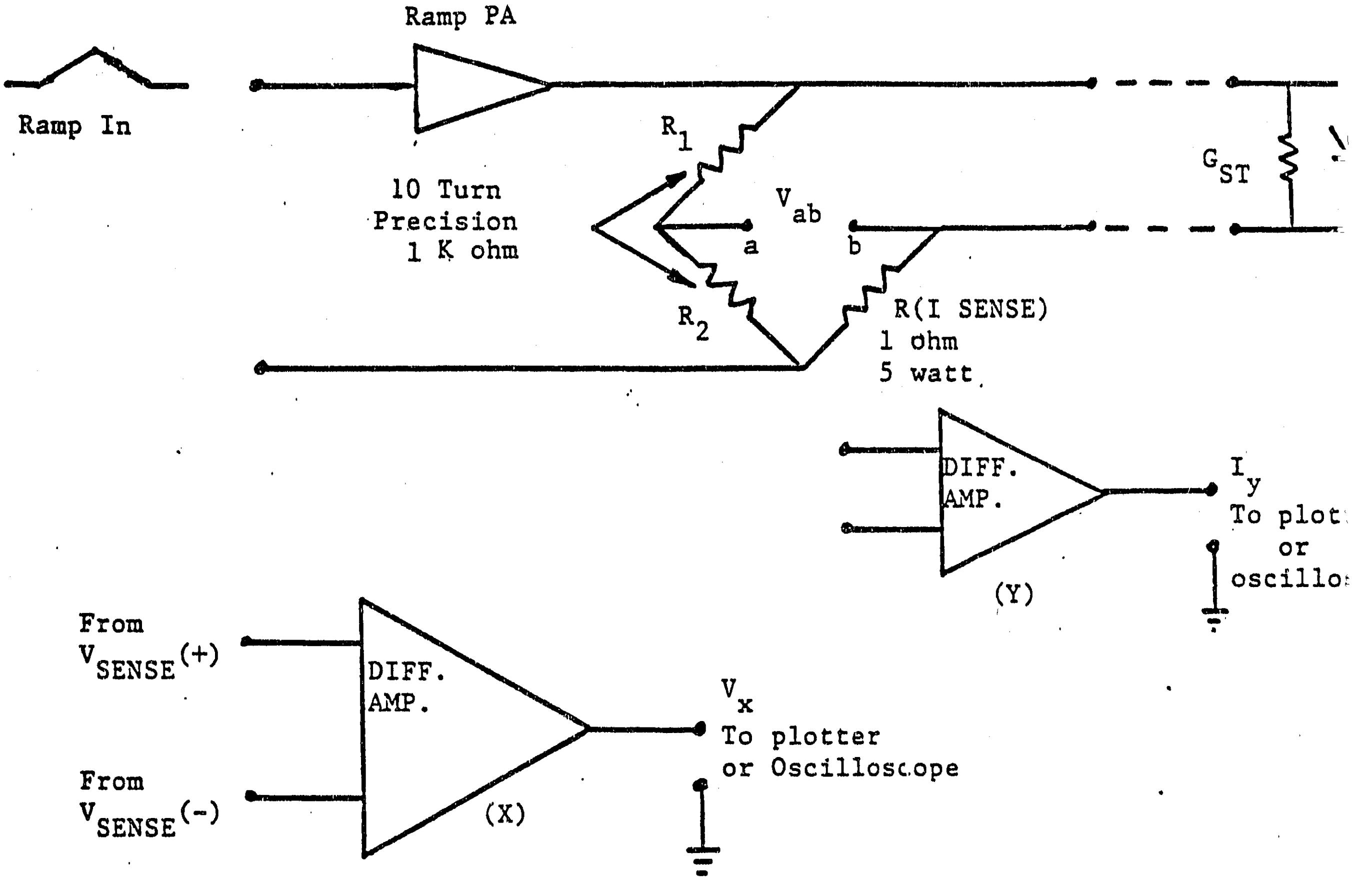

Figure 8. Simplified Test Circuit

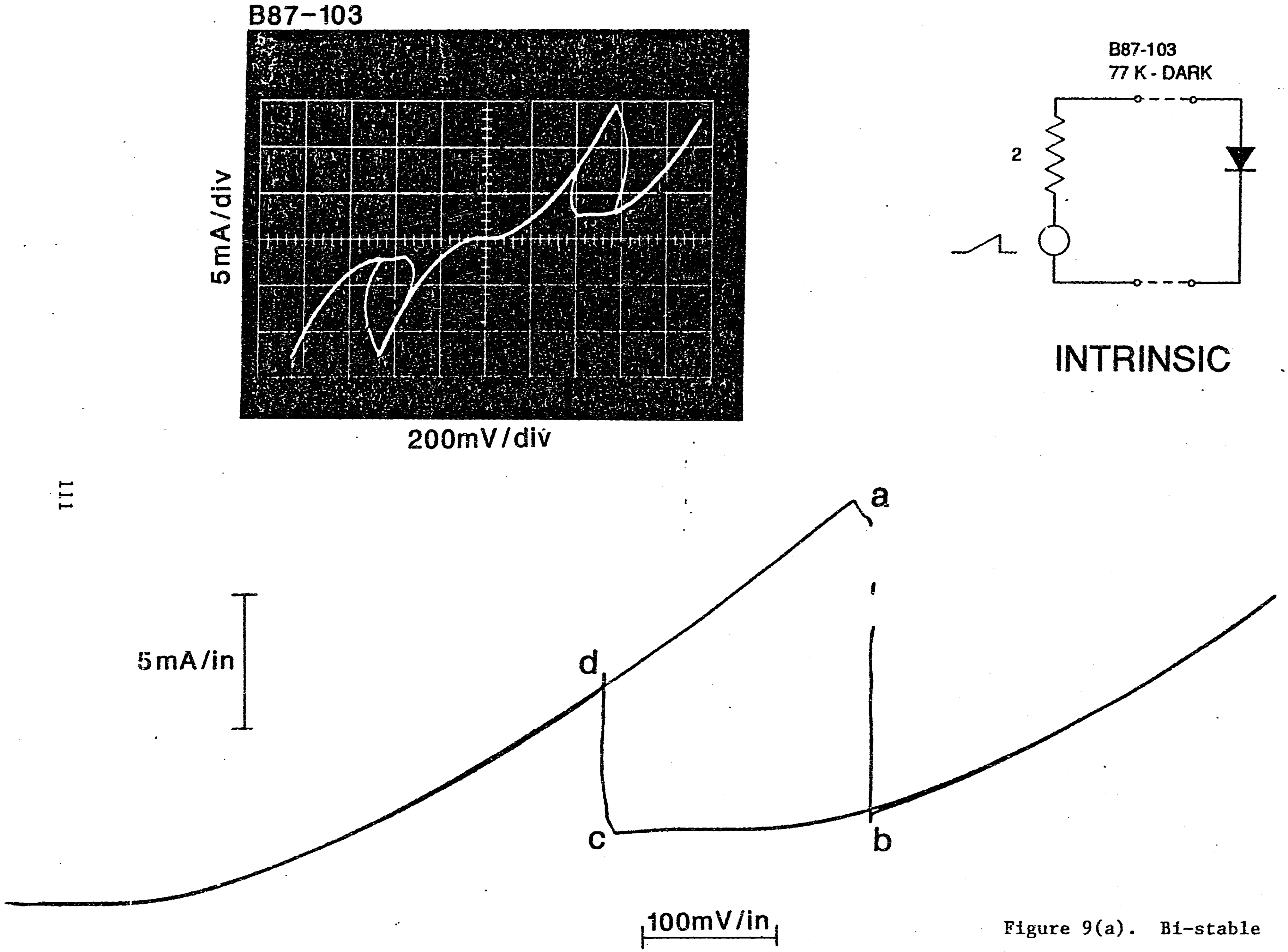

Figure 9(a). Bi-stable

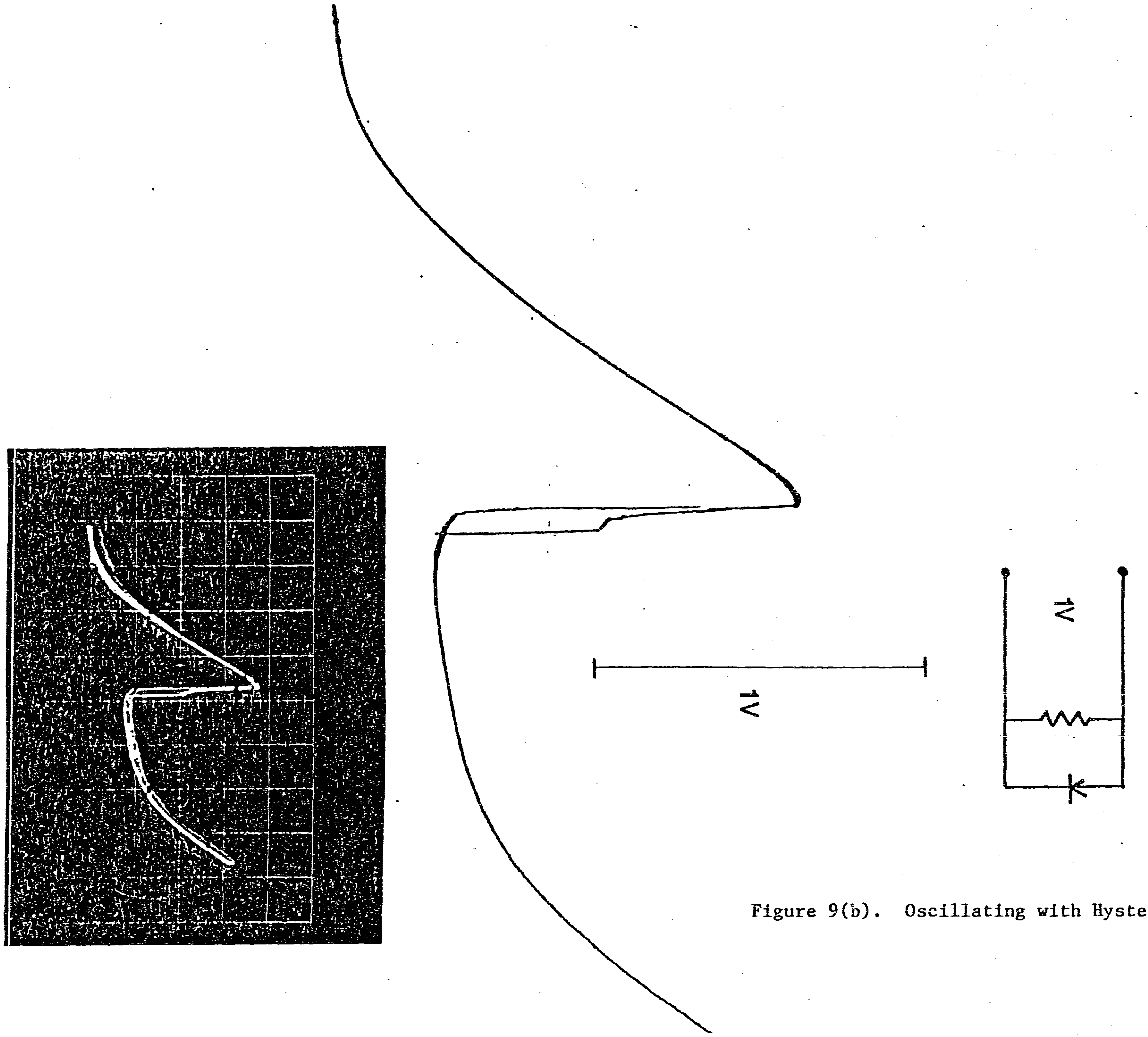

Figure 9(b). Oscillating with Hysteresis.

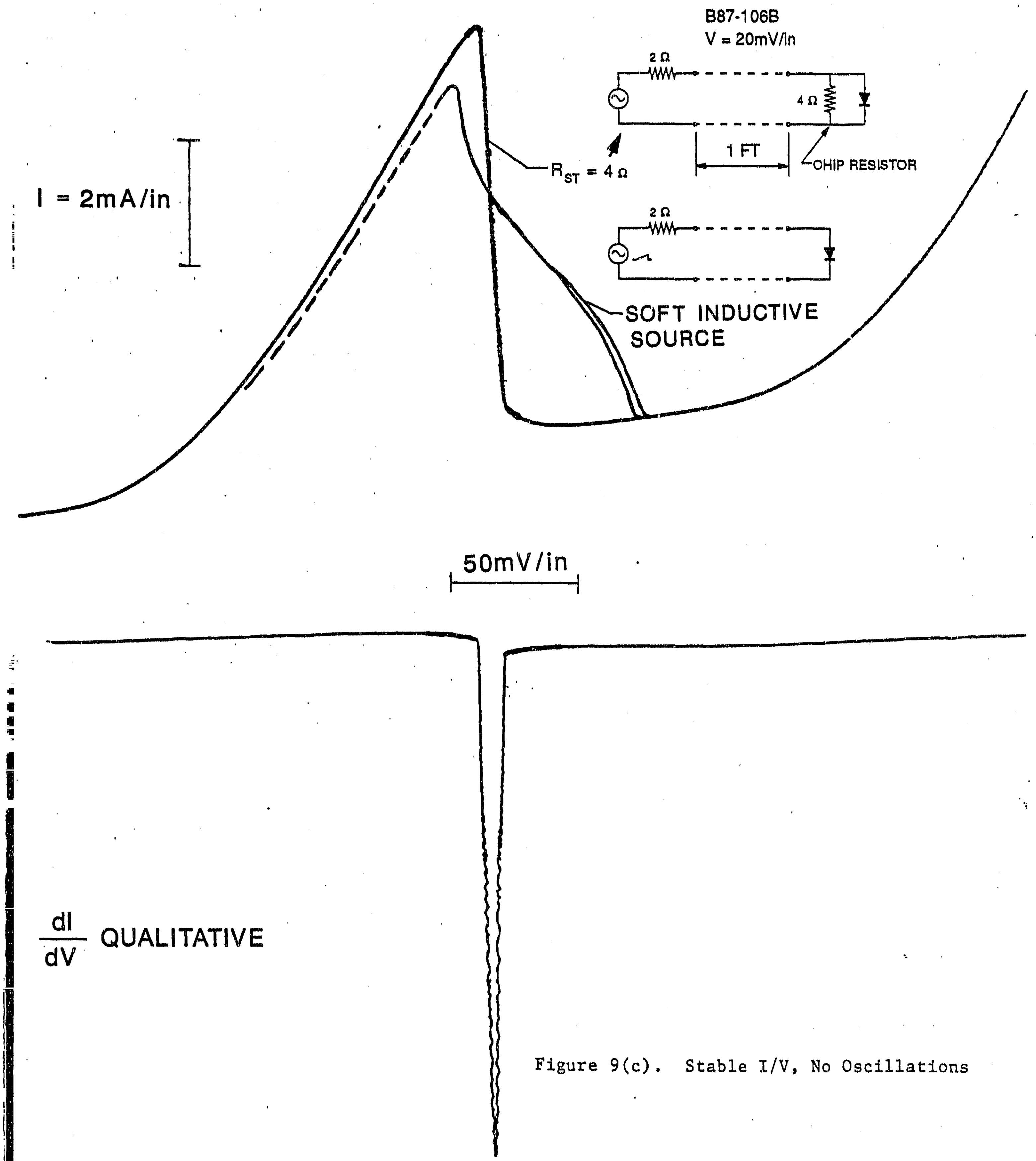

Figure 9(c). Stable I/V, No Oscillations

END

DATE FILMED

4/8/93